Fakultät für Physik und Astronomie

Ruprecht-Karls-Universität Heidelberg

Masterarbeit

Im Studiengang Physik

vorgelegt von

Carl Heintze

geboren in Hamburg

2020

Projektion von repulsiven Potentialen in ultrakalte Quantengase mit einem Mikrospiegelaktor

Die Masterarbeit wurde von Carl Heintze

ausgeführt am

Physikalischen Institut

unter der Betreuung von

Prof. Dr. Selim Jochim

Department of Physics and Astronomy

University of Heidelberg

Master thesis

in Physics

submitted by

Carl Heintze

born in Hamburg

2020

Projection of repulsive potentials in ultracold quantum gases with a Digital Micromirror Device

This Master thesis has been carried out by Carl Heintze

at the

Physical Institute

under the supervision of

Prof. Dr. Selim Jochim

Projektion von repulsiven Potentialen in ultrakalte Quantengase mit einem Mikrospiegelaktor :

In dieser Arbeit wurde der Einbau und Betrieb eines Mikrospiegel-Aktors (DMD) zum Projizieren repulsiver optischer Potentiale in ein ultrakaltes Quantengas geplant. Das Ziel ist die Erzeugung von homogenen Systemen und arbiträren Potentialen. Die Nutzung eines DMDs ist durch zwei verschiedene Ansätze motiviert. Einerseits erfordert die Messung von globalen Transportparametern, welche Einblick in Paar-Paar-Korrelationen und universelle Skalen geben, homogene Systeme [1]. Andererseits ermöglichen flexibel skalierbare Potentiale die Untersuchung des Übergangs von kleinen Box-Systemen zu makroskopischen statistischen Ensembles [2].

In einem ersten Test-Aufbau wurde die DMD-Mikrospiegel mit einem Teleskop auf eine Kamera abgebildet, um binäre und skalierbare DMD-Masken zu untersuchen. Es wird eine Methode beschrieben, welche die mathematische Abbildung zwischen der DMD- und der Kamera-Ebene findet, um Abbilungsfehler zu korrigieren. Verbleibende Störungen des Potentials werden quantifiziert und mit den Skalen in der optischen Falle verglichen. Um die Leistung unseres Abbildungssystems zu überprüfen, wird das Gaussche Strahlprofil der Lichtquelle mithilfe des DMDs ausgeglichen und ein ebenes Intensitätsprofil in die Bildebene projiziert. Im Test-Aufbau wird eine relative mittlere quadratische Abweichung von 3.8 % erreicht, was ausreichend ist, um mit der Projektion in die Atomebene fortzufahren.

Projection of repulsive potentials in ultracold quantum gases with a Digital Micromirror Device:

In this thesis the implementation and application of a digital micromirror device (DMD) in the context of a cold atom experiment to perform beamshaping was planned. The target are homogeneous systems and arbitrarily shaped potentials. The usage of a DMD is motivated by two different aspects. First the measurement of bulk properties, giving insight into pair-pair correlations requires a homogeneous system [1]. Secondly, arbitrary shaped potentials can be used to study the transitions from small box systems towards large statistical ensembles [2].

In a test setup, imaging the DMD pattern via a single telescope onto a camera, binary and grayscaled potentials were examined. In the following a procedure is described to map the DMD-screen on the image plane and to account for imaging imperfections by finding the corresponding image transformation functions. Remaining potential disturbances on the camera screen are quantified and compared with trap scales. To quantify the performance of the system in terms of grayscaling, one accounts for the Gaussian beamshape of the lightsource and project a flat potential into the first image plane. With the test-setup, a relative root-mean-square deviation of 3.8 % was achieved, which allows to take a step further and start beamshaping into the atom plane.

Contents

1

Introduction

Superconductivity and superfluidity are fascinating phenomena, which are still part of actual research. For weakly interacting fermionic systems superfluidity was explained by Bardeen, Cooper and Schrieffer. They connected the phenomena with the emergence of strongly correlated pairs of opposite momentum [3]. However, superfluidity in strongly interacting fermionic systems is still not fully understood.

Ultracold atoms offer a very clean and flexible way to experimentally examine fermionic superfluidity in these strongly interacting systems. Most of the relevant parameters such as interaction strength, temperature, interparticle distance and the confining potential [4] can be precisely controlled.

In our group, we experimentally study the BEC-BCS crossover in 2D fermionic ^{6}Li systems [5] with cold atom samples of fermionic ^{6}Li in an optical trap. The essential parameters for the pairing process are the size of the pairs with respect to the interparticle spacing or accordingly the scattering length with respect to the interparticle spacing [4]. They can be controlled by tuning the interaction strength via the magnetic field. In this way, the quantum gas can be studied from the limit of spatially tightly bound pairs to pairs, being spread over several instances of the inter-particle spacing [6]. Of special interest is the strongly interacting regime, lying between these two limits. In this regime the system shows universal behavior and can serve as a benchmark for theories [7, 8]

Strongly interacting 2D-regimes were already explored in this group [9], revealing violations of classical scaling symmetries. Further insight in the behavior of quantum gases at criticality can be gained by the measurement of thermodynamic properties. Local properties, like compressibility or density have already been studied and the superfluid phase transition was observed [8].

Since most quantum gas experiments use magnetic traps or Gaussian optical beams to trap the atoms, they experience curved potentials and the chemical varies over the trap. Therefore, making predictions by studying global thermodynamic properties is highly complicated, due to the local variations within the trapped sample. From a theory point of view however, it would be highly desirable to be able to measure global transport properties as they offer insight in pairing processes and universal quantities in these systems [10]. Especially the bulk viscosity can be directly connected to pair-pair correlations, which are essential for the superfluid phase transition [1]. In this way, universal relations, such as the equation of state or universal critical temperatures, can be extracted from the measurements in a straightforward way, if the system is homogeneous. This is our motivation to create a homogeneous trap by including a beamshaping device in the setup, which, in the future, will allow us to create arbitrary potential for the atoms.

We plan to achieve controlled beamshaping by introducing a digital micro mirror device (DMD). First, we want to use repulsive optical potentials to project a two dimensional box into the atom plane. This gives us the platform to study homogeneous systems. Later, we will use the DMD to create arbitrary shaped potentials.

One perspective would be to project two reservoirs of variable size in the atom plane and to couple them dynamically. Questions about the evolution from small coherent ensembles to large, statistically described ensembles and the influence of reservoir sizes on transport properties can be evaluated [2].

In the following, the design consideration of a DMD-setup for the existing experiment will be reported. In a test setup the projection of binary and grayscaled potentials was examined. Therefore, the current experimental setup is briefly discussed (sec. 2.1), followed by the physical fundamentals. Subsequently the DMD setup is discussed, starting with an introduction about the technical details (sec. 3.1) of the device. Then, I present the physical constraints and the concrete design (sec. 3.2). Afterwards, the usage and the creation of binary as well as grayscaled potentials in the test-setup is discussed (sec. 3.3). Finally, I give a conclusion and present our future plans with the setup (sec. 4).

2

Physical fundamentals

2.1 The experiment

Tackling questions about many particle physics arising from few particle interactions with cold atoms requires quantum control on the single particle level and a solid understanding about particle interactions and other relevant scales in the system.

The experiment uses ^{6}Li atoms which are fermions. Since the physics are determined by the inter-particle interactions, precise adjustments of the interactions strength offers a lot of control about the quantum system.

2.1.1 Interactions

Fermions are characterized by their exchange symmetry. The fermionic creation and annihilation operators fulfill the anti-commutator relations $\{a_\mathrm{i}^\dagger, a_\mathrm{j}^\dagger\} = \{a_\mathrm{i}, a_\mathrm{j}\} = 0$ for the modes i and j. Therefore, exchanging two particles changes the overall sign of the wavefunction, which leads to the Pauli-exclusion principle, stating that two identical fermions cannot occupy the same state. Therefore, in the fermionic groundstate, the particles fill all the lowest energy shells of the system with one particle per state. The fermion in the highest occupied state at zero temperature gives the energy-scale of the system. The Fermi energy in two dimension is given as

$$E_\mathrm{F} = \frac{n\pi\hbar^2}{m}, \tag{2.1}$$

depending on the particle mass m and the particle density n.

There are three main length scales in the system. Firstly, the inter-atomic distance $n^{-1/3}$ with n being the density of the sample. Secondly, the effective range of inter-atomic potentials r_0 which are dominated by van-der-Waals interactions scaling with $1/r^6$ and thirdly the thermal de-Broglie wavelength of the atoms which is

$$\lambda_T = \hbar\sqrt{\frac{2\pi}{mk_BT}}. \tag{2.2}$$

T is the temperature, m the mass and k_B is the Boltzmann-constant. Realistic numbers for cold atom experiments can be found in [11] and are for example

$$\begin{aligned} n^{-1/3} &= 1\,\mu\mathrm{m} \\ T &= 50\,\mathrm{nK} \\ \lambda_T &= 3\,\mu\mathrm{m} \\ r_0(\mathrm{Lithium}) &= 182\,\mathrm{pm}. \end{aligned} \tag{2.3}$$

The de-Broglie wavelength is on the order of the inter-atomic spacing and much larger than the effective range of the van-der-Waals potential, i.e. it is reasonable to assume that the precise shape of the potentials is not resolved by scattering processes and that it can be approximated by a spherical symmetric potential. The inter-atomic spacing is also much larger than the effective range of the interactions and therefore higher order collisions beyond two body are negligible.

To describe the interactions one uses the Schrödinger-equation for the reduced one-particle problem (c.f. [4])

$$\left(\nabla^2 + k^2\right)\Psi_{\vec{k}}(r) = v(r)\Psi_{\vec{k}}(r) \tag{2.4}$$

with $k^2 = \frac{mE}{\hbar^2}$ and $v(r) = \frac{mV(r)}{\hbar^2}$ and m being the particle mass. One finds that

$$\Psi_{\vec{k}} \propto e^{i\vec{k}\vec{r}} + f(\vec{k}',\vec{k})\frac{e^{ikr}}{r} \tag{2.5}$$

with f being the scattering amplitude for the momenta $\vec{k}$ and $\vec{k}'$ and containing all the interesting physics beyond the plane wave part in the first term. As already mentioned, spherical symmetry can be assumed and the wave functions are expanded in spherical waves of different angular momenta l. One finds that the scattering process leads mainly to a phase shift δ_l of the atomic wavefunction and that the phase shift depends on l and k such that

$$\delta_l \propto k^{2l+1}. \tag{2.6}$$

For low temperature and small $k << 1/r_0$ just the s-wave terms ($l = 0$) are important and the scattering physics are mainly described by the s-wave scattering length a. For the scattering length, defined as $a = -\lim_{k<<1/r_0} \frac{\tan(\delta_0)}{k}$, the scattering amplitude in low order reads

$$f(k) = \frac{1}{-1/a + r_{\text{eff}}k^2 - ik}. \tag{2.7}$$

r_{eff} is the effective range of the inter-atomic potential and given by r_0 for van-der-Waals interactions.

2.1.2 Feshbach resonances

Having a model for the inter-atomic interaction in the quantum gas, it is of main interest to find a way to manipulate it. Precise control over the interaction strength enables the experimentalist to create completely different regimes, ranging from tightly bound molecules to large, weakly bound atomic pairs being correlated over the whole trap. Therefore one exploits the different magnetic moment of the two-particle atomic states. Their energy depends on the inter-atomic distance and, since the state has a certain magnetic moment, on the magnetic field. If two atoms scatter, their initial two-particle state scatters into another two-particle state with the same energy (see fig. 2.1). Most important for the experimental routine is the case, with

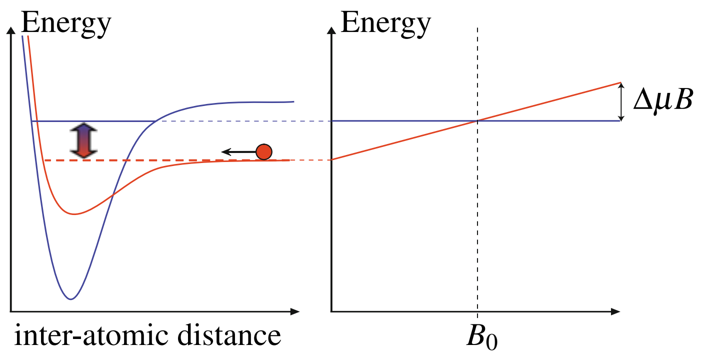

Figure 2.1 Figure taken from [12]. Energy curves of two particle scattering. On the left side the open and the closed channel are shown and on the right side the detuning of the channels in dependence of the magnetic field is plotted. $\Delta\mu$ signifies the difference in magnetic moments and B the magnetic field. B_0 marks the Feshbach-resonance i.e. where the detuning is zero.

an incoming unbound state, called the open channel and another channel of higher energy, called the closed channel, consisting a bound state. An initial state in the open channel cannot scatter in a final state in the closed channel due to energy conservation but virtual processes are possible. The atoms can scatter in the closed channel and return after a **short** amount of time. This process leads to a phase shift of the wave function. The duration of the process and therefore the phase shift depend on the detuning between closed and open channel. Since the two channels have different magnetic momenta, the detuning is adjustable via the magnetic field. As a result the s-wave scattering length or the interaction strength can be controlled via the magnetic field. Fig. 2.2 shows the s-wave scattering length in units of a_0, the background scattering length, being present without any magnetic field. The indices correspond to different combinations of states in the hyperfine manifold of the electronic groundstate of ^{6}Li.

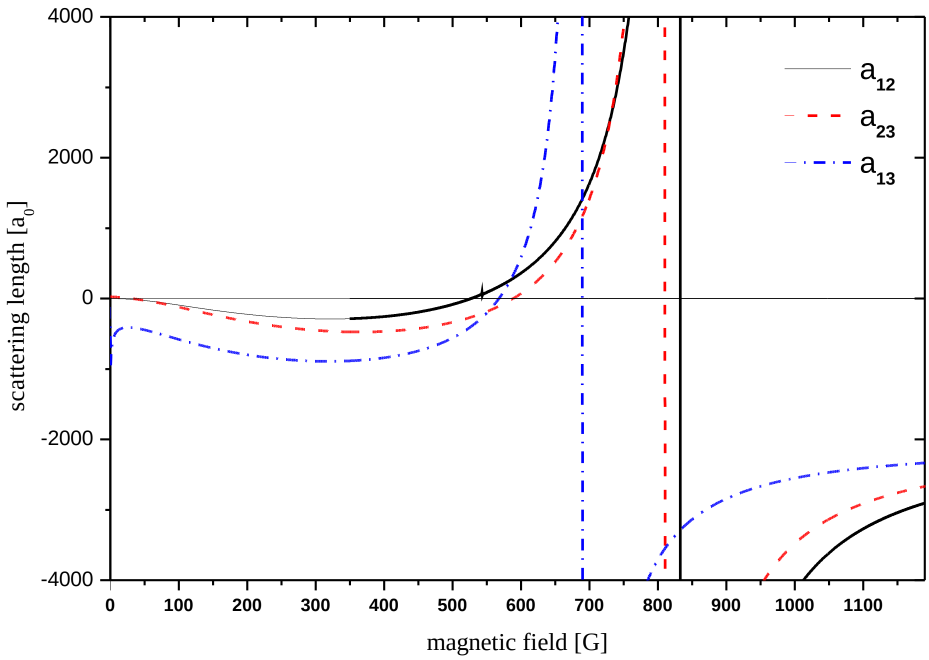

Figure 2.2 s-wave scattering lengths for the three lowest states in the hyperfine manifold of the electronic gorundstate of ^{6}Li in units of the Bohr radius a_0 of the states $|1\rangle$ and $|3\rangle$ (c.f. fig. 2.6).

2.1.3 Experimental realization

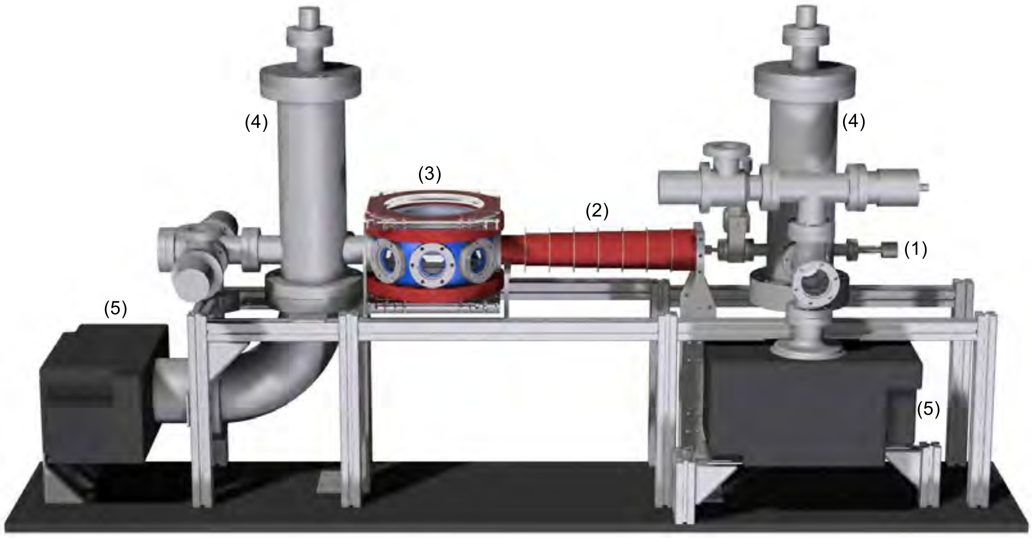

Figure 2.3 The vacuum architecture. The atoms are evaporated at $350\,^{\circ}C$ (1), subsequently the Zeeman slower slows the atoms (2) and they enter the main experimental chamber (3). Optical access (NA of 0.8) for absorption and fluorescence imaging is given from above and from below. The apparatus is pumped by two titanium sublimation pumps (4) and ion pumps (5). Taken from [13].

The vacuum apparatus is shown in fig. 2.3. The atoms are evaporated in an oven at $350\,^{\circ}C$ and enter through an aperture the Zeeman slower. The Zeeman slower is used to slow down the atom beam which finally reach the experimental chamber. There, the atoms are trapped in a magneto optical trap (MOT).

MOT and optical dipole trap A MOT consists of three pairs of circular polarized, red detuned beams (one for each dimension). Trapping is achieved by the interplay of the MOT beams and a pair of coils in anti-Helmholtz configuration producing a magnetic field gradient. The MOT geometry along one dimension is shown in fig. 2.4. The beams are red detunded by δ and a magnetic field gradient is present along the horizontal axis. The magnetic field leads to a space dependent Zeeman shift of the magnetic sublevels such that the atoms at a distance x_0 from the center are in resonance with a beam pointing towards the trapcenter. Therefore the atoms get confined. Additionally atoms moving fast in the horizontal plane get cooled because they come into resonance with a counter propagating beam due to the Dopplershift.

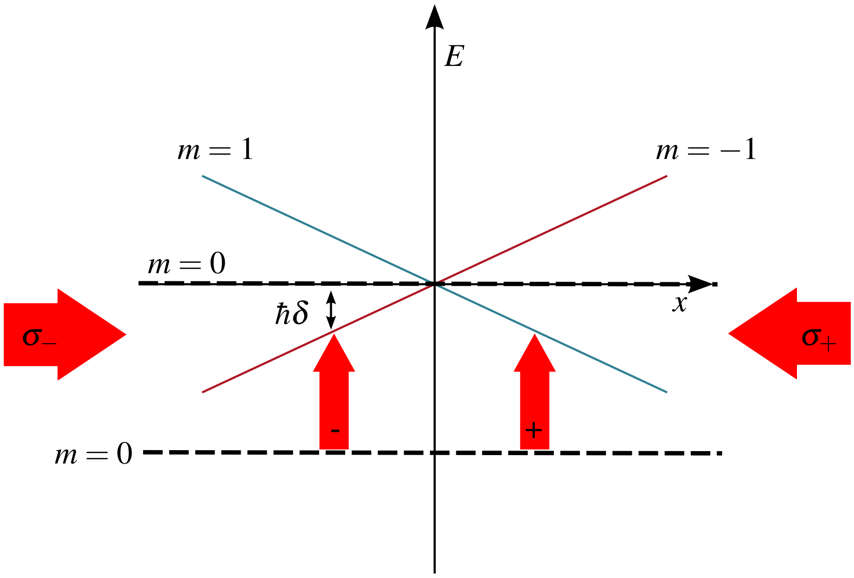

Figure 2.4 MOT. By δ red detuned light shines onto the atoms. A magnetic field gradient leads to a space-dependent Zeeman shift of the magnetic sub-levels. Due to the different polarizations of the laserbeams, the atoms at a certain radial distance are in resonance with a beam pointing towards the trap center and experience a confining force.

This way one achieves atom numbers on the order of $\approx 10^7$ particles in the MOT. The size of the MOT is decreased by increasing the strength of the magnetic field gradient at the same time as decreasing the laser detunings. This way, the atoms are transferred into the optical dipole trap (ODT) which is built by two crossing beams with orthogonal polarizations of an industry laser at 1064 nm which can emit maximally 200 W. The orthogonal polarizations ensure that the two beams do not interfere and built a manifold of ellipsoids.

Optical dipole traps exploit the polarizability of atoms. In a semi-classical picture, one can describe the atom as a two level system coupling to the classical light field. From the polarizability leading to a force in intensity gradient fields one can deduce the optical dipole potential (c.f. [14]) as

$$V = \frac{3\pi c^2}{2\omega_0^3}\left(\frac{\Gamma}{\Delta} + \frac{\Gamma}{\omega_0 + \omega}\right) I. \tag{2.8}$$

c is the speed of light, ω_0 the angular frequency of the atomic resonance, ω the laser frequency, Γ is the natural linewidth, Δ is the detuning of the light field with respect to the atomic resonance and I is the intensity of the light field[1]. The resonance frequency in our experiment is the transition frequency from the $2^2\mathrm{S}_{1/2}$ state to $2^2\mathrm{P}_{3/2}$ state which is the Lithium D2 line at 671 nm.[2]. For effective trapping one has to evaluate the amount of photon scattering, heating the atom sample. The photon scattering rate Γ_{sc} is given as

$$\Gamma_{\mathrm{sc}} = \frac{3\pi c^2}{2\hbar\omega_0^3}\left(\frac{\omega}{\omega_0}\right)^3\left(\frac{\Gamma}{\Delta}+\frac{\Gamma}{\omega_0+\omega}\right)^2 I. \tag{2.9}$$

In both equations the counter propagating term $\propto \frac{\Gamma}{\omega_0+\omega}$ can be neglected, since the detuning is small. By comparing the two equations, one finds that the photon scattering is proportional to $\left(\frac{\Gamma}{\Delta}\right)^2$, while the potential is linear in $\frac{\Gamma}{\Delta}$. Therefore, for increasing the detuning, the photon scattering rate shrinks faster than the optical potential and trapping gets more effective in terms of heating due to photon scattering. By using the linear dependence of the potential on $I(\vec{r})$, the potential landscape in ODTs can be formed by modulating the intensity profile of the laser. In our case this is Gaussian, but with different widths along x and y resulting in a "surfboard" shaped trap. Note that red detuned light builds attractive and blue detuned light repulsive potentials.

To enter the 2D regime the atoms have to be transferred to a "pancake" trap, the "Schielbrille". Two beams of a INNOLIGHT Mephisto-S 500 NE laser providing up to 500 mW. The Mephisto seeds a fibre amplifier which amplifies it up to 50 W. The beams are superimposed under an angle of 14° (c.f. 2.5a) with parallel polarizations leading to interference. The pattern builds up as an ensemble of "pancakes" providing the 2D regime. In this setup aspect ratios of $\omega_z/\omega_r \approx 300:1$ are achieved. The axial trap frequencies reach up to $\omega_z \approx 2\pi \times 7\,\mathrm{kHz}$ (c.f. [13]). For few fermion experiments the sheets can be overlapped with an optical tweezer built by an SLM. Displaying different patterns, one can adjust the aspect ratio and the geometry of the tweezer, building the microtrap. Its size on the order of a few μm.

The ^{6}Li manifold Besides transitions between different trap levels there are also atomic excitations present in the system. For experiments different hyperfine levels of the electronic groundstate $2^2\mathrm{S}_{1/2}$ are used. The hyperfine structure of ^{6}Li

[1] ω is an angular frequency, Δ and Γ have to be formulated in the same units, i.e. either angular frequency or frequency

[2] The exact numbers for ^{6}Li can be found in [15]

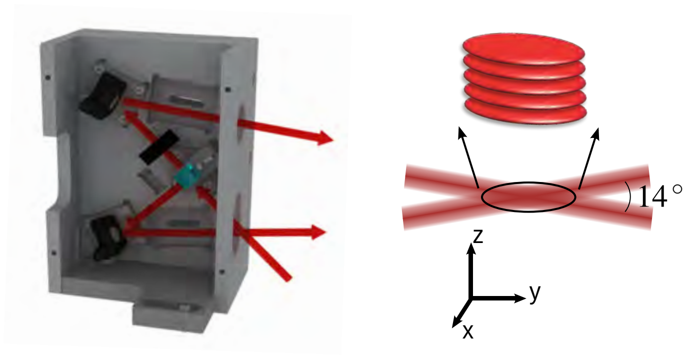

(a) Standing wave trap ("Schielbrille").

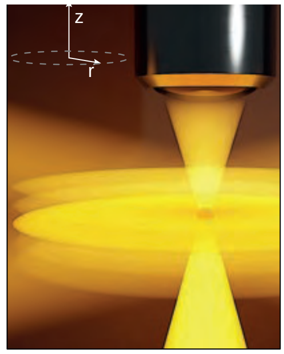

(b) Microtrap/tweezer.

Figure 2.5 Schielbrille (2.5a) and Microtrap (2.5b). In 2.5a two beams are overlapped with an angle of 14° building an interference pattern of "pancake" shaped traps. Taken from [16]. 2.5b shows the overlapped "pancake" trap with a beam from above. This beam comes from a SLM setup belonging to the experiment. In the overlap region the microtrap is formed and can be adjusted by changing the pattern on the SLM. Taken from [13].

is composed of six different sublevels which degeneracy is lifted by the magnetic field. For low fields the total electronic angular momentum $\vec{J}$ and the nuclear spin $\vec{I}$ are coupled such that the electronic groundstate $2^2\mathrm{S}_{1/2}$ splits up into two substate manifolds, defined by the quantum numbers for the total angular momentum F and its magnetic moment m_F. The coupling between the nuclear spin and the total electronic angular momentum varies with the magnetic field strength. In ^{6}Li the nuclear spin and the total electronic angular momentum are already decoupled at fields higher than 200 G (Paschen-Back regime). Therefore, the respective magnetic moment quantum numbers m_J and m_I are good quantum numbers and the electronic groundstate is splitted into two m_J manifolds consisting of three substates with different m_I. These substates are spaced by approximately 80 MHz.

This hyperfine manifold is also used for imaging. In principle the apparatus enables absorption imaging from below the chamber and high resolution fluorescence imaging from above (c.f. fig. 2.3). The imaging setup (c.f. fig. 2.7) consists of a high resolution objective, a dichroic mirror and a PBS. The objective has a numerical aperture of 0.6 and an effective focal length of 20.3 mm providing a resolution of 1 μm. Through the objective passes the fluorescence signal from the chamber (671 nm), the MOT light into the chamber (671 nm) and the light for the optical

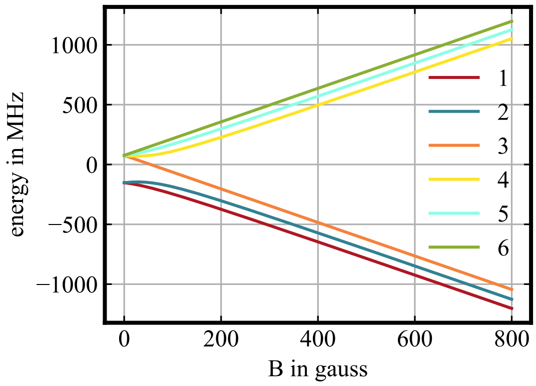

Figure 2.6 Hyperfine manifold of the ^{6}Li electronic groundstate $2^2\mathrm{S}_{1/2}$ for different magnetic fields. In the low field regime the hyperfine coupling is dominant and such the quantum numbers for total angular momentum F and its magnetic moment m_F are good quantum numbers. For higher fields the angular momenta starts to decouple until the Paschen-Back regime is reached and the energies depend on the magnetic moment of the total electronic angular momentum m_J and the magnetic moment of the nuclear spin m_I.

tweezer coming from the SLM (1064 nm). The 671 nm light and the 1064 nm light are combined on a dichroic mirror in front of the objective. Since the MOT light coming from the experimental chamber and the fluorescence light have different circular polarizations, they can be separated on the PBS.

2.1.4 Parametric heating

There are different ways to drive excitations in atomic systems. For imaging, cooling and trapping inner-atomic transitions are used. Light of the frequency corresponding to a transition is sent into the trap, gets absorbed, and excites the atom. Another way of driving excitations is intensity modulation which was also used in our group to drive the Higgs-mode-precursor excitations in [17]. Assuming a light field which builds a first order harmonic trap with a certain noise in intensity can be described by the Hamiltonian

$$\hat{H} = \frac{\hat{p}^2}{2m} + \frac{1}{2}m\omega^2\left(1+\varepsilon(t)\right)\hat{x}^2 \tag{2.10}$$

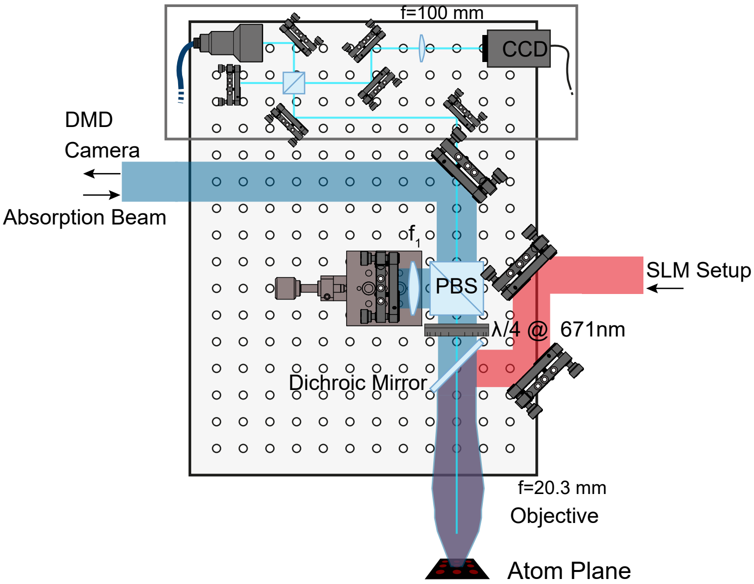

Figure 2.7 Imaging setup. The 671 nm beam, used for imaging, and the 1064 nm beam, used for the optical tweezer, coming from the SLM, are combined on a dichroic mirror. They enter the experimental chamber through the objective (NA = 0.6 and effective focal length 20.3 mmm). For fluorescence imaging, the MOT light can be separated from the imaging light since they have different circular polarizations and therefore one can use a PBS. The optics in the box are used for aligning the objective. Figure from [13]

with the trap frequency ω, momentum operator $\hat{p}$ and position $\hat{x}$, the mass m and the time dependent relative intensity modulation $\varepsilon(t)$. The trap frequency is proportional to the time averaged intensity. A relative intensity modulation leads to another effective trap frequency as described by eq. 2.10. A perturbative treatment using the Dyson series (c.f. [18]) leads to

$$\langle \partial_t E \rangle = \frac{\pi}{2} \omega^2 S_\varepsilon(2\omega) \langle E \rangle \tag{2.11}$$

with the energy E and $\langle \ldots \rangle$ signifying the temporal average. $S_\varepsilon(2\omega)$ is the one-sided power spectrum of the fractional intensity noise of the frequency 2ω. That shows that intensity modulations with twice a trap frequency leads to exponential heating, which means energy increases. Therefore one has to make sure that the intensity modulations of light sources in the experiment are not on the order of the trap frequencies.

2.1.5 Possibilities and limitations of the setup

During the last year, it has been the question how correlations and Cooper-Pairing arises from few-particle physics. In this framework few fermion experiments in the optical tweezer with six to twelve atoms have been performed. This led to the observation of “Pauli-crystals” in a non-interacting two-dimensional harmonic oscillator trap ([19]). These crystals are the visualization of the spatial correlations arising due to Pauli-blocking and the harmonical confinement. Measuring the excitation spectrum of such ensembles for different interaction strengths, the few-body precursor of the Higgs mode was found ([17]).

These experiments used the harmonic oscillator state manifold to observe excitations without being interested in thermodynamic transport properties such that a varying chemical potential was no limiting factor.

In contrast to these experiments, the study of universal behavior of many particle systems requires the observation of bulk properties and therefore a slowly varying chemical potential. As already motivated (c.f. sec. 1), the measurement of bulk properties offers insight in pair fluctuations ([1]), being characteristic for the superfluid phase transition. Therefore, a beamshaping device would be helpful to get rid of potential curvatures over the trap and to create arbitrary trapping geometries.

Additionally the few particle control in combination with a beamshaping device can be used to study transport properties in few-body atomtronic geometries. Few-body Josephson junctions[3] or the coupling of small ensembles to large reservoirs can be realized. In combination with the single-atom resolution of the setup, the counting statistics and particle correlation functions can be extracted.

The first milestone would be the creation of a flat potential with sharp walls in the atom plane. One could use a red detuned, broad Gaussian beam (width $\approx 300\,\mu$m) to built a flat attractive potential. That could be provided by the standing-wave-trap mentioned above (c.f. 2.5a). A strong, sharp confinement is achieved by projecting walls of blue-detuned light into the atom plane building arbitrary geometries. The superposition of these beams results in a flat box potential (fig. 2.8).

[3] Josephson junctions (many body) in cold atom experiments including beam shaping devices were already realized in the group of Prof. Henning Moritz ([20]).

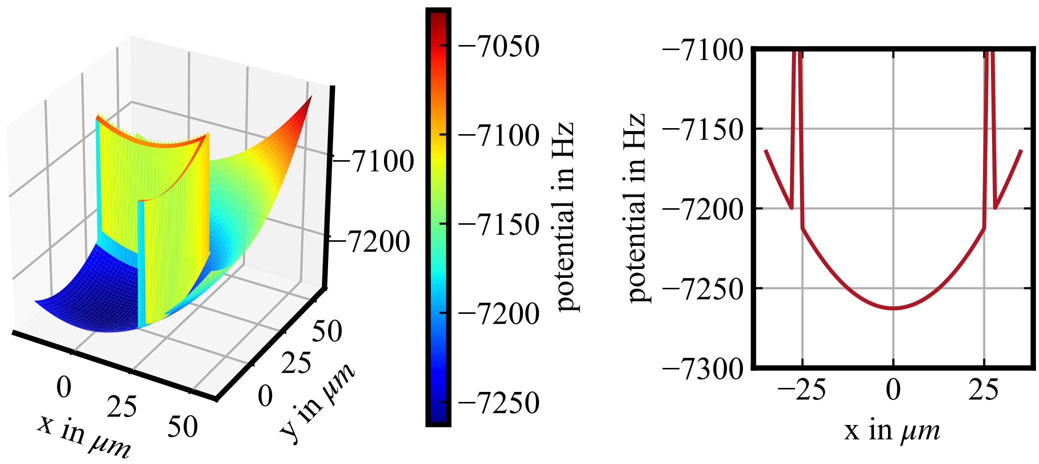

(a) 2D representation of the potential. **(b)** 1D representation of the potential.

Figure 2.8 Model system. A box with side length $50\,\mu$m. In theory one could also equalize the potential bending inside the box which is on the order of $50-100$ Hz leading to a flat box. The attractive potential is created by the Schielbrille (c.f. 2.5a), a 1064 nm beam with a total power of 4 W and a beam waist of $300\,\mu$m. The resonance wavelength is 671 nm.

2.2 Beamshaping

As written in eq. 2.12, one can describe the electromagnetic waves by their amplitude and phase. Creating arbitrary light fields, these two quantities are addressed by either amplitude or phase modulation. Two typical devices for these tasks are digital micro mirror devices (DMD), used in beamers, and spatial light modulators (SLM), used in computer screens. SLMs consists of an array of liquid crystals. Their orientations, influencing the polarization or phase of the light field, are controlled by applied voltages.

In contrast to SLMs, DMDs are amplitude modulators. A DMD consists of an array of single addressable micromirrors (see fig 2.9). Every mirror can be tilted either by $-\theta_{\text{tilt}}$ or $+\theta_{\text{tilt}}$. Usually the optical setup is arranged such that one of the two positionings leads to reflecting light into the further imaging system ("on") while the other position leads to the light being dumped ("off"). This way the DMD serves as a binary amplitude mask.

All in all, there are two main decisions to make. Having direct access to the

Fourier plane enables to account for aberrations and to modulate the amplitude by phase holograms. Secondly one has to decide if one wants work with a DMD or a SLM, having either the amplitude directly accessible or the phase.

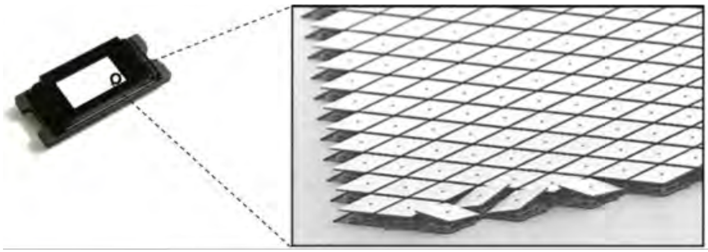

Figure 2.9 The DMD surface under the microscope. Each micro mirror has a width $12\,\mu$m and can be tilted by $\pm 12^\circ$.

Working in the Fourier plane gives access to the phase, no matter if one works with a DMD or a SLM. That means it is possible to account for known aberrations in the system. These aberrations can be determined by evaluating output images using Zernike polynomials and accounted for, by changing the mask in the Fourier plane. Usually SLMs are used in the Fourier plane because otherwise there would be no control about amplitudes in the output beam. Holograms are created by displaying the proper phase pattern in the Fourier plane (e.g. in [21]). This way the SLM takes the incoming light and **redistributes** it over the image plane and in principle no intensity is lost. In practice there are losses due to an imperfect setup and "Fourier plane specific" losses. Since the actual image is a hologram of the pattern displayed on the SLM, imperfect patterns and the discretization of the Fourier plane lead to losses in efficiency.

Devices in the image plane display directly the target geometry and therefore the creation of patterns on the beamshaping device is straight forward. A DMD modulates the amplitude by turning pixels "on" and "off" (tilting the mirrors at $+\theta_{\text{tilt}}$ or $-\theta_{\text{tilt}}$) and therefore **discards** intensity. For Fourier plane setups, this means that the DMD can just display patterns with real-valued Fourier transforms since the phase is inaccessible. In the image plane, the pattern displayed on the device gets directly imaged onto the atoms but it is impossible to account for aberrations. Additionally DMDs are faster than SLMs, since the respond time of the liquid crystals is longer than the micromirror switching time. It takes approximately 100 ms until the liquid crystals reach a stable position and therefore maximal pattern rates are on the order of $\approx 10\,\text{Hz}$[4] due to the finite liquid crystal response time, whereas DMDs

[4] see for example the EXULUS series from ThorLabs

reach pattern rates of up to 20 kHz[5].

2.3 Fourier optics

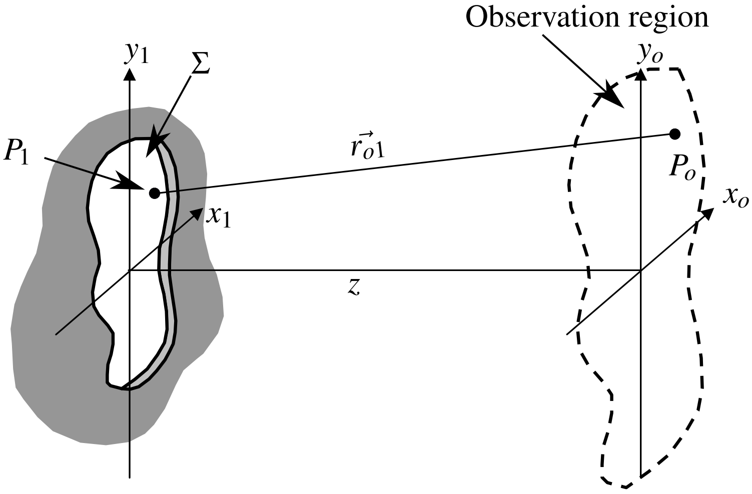

Figure 2.10 Geometry described by eq. 2.14 adapted from [22]. The lightfield passes through the aperture Σ to the observation region.

The situation discussed in this section is shown in fig. 2.10. An adjustable aperture Σ is illuminated by a lightsource. The light travels from the aperture into the image plane or observation region. Having a certain target light field to project onto the atoms, a proper description of the dependence between incoming and outgoing light is needed. Using Fourier optics, one decomposes the amplitude fields in two dimensional mode expansions and looks for propagators between planes normal to the propagation.

Assuming polarized monochromatic light, the light field in a transversal plane at point P and time t can be described by a scalar

$$u(P,t) = \mathrm{Re}[\mathbf{U}(P)e^{-i2\pi\nu t}]. \tag{2.12}$$

$\mathbf{U}(P)$ signifies the *phasor* which depends on the electric field amplitude $U(P)$ and the local phase $\phi(P)$ so that

$$\mathbf{U}(\mathrm{P}) = U(P)e^{-i\phi(P)}. \tag{2.13}$$

[5] see for example the SuperSpeed V-Module from Vialux

ν is the optical frequency such that the speed of light is given as $c = \frac{2\pi\nu}{k}$ with the wavenumber k. u fulfils the wave equation and $\mathbf{U}$ the Helmholtz equation. Following the Rayleigh-Sommerfeldt theory presented by [22] one finds the Rayleigh-Sommerfeld diffraction formula

$$\mathbf{U}(P_0) = \frac{1}{i\lambda} \int\int_{\Sigma} \mathbf{U}(P_1) \frac{\exp(ikr_{o1})}{r_{o1}} \cos(\vec{n}, \vec{r}_{o1})\, ds \tag{2.14}$$

claiming that the field at P_o can be calculated by integrating over the points P_1 lying on the aperture Σ (cf. fig. 2.10). The Rayleigh-Sommerfeld formula is the starting point of the Fresnel-and Fraunhofer approximations, that lead to fourier optics. The idea is to consider the light amplitude in the far field to be able to expand r_{o1} and to simplify the integral. Following the arguments of Fraunhofer and Fresnel one finds that the light amplitude in the far field is proportional to the Fourier transform of the amplitude at the aperture. The Fraunhofer approximation gives

$$\mathbf{U}(x_o, y_o) = \frac{\exp(ikz)}{i\lambda z} e^{ik/(2z)(x_o^2+y_o^2)} \mathscr{F}\{\mathbf{U}\}(f_X, f_Y)\Big|_{f_X=\frac{x_o}{\lambda z}, f_Y=\frac{y_o}{\lambda z}} \tag{2.15}$$

for the field amplitude at the object point (x_o, y_o).

Besides the complex phase, which vanishes when considering the intensity, it is just the Fourier transform of the light field at the aperture. It should be mentioned that the requirement for "far-field" from the Fraunhofer point-of-view is not easy to achieve. Assuming light with a wavelength of 660 nm and an aperture of one inch, one finds that the distance z between screen and aperture has to fulfill $z >> 1540\,\mathrm{m}$[6]. However, by using a lens the "far field" is located in the focal plane of the lens. In the Fourier optics approach a lens is described as an element delaying an incident wavefront by an amount depending on the lens geometry. This additional phase term ensures that the field in the back focal plane can be described in the "far-field". If the lens is set up in a 2f setup, the output amplitude of the light field is

$$\mathbf{U}(x_o, y_o) = \mathscr{F}\{\mathbf{U}\}(f_X, f_Y)\Big|_{f_X=\frac{x_o}{\lambda z}, f_Y=\frac{y_o}{\lambda z}}. \tag{2.16}$$

Note that the phase term which was present in the Fraunhofer approximation in eq. 2.15 cancelled out and the lens provides an exact Fourier transform of the input image.

[6] Fraunhofer approximation assumes that $z >> \frac{k(x_1^2+y_1^2)_{max}}{2}$ holds (cf. [22] or [23])

2.4 Imaging

The final optical setup is planned as two 4f setup in series giving the needed demagnification of approximately 85 and well defined Fourier planes for filtering. With the image in a focal plane of the first lens, it would also be possible to implement the DMD in a Fourier plane or to use a different number of telescopes. For large scale geometric structures as box and tubes, the image plane pattern is straight forward and less vulnerable to computational errors than the Fourier plane hologram. Image plane setups with more or less lenses are inconvenient due to the required demagnification as it will be pointed out in sec. 3.2.1.

To display arbitrary geometries in the image plane, one has to consider the incoming light field $U(\vec{x})$, illuminating the aperture, the mask displayed on the projector $mask(\vec{x})$, defining the aperture and the output light field $U_o(\vec{x})$. The linearity of the wave equations enables us to decompose the incoming light field in point like excitations and to solve the problem for each of them individually. The system response to these excitations is the point spread function (PSF). The output field can be calculated as the convolution of the PSF with the input field (c.f. [22]).

For Image formation, one has to compute the output intensity in dependence of the input intensity. The performance of the optical system is dependent on the coherence properties of the light. The differences between coherent and incoherent illumination can be shown by calculating the output intensity for the two cases.

2.4.1 Coherent and incoherent image formation

Coherence is a term used in many physical contexts such as quantum information, optics and many particle physics. The key ingredient is the capability of different waves to interfere, thus having a well defined phase relation. For our purpose two different kinds of coherence are important, namely spatial and temporal coherence. For qualitative understanding one can assume a plane wave description

$$\Psi(\vec{x},t) \propto \mathrm{e}^{-i(\vec{k}\vec{x}+\omega t)}. \tag{2.17}$$

One identifies two terms defining the phase of Ψ. On the one hand, the phase depends on $\vec{k} \times \vec{x}$ and, on the other hand, on $\omega \times t$. Having a single well defined $\vec{k}$ and ω every point in space has a defined phase relation to every other point in space for all times t. Spatial and temporal incoherence deals with the case having different values for $\vec{k}$ (spatial) or ω (temporal) in the system.

In this thesis **spatial** incoherence describes that the coherence capability i.e. the interference contrast depends on the **spatial** distance of two object points which emit waves interfering with each other. **Temporal** incoherence describes that the interference contrast depends on the **temporal** delay of paths interfering with each other. Following these definitions a coherence length l_c is connected with spatial incoherence and the coherence time τ_c with temporal incoherence, but since time delay and path differences can be translated into each other via the speed of light c, the terms are usually used in both contexts.

To quantify incoherence the coherence function

$$\Gamma(\vec{r}_1,\vec{r}_2,\tau) = \langle U(\vec{r}_1,t+\tau)U^*(\vec{r}_2,t)\rangle_T \tag{2.18}$$

is used. It is the time average over some time T of the product of the amplitude field U at time $t+\tau$ and point $\vec{r}_1$ with the complex conjugated amplitude field at time t and point $\vec{r}_2$. The quantity describes the intensity of two fields separated by $\vec{r}_1 - \vec{r}_2$ and delayed by τ measured over a time T which could be for example the exposure time of a camera.

As figured out above, for image formation one analyzes the input object point wise. The final measured quantity, the light intensity in the image (i) I_i is given as the sum of all impulse responses to the input field and its complex conjugate and depends on the image coordinates (x_i, y_i). Since the camera has a finite exposure time, the time dependence of the input/object fields (o) has to be taken into account and the time average over the exposure time T is calculated. This reads as

$$\begin{aligned} I(x_i,y_i) = \int\int\int\int_{-\infty}^{\infty} &\mathrm{PSF}(x_i - x_o', y_i - y_o')\mathrm{PSF}^*(x_i - x_o'', y_i - y_o'') \\ &\left\langle U(x_o', y_o'; t)U^*(x_o'', y_o''; t)\right\rangle_T \, dx_o' dy_o' dx_o'' dy_o''. \end{aligned} \tag{2.19}$$

In the perfectly coherent case the time-average is of no concern because the impulse responses vary in unison and their relative phases are constant. Therefore, the time-average drops out and the output intensity is

$$I(x_i,y_i) = |(U_o * \mathrm{PSF})(x_i,y_i)|^2. \tag{2.20}$$

Using the convolution theorem this shows that the image amplitude depends linearly on the input amplitude as $\sqrt{I_\mathrm{i}(f_\mathrm{X}, f_\mathrm{Y})} = U_\mathrm{o}(f_\mathrm{X}, f_\mathrm{Y}) \times \mathscr{F}(\mathrm{PSF})$.

For perfectly incoherent imaging the impulse responses vary not in unison but statistically independent from each other and the temporal average of phasors at different positions is always zero. All correlation terms drop out and

$$\left\langle U(x_o', y_o'; t)U(x_o'', y_o''; t)\right\rangle_T = U(x_o', y_o')U(x_o'', y_o'')\delta(x_o' - x_o'', y_o' - y_0'') \tag{2.21}$$

holds. Therefore, the incoherent image is calculated as

$$I_\mathrm{i}(x_i, y_i) = \left(|\mathrm{PSF}|^2 * I_\mathrm{o}\right)(x_i, y_i). \tag{2.22}$$

In contrast to the coherent case, the incoherent image intensity depends linear on the object intensity as $I_\mathrm{i}(f_{\mathrm{X},}, f_\mathrm{Y}) = \mathscr{F}(|\mathrm{PSF}|^2) \times I_\mathrm{o}(f_\mathrm{X}, f_\mathrm{Y})$.

2.4.2 Performance of coherent and incoherent imaging

The performance of the coherent and incoherent imaging systems is different. Since the benchmark for the DMD setup is the creation of a box with sharp edges, the differences between coherent and incoherent imaging with respect to sharp features and the spatial frequency spectrum are important. Therefore, image formation of two different setups is simulated. The model system is a 2f setup with a circular aperture in the Fourier plane. For qualitative statements the exact numbers concerning NA and focal length are not important as long as they are hold constant. The

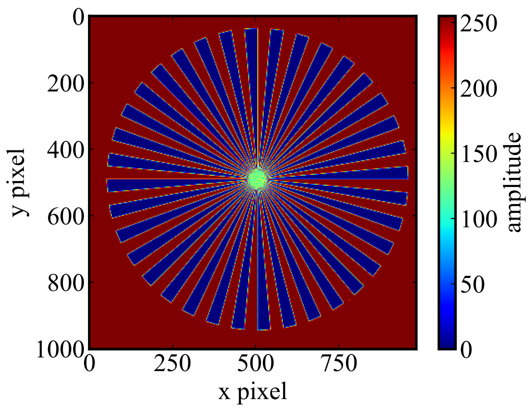

Figure 2.11 Siemensstern

Siemensstar is an appropriate image to show the spatial resolution of an imaging system since the spatial frequencies of the features increase from inside to outside (c.f. fig. 2.11).

In fig. 2.12 the results for coherent and incoherent imaging are shown. Due to limited spatial resolution the spokes close to the center are not resolved anymore. The resulting circle of constant amplitude around the center demonstrates the spatial resoluton of the imaging system. Comparing the incoherent with the coherent case, one recognizes that the spatial resolution of the incoherent imaging system is larger, but the edges are less sharp, so contrast is worse. Additionally, the incoherent image seems to be smoother than the coherent image which shows spikes in amplitude next to edges. The reason for these features are the different image formation pro-

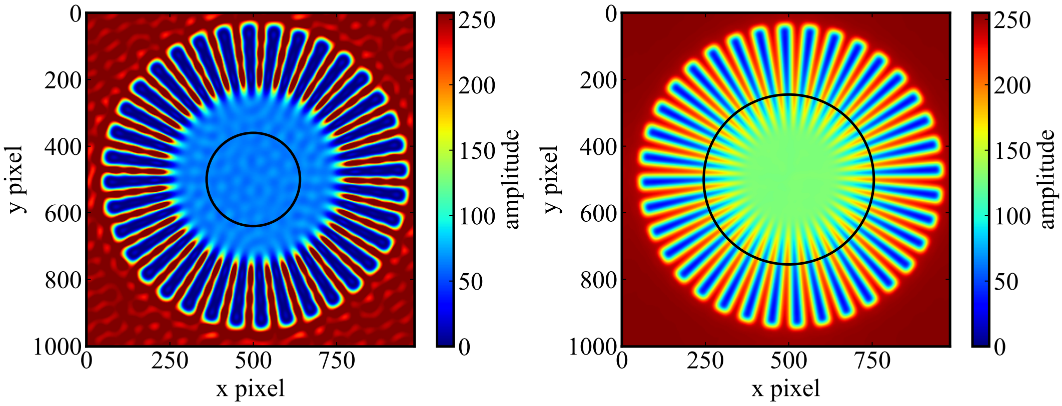

(a) Coherent output intensity. **(b)** Inoherent output intensity.

Figure 2.12 The figures show the calculated Siemensstar image(c.f. 2.11) for both a coherent (left) and incoherent (right) light source. The spatial spokes close to the center are not resolved anymore due to their higher spatial frequency. The circles show the not resolvable area of the oppositional image formation process. Comparing the incoherent with the coherent output, one recognizes that the spatial resolution of the incoherent system is larger in this sense.

cedures. As already pointed out, in the coherent imaging formalism, one computes the Fourier transformed output **amplitude** by multiplying the Fourier transformed PSF, which is the aperture in Fourier coordinates, with the input field. Subsequently one computes the output amplitude by Fourier transforming in the image plane and takes the absolute square to get the output intensity. The Fourier transformed PSF is called the “coherent transfer function” (CTF, c.f. fig. 2.13).

In the case of perfectly incoherent imaging the procedure is different. As described by eq. 2.4.1 one calculates the output **intensity** by taking the Fourier transform of the squared PSF and multiplying it with the Fourier transformed intensity. The Fourier transform of the squared PSF is called “optical transfer function” (OTF). Since the aperture is rotaional invariant, it is sufficient to show a cut along the y-axis as shown in fig. 2.13a.

Since the mask is binary, the CTF is also either one or zero with a certain cutoff frequncy depending on the size of the aperture. In contrast to the CTF, the OTF de-

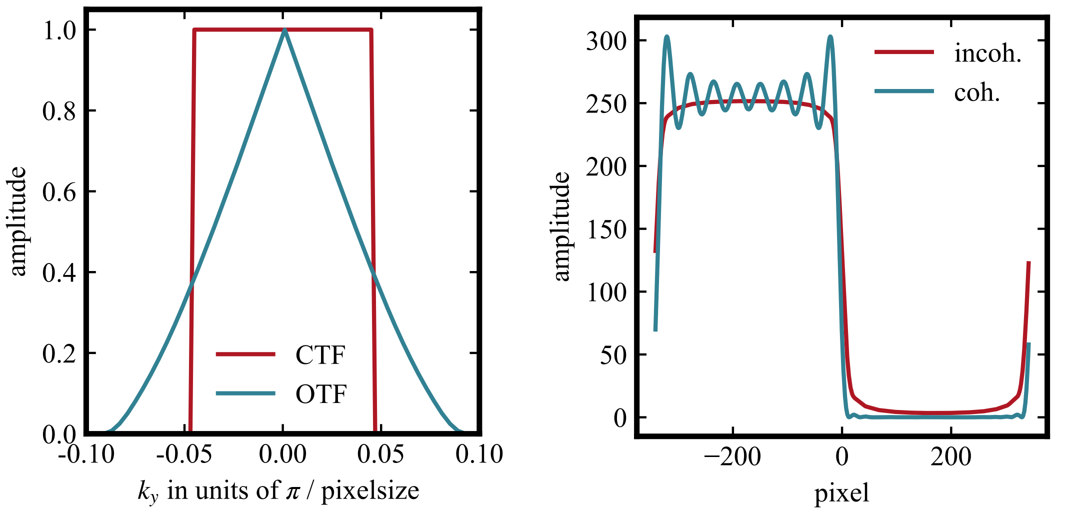

(a) Optical transfer functions relevant for the image formation. The cutoff frequency defined as the spatial frequency, where the corresponding transfer function drops to zero. The cutoff frequency in the incoherent case is twice as large as the coherent cutoff. In contrast to the CTF, the OTF decreases with increasing spatial frequency.

(b) 1D image intensity for a sharp edge. Coherent imaging leads to characteristic speckles near the edges. The spatial frequency depends on the chosen aperture diameter. Incoherent imaging leads to washed ou speckles and smooth edges.

Figure 2.13 Coherent and Incoherent image formation.

creases with increasing spatial frequency and drops to zero at twice the CTF cutoff frequency. In general it is not possible to compare the performance of incoherent imaging with coherent imaging based on the transfer functions because they do not deal with the same quantity. The CTF transfers the object amplitude into the image, while the OTF transfers the object intensity. For the Siemensstar, the mask is completely real valued and the spatial resolution can be compared based on the transfer functions[7]. This explains the different radii in fig. 2.12. The mentioned spikes in the coherent image are a result of the sharp frequency cutoff of the CTF.

A 1D cut across an intensity step reveals the differences between coherent and incoherent imaging[8]. In fig. 2.13b the difference between coherent and incoherent imaging is clearly visible. The coherent image shows the characteristic oscillation

[7]For complex valued masks, this is different

[8]The aperture was also rotational symmetric and placed in the Fourier plane.

near the edge and in the incoherent case it is washed out.

Regarding fig. 2.12 and fig. 2.13 it becomes clear that the comparison of coherent and incoherent imaging is not trivial. On the one hand, one can argue that the spatial resolution of incoherent imaging systems is larger since it is possible to resolve inner regions of the Siemensstar, that are already blurred in the coherent case. On the other hand it is visible that the contrast at sharp edges is better in coherent systems and therefore it seems that this is due to higher frequencies being present in the coherent imaging process. This ambivalent behaviour is due to the different shapes of the transfer functions (c.f. 2.13a). The coherent has less spatial frequencies included but all have the same weight. In the incoherent case, there are twice as many spatial frequencies included but their weight decreases with increasing spatial frequency.

2.4.3 Partial Coherence

Real lightsources behave neither completely coherent nor completely incoherent, but partially incoherent. Therefore, the coherence function depends on the distance between considered object points and calculating the image via eq. (2.19) gets complicated. The integrations over the two fields in eq. (2.19) get coupled by a kernel depending on the size of the coherence function. For a qualitative understanding one can imagine the partially coherent field as a composition of coherent fields with different weighted $\vec{k}$. The Fourier transform of the amplitude in the Fourier plane is the product of the Fourier transformed input field and the Fourier transformed PSF which is just the rescaled aperture. Assuming a binary mask, e.g. a circular screen, the Fourier transformed PSF is again a binary mask with a certain cutoff frequency. The different $\vec{k}$-modes in the partial coherent field hit the Fourier plane at different positions and get therefore filtered differently. Following this interpretation one could model partially coherent light by weighting and shifting a mask in the Fourier plane for different modes. Qualitativly I would expect that high frequency components get washed out, so the ringing next to edges would be reduced. In analogy to the completely incoherent case areas at smaller radii would be resolved. For quantitative statements one needs to know the exact weights of the different k-modes.

Experimentally temporal incoherent light is achieved by using a broad light source consisting of many different coherent modes. Using a Michaelson interferometer and varying the time delay between the two paths by changing one arm length, one can observe the characteristic decrease of the interference contrast for an increasing time delay followed by revivals at later times. Revivals are present because each of the different modes is still phase coherent and when all the phases are at an integer multiple of 2π they add up constructively. Our common clocks represent in this sense a system with three different modes (one for each hand) and two constructive revivals per day, namely at 12 a.m. and 12 p.m.

For using spatially incoherent light there are different approaches. One can create arrays of delayed rays such that they are not coherent which each other any more [24]. Other approaches include SLM's and averaging over several images (c.f. [25]) or fast moving and therefore time-averaging apertures in the Fourier plane (c.f. [26] or [27]). But these approaches rely on time-averaging and therefore they assume that all relevant timescales of their systems are well above the timescale of the averaging process.

2.4.4 Conclusion

All in all, using incoherent light is preferable, because sharp features get smoothed out. This is a result of the decreasing transfer function for increasing spatial frequencies. All dirt or dust particles on the optics are sharp features, such that using incoherent light would lead to smaller intensity gradients in the atom plane and to less disturbance of the optical potential. Perfectly incoherent lightsources are not available and as pointed out in this section, the generation of partially incoherent light needs either a moving Fourier plane aperture, which we cannot realize since this modulation would have to be on the MHz scale, to be faster than all timescales in the experiment, and other approaches are rather money- or time-consuming. Therefore, we decided to use a laser with a relative large bandwidth (c.f. sec. 3.2.2).

3

Setting up a DMD

3.1 DMDLC 9000

In this chapter the technical details of the chosen digital micro mirror device (DMD) are described. Most important points are the pattern rate and upload speed of pattern sequences.

3.1.1 Overview

Texas Instruments offers a broad range of DMDs. We decided to buy the device with the largest screen (2560×1600), the DMDLC 9000. A large number of pixels offers a large drawing area and many degrees of freedom, which can be used for grayscaling or creating detailed geometries. The disadvantage is, that larger screens require more data to transmit and therefore the maximal pattern rate is reduced.

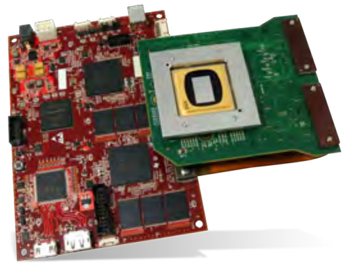

Figure 3.1 DMD Lightcrafter 9000 Evaluation Module from Texas Instruments. The module consists of two parts, connected with flex cables. One is the board with the DMD itself and the other is the PCB board with the controllers and the memory. Picture from [28].

The device consists of two parts connected with flex cables (see fig. 3.1). One part is the DMD board, that contains the micro mirror array. The front side is dominated by the large screen embedded in a metal frame. On the screen one finds the micromirror array (c.f. fig. 3.2). For the array there are two different kinds of arranging the micromirrors, either in a diamond or a rectangular pattern configuration.

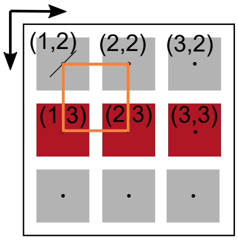

(a) Standard micromirror arrangement.

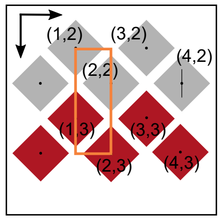

(b) Diamond pattern arrangement

Figure 3.2 Possible micromirror arrangements. On the left, the arrangement of the DMDLC9000 is shown. The micromirrors are aligned with array edges. Since the tilt axis lies along the diagonal of the micromirrors, we rotate the DMD by 45° before mounting it to hold the beam in a horizontal plane with respect to the table. Another possible arrangement is the diamond pattern. There, the DMD does not have to be rotated but the coordinate system leads to a distortion by a factor of $\sqrt{2\pi}$.

On the DMDLC9000 the micromirror edges are aligned with the respective coordinate unit vector (arrows in fig. 3.2, rectangular pattern). Therefore the horizontal and vertical distances between pixels are given by the micromirror pitch. If the micromirrors are arranged in a diamond pattern[1], a distortion of the uploaded pattern is present. As pointed out in sec. 2.2, the mirrors can be rotated in the “on” or the “off” position. The rotation axis is the diagonal of the micromirrors. If one wants to hold the “off-beam” and the “on-beam” in the horizontal plane, the rotational axis has to be vertical. Therefore, a screen with a rectangular pattern has to be rotated by 45°, while this is not case for the diamond pattern.

The DMD does not have to be rotated but due to the diagonal alignment, the pattern is distorted in one direction. On the backside one finds a heat sink which should be kept uncovered due to the noticeable amount of heat emitted. The second part is the PCB board consisting of two controllers and the memories.

The internal structure scheme is shown in fig. 3.3. The DMD itself (DLP9000 WQXGA) consists of 2560×1600 pixels with a mirror pitch of 7.6 μm which gives a total mirror array size of 12 mm $\times$ 19 mm. Internally the screen is divided in two independent screens of 1280×1600 pixels, the Master screen and the Slave screen, controlled by the respective controller. Each controller has its own flash memory on the PCB board.

[1] That will be the case for the DMD used in sec. 3.3.2

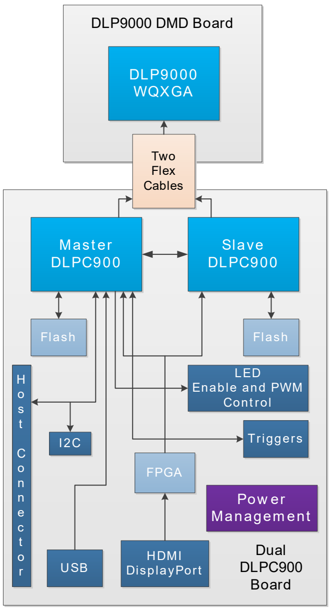

Figure 3.3 Schematic architecture of the DMDLC 9000 from [28]. The module has inputs for trigger, HDMI, USB 1.1 and I2C. Output lines are for triggering and LED control. The screen is divided into two sub screens, each controlled by its own controller (Master and Slave). More details can be found in the manuals [28] and [29].

The evaluation module has three possible data inputs which are USB 1.1, I2C and HDMI. Via these channels the user can send commands and image data to the controllers. Additionally the evaluation module has a trigger in-and output and a LED control line.

Two different kinds of data are transmitted to the evaluation module. On the one hand there are configuration commands, which set timings, bit depths, display modes etc.. On the other hand, there are the image data itself consisting of binary values for each individual image pixel. All data, sent via USB, is transferred to the Master controller, which forwards the image data of the Slave screen to the Slave controller. Subsequently the configuration commands for both sub screens are processed by the Master controller. Afterwards the image data is sent in parallel from the controllers to the respective screens. As soon as the data transfer is finished, the selected display mode starts. The delay time between the first command, sent to the DMD and the display of the pattern depends on the pattern and the selected mode. This will be discussed in the following section.

3.1.2 Communication protocols

To transmit commands and data one uses one of the input lines: USB, I2C or HDMI. The HDMI mode can only be used for video streaming. Thus we decided to use the USB HID protocol, which is executed via a Python program adapted from the Linux-only version for a similar device from Texas Instruments in [30].

For the exchange of messages with the DMD, the pywinusb Python package [31] was used. Image and command data are sent as hexadecimal digits. The programmer guide [29] provides a dictionary for all relevant USB-commands. Since the software is designed for displaying movies in 24 bit RGB[2], all the images have to be sent in this format. Therefore the data transfer is very inefficient for binary patterns. Each mirror can be in just two states, either "on" or "off", but for each pixel 24 bits are transmitted instead of one. Further details about the USB-protocol can be found in the Appendix.

3.1.3 Pattern rates and bit depth

The DMD Lightcrafter evaluation module is not desingned for cold atom experiments, but to be included in commercial beamers. Therefore, timings and data structure are optimized for coloured images and videos. Since cold atom systems can be heated by modulations of the intensity in the kHz range (see sec. 2.1.3 and 2.1.4), the exact dynamic behaviour of the micromirrors is important. The pattern rate is limited by the mechanical properties of the micromirrors and by the upload speed of image data from the controllers to the screen. That results in a minimal exposure time for each pattern, since the pattern rate is finite.

The mechanically given minimal exposure time can be deduced from the time, the intensity of a light beam, which is reflected on the screen, needs to stabilize after a switching process of the micromirrors. This is shown in fig. 3.4.

Since the DMD is designed to be part of a complete beamer setup including a lightsource, it is also possible to control an illumination module with the DMD via the LED outputs. In this way the pattern display gets synchronized with the illumination module. With red, green and blue light, colored images are created by binary amplitude mixing. It suffices to display single images fast (kHz scale), such that our eye is not able to distinguish them any more and averages over them. As a result, we experience a certain depth of colour.

Each pixel gets illuminated eight times per colour, such that the 8 bit representation, offering 256 different intensity levels, is encoded in the corresponding illumination times. To achieve 256 intensity levels, the exposure times have to be

[2]Three colors and with 8 intensity levels each.

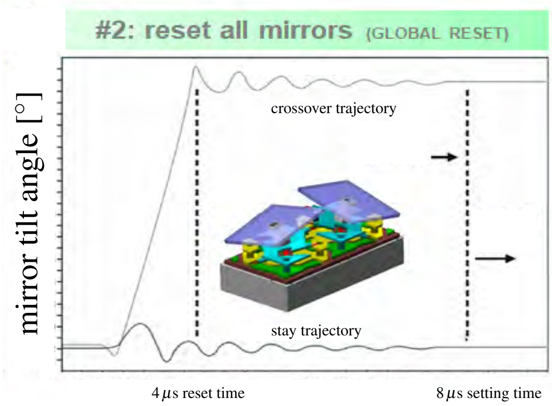

Figure 3.4 Mirror switching and mechanical design of the micro mirrors. The mirrors are located on a spring giving them enough flexibility to switch between the on and off position. The movements of the mirrors are initiated by electrostatic forces due to charges on an electrode sitting behind the landing tips. Each micro mirror has a CMOS memory beneath which contains the mirror position in the next image. Since the mirrors are switched mechanically and undergo a damped oscillation after switching a delay between different patterns is needed. This delay is approximately 12 μs as can be seen in the left figure. The image was sent by a Vialux developer during a discussion.

weighted with 2^0, 2^1, 2^2, ..., 2^7. In this way the 8 bit representation of the image is represented by eight binary patterns.

Nevertheless it is not possible to calculate the maximal binary pattern rate of DMDs by inserting the frame rate and the colour depth.

The DMDLC 9000 supports up to 120 Hz with 24 bit RGB. A naive calculation would lead to a minimal exposure time of $\frac{1\,\mathrm{s}}{120\times256\times3} = 10\,\mu$s for each mirror and a binary pattern rate of 92 kHz. However, in reality the minimal time, a pattern is displayed, is 105 μs. The high frame rate is achieved by modulating the illumination on a shorter time scale. That means, that the mirrors always stay in their position for at least 105 μs, but they are not illuminated the whole time. Dark times are added, such that the exposure time is not limited by the movement of the mirrors, but by the switching time of the light engine. In this way the minimal exposure time can be below 105 μs and higher frame rates are achieved.

3.1.4 Display modes

Four different display modes are supported by the module: the "Pattern-On-The-Fly mode", the "Video mode", the "Video pattern mode" and the "Pre-Stored pattern mode". The video-modes displays videos, streamed via HDMI. Therefore one relies on the GPU for displaying movies and it is complicated to time the displayed movie sequence from the GPU with the experiment. In addition the pattern creation would be complicated, since the DMD-software does not display the RGB patterns in the given order but "these bitplanes, time slots, and color frames are shuffled and interleaved within the pixel processing functions of the DLPC900 controller" (c.f. [29] p. 43).

The "Pre-Stored pattern mode" works with patterns, which were delivered with the firmware of the module and changing these patterns would require to update the firmware.

Therefore the "Pattern-On-The-Fly" mode was chosen. In this mode the exposure time, the dark time (time between patterns) and the bit depth of each pattern can be set separately. Additionally it is possible to change the pattern at a well defined point in time, using external triggers. The trigger output of the DMD enables us to time subsequent steps with respect to pattern changes. The minimal possible exposure time for one-bit patterns is $105\,\mu$s. A big disadvantage of using single pattern modes is, that it cannot be used together with HDMI, because this mode is designed for debugging purposes and thus just supports USB 1.1.

Additionally, due to the internal software structure, every image has to be uploaded in 24 bit RGB format. For one bit images that means that every pixel is set by sending either three times 0b00000001 or three times 0b00000000 instead of 0b1 or 0b0. Since single images contain 2560×1600 pixels in RGB format, one has to upload $3 \times 2560 \times 1600$ bytes per pattern. Assuming only the image data without any command bytes and a transfer rate of 64 kB/s[3] that gives $\frac{2560\times 1600\times 3\times 1.04\,\text{bytes}}{64000\,\text{B}/s} = 200\,\text{s}$[4]. In practice I observed upload times two to three times longer, resulting in delays of ten minutes due to data upload. This is not feasible, because adjusting gets extremely time consuming. To solve this issue, we decided to use another DMD provided by Vialux which will be introduced later.

To conclude, the general procedure is to upload all patterns of a sequence in the Flash-memory of the corresponding controller and to define the look-up table (LUT), which contains all specifications for the patterns. These specifications are the bit depth and all settings for triggers, in-and output signals as well as the display mode. As soon as the upload is completed, one can start the sequence. It is possible

[3] maximal possible data transfer rate using USB HID protocols.

[4] The factor of 1.04 accounts for header bytes and command bytes transporting no image data.

to change look-up entries of already uploaded sequences, but changing patterns or adding patterns is not possible without reuploading the whole sequence. That means that every sequence has to be uploaded in advance, such that no automatic feedback algorithm can be used, because each adjustment requires a reupload of the whole sequence.

3.1.5 Encoding

The module offers two kinds of data compression to speed up the upload in the “Pattern-On-The-Fly” mode. Either Run-Length-Encoding (RLE) or Enhanced-Run-Length-Encoding (ERLE) can be used. The idea of these modes is to look for repetitions in the pixel values. Instead of defining 100 even pixels separately by 300 bytes one can describe them by five bytes. One byte signals that the encoding mechanism is used, one gives the number of repetitions and the last three give the pixel value (in 24 bit RGB format). RLE just encodes repetitions in the same line and ERLE encodes repetions per line and per column. This way patterns displaying large scale geometries such as boxes, lines or binary potentials can be uploaded much faster ($\approx 6\,$s per pattern), which is still to slow for dynamic adjustments, because it would increase the cycle time of the experiment approximately by a factor of two.

3.1.6 Flickering

In general it is recommended to switch the patterns as often and as balanced as possible, such that the time, the mirrors are in the “on” and “off” positions, are approximately equal. If the mirrors stay in one position for long times, it is possible that they get stuck. Therefore a flickering function was implemented by the manufacturer. Every $105\,\mu$s the mirrors get released globally, such that they are all undefined giving rise to kHz intensity noise on the reflected laser beam. For our experiment this is very problematic because that would lead to heating of the atomic sample, as already observed in other experiments, like [32]. Klaus Hueck developed an electric circuit for the DMDLC 6500 [33], which interrupts the signal line, which carries the trigger for the global release on the chip. This procedure was adapted for our model but our controller got damaged. Digital Light Innovations provided a software workaround, which could not be checked yet. Further details about the circuits and the software solution can be found in the Appendix (c.f. sec. 5.2). Besides of that, the DMD, provided by Vialux (c.f. sec. 4), offers control about the timing of the mirror releases such that is not an issue.

3.1.7 How to use the DMDLC 9000

The main aspects, which are important for the experimental procedure are the pattern rate, the upload speed and the control of the DMD.

In the context of a cold atom experiment, the DMD has to be used in a single pattern mode (“Pattern-On-The-Fly mode”), such that the experimentalist has to upload the whole sequence in advance and no spontaneous adjustments are possible. The upload speed is limited to maximally $64\,\mathrm{kB/s}$[5] which makes it impossible to use uncompressed images, because they need upload times of approximately ten minutes. Large scale geometries can be uploaded in $6\,\mathrm{s}$, which is still too slow for dynamical adjustments.

Sequences can be triggered externally and pattern rates of up to $9.5\,\mathrm{kHz}$ are possible. Nevertheless, in the original configuration the device is not usable for static patterns, because the DMD releases its mirrors every $105\,\mu\mathrm{s}$, which let them undefined and leads to kHz intensity noise.

Due to all these limitations we decided to buy a DMD from Vialux, which will be introduced later in the conclusion of this thesis.

3.2 Design considerations

In sec. 2.1.5 physical capabilities of a DMD setup were discussed. A first target system will be introduced in the following chapter and an adapted setup will be presented. We decided for the beamshaping device, a DMDLC 9000 from Texas Instruments, such that the magnification and the geometry of the setup has to be chosen with respect to the physical parameters of the target system and the technical details of the DMD. Important parameters are the size of the micromirrors, the size of the target system and the needed intensities in the atom plane. Additionally one has to decide on the laser, one wants to use. The important quantities are the laser power, the wavelength and the degree of coherence (fig. 3.5).

3.2.1 First target system

For current experiments with a large number of atoms ($\sim 10^4$) the standing wave trap (c.f. fig. 2.5a and [11]) is used. The trap is created by a $4\,\mathrm{W}$ Gaussian beam at $1064\,\mathrm{nm}$. The waists in the focal plane are $w_{\mathrm{hor}} = 600\,\mu\mathrm{m}$ and $w_{\mathrm{vert}} = 75\,\mu\mathrm{m}$ [35]. According to eq. (2.8) this results in an attractive Gaussian shaped 2D trap with a trap depth of $\omega_z \approx 7.3\,\mathrm{kHz}$ and radial trap frequencies on the order of $15\,\mathrm{Hz}$.

[5] Even lower transfer rates ($\sim 30\,\mathrm{kB/s}$) were observed.

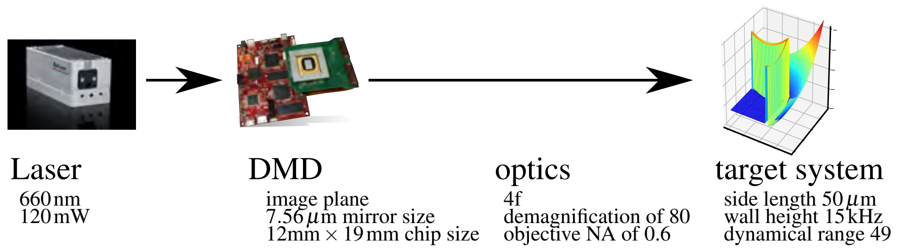

Figure 3.5 The imaging system will consist of a blue detuned laser, illuminating the DMD. The subsequent optical system demagnifies the beam such that the target geometry is projected onto the atoms. Photos from [28] and [34].

The geometrical size of the standing wave trap gives a scale for the first target system which is a box of side length $50\,\mu$m. The plan is to use the DMD setup to project additional potentials onto the standing wave trap to shape the trapping potential in the 2D plane.

The scale of the inter-atomic spacing is given in eq. (2.1.1) and is chosen such that the system is dilute enough to be treated as a quantum degenerate system. The given inter-atomic spacing corresponds to an atom density on the order of $1/\mu\text{m}^2$. To be treated as a closed box, the system walls have to be high enough to make sure, that no relevant tunneling processes out of the box appear. The probability for tunneling of a particle with mass m and energy E through a potential barrier with the height of V_0 and thickness d is given as the absolute square of the transmission amplitude $S(E)$ [36]

$$|S(E)|^2 = \frac{1}{1+(1+\frac{(V_0-2E)^2}{4E(V_0-E)})\sinh^2(d\sqrt{2m(E-V_0)}/\hbar)}. \tag{3.1}$$

For 2D samples the Fermi energy

$$E_F = \frac{\hbar^2 \pi n}{m}, \tag{3.2}$$

depending on the particle mass m and the density n, sets the energy scale. With the

Fermi-velocity v_F and the boxsize of $50\,\mu\mathrm{m}$ a loss rate d_tN can be calculated via

$$d_tN = 2\frac{v_\mathrm{F}}{50\,\mu\mathrm{m}} \times |S(E_\mathrm{F})|^2. \tag{3.3}$$

The wall thickness and wall height has to be chosen, such that the tunneling probability is low. Choosing the wall thickness as $2\,\mu\mathrm{m}$ and the a wall height as $3\,E_\mathrm{F}$ is reasonable, since the lossrate for a ^{6}Li particle of mass 6 u and energy $E = E_\mathrm{F}$ would be 0.003 atoms/s, which is low enough to be neglected. The Fermi-energy of such a sample is on the order of 5 kHz, so the wall height corresponds to approximately 15 kHz. This can be achieved by superimposing a blue detuned beam with the red detuned beam of the current ODT (fig. 3.6).

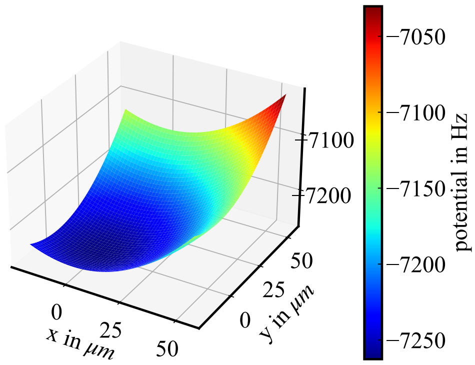

(a) Attractive potential.

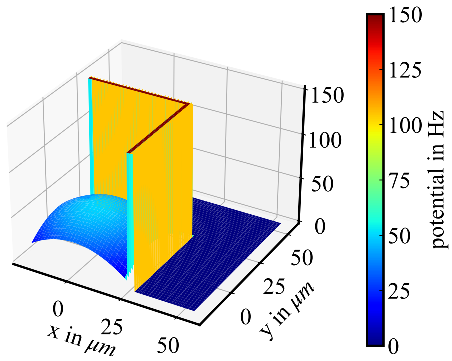

(b) Repulsive potential.

Figure 3.6 The potential landscapes that will be prepared with the setup. The attractive potential is created by a 660 nm beam and the repulsive by the standing wave trap at 1064 nm. The wall height is cut to be able to show the small potential variations in the center.

If one wants to equalize the harmonic shape of the attractive potential, precise local control over the beam intensity will be needed. In general this is done by grayscaling the intensity. The dynamical range or intensity depth quantifies the number of available intensity levels[6]. It is not possible to do binary temporal amplitude mixing, since the DMD provides maximally pattern rates of 9.5 kHz which is too slow. This frequency is very close to the energy scales of trapped sample (z-confinement and Fermi-energy, see ch. 2.1.4 and ch. 2.1.3). Another way to achieve

[6] The PSF is illuminated by a certain area on the DMD. The dynamical range/intensity depth is the size of this area in pixels

grayscaling is to use an imaging system, which cannot resolve single mirrors on the DMD. For 2f setup, imaging an infinitesimal small spot gives the PSF of the system. With a circular aperture in the Fourier plane the intensity pattern in the atom plane is an Airy disk of radius

$$r_{\mathrm{PSF}} = 1.22\frac{\lambda}{2\mathrm{NA}}, \tag{3.4}$$

depending on the chosen wavelength λ and the numerical aperture NA. The resolution of an imaging system is given by this radius.

With a given demagnification one can calculate the size of a perfect image of a DMD pixel in the atom plane. If the size of single mirrors is below the resolution limit, they will not be resolved. Therefore several mirrors will illuminate one PSF and its brightness can be controlled by the number of "on"-pixels in a certain area, smaller than the resolution limit, on the DMD. Propagating a δ-excitation from the atom plane to the DMD and counting the number of pixels which are illuminated, gives the dynamical range n_{d}.

The numerical aperture of the imaging system is limited by the objective used in the experiment ($NA = 0.6$) (c.f. [13] and fig. 2.7) and he mirror size of the DMD is $7.56\,\mu$m. In an imaging system with a certain demagnification M, one finds the dynamical range n_d by comparing the size of the Airy-disk with the demagnified pixel size, which gives

$$n_d = \left(\frac{1.22\lambda \times M}{2NA \times 7.56\mu\mathrm{m}}\right)^2. \tag{3.5}$$

On the one hand, one wants to achieve a large dynamical range, which requires a large demagnification. On the other hand one wants to create systems on the scale of $50 - 100\,\mu$m with the given chip. Large demagnifications mean, that more pixels are required. Therefore, one has to find a compromise between grayscaling and system size, which led us choose a dynamical range around $7 \times 7 = 49$. Without any additional aperture in the beam path one can read off the dynamical range corresponding to a certain magnification in fig. 3.7. A grayscaling depth of 49 would correspond to a demagnification of 80 which is reasonable since the box of side length $50\,\mu$m in the atom plane would correspond to approximately 550 mirrors on the DMD.

For the optical system a telescope setup with the objective as the last lens is used. On needs at least two telescopes for the desired magnification of ≈ 80, since a single telescope setup would require a non-standard 1600 mm lens between the DMD and the objective. Therefore the two telescopes consist of achromatic 2 inch lenses with focal lengths of 500 mm, 300 mm and 1000 mm. To minimize aberrations achromats

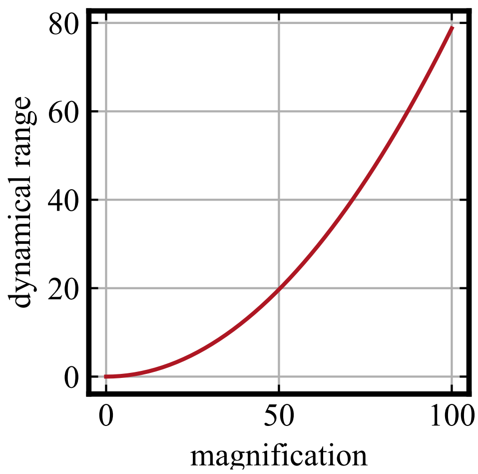

Figure 3.7 Greyscaling depth in dependence of the magnification. The number of mirrors illuminating one PSF is given by the dynamical range.

with focal lengths $> 150\,\mathrm{mm}$ were chosen.

3.2.2 Lightsource

After deciding what imaging setup and DMD are going to be implemented, one has to choose an appropriate lightsource. The first, most important choice is the wavelength of the laser (c.f. eq. 2.8). Other ^{6}Li setups work with wavelengths of 532 nm which requires laser powers on the order of a few Watts [33]. Since the required power is proportional to the detuning, one can reduce the amount of needed power by reducing the detuning. To this end, we decided to install the iBeam-SMART-660-S laser from Toptica. It emits light centered at 660 nm and claims to reduce "speckles"[7] by emitting light with a small coherence length. The laser is a free running diode laser with output powers of up to 130 mW. By connecting the laser to an analogue signal, the laser can be pulsed with a rate of up to 1 MHz. The module has an active temperature control which can be tuned around the operating temperature.

The used atomic resonance in ^{6}Li is at 671 nm. The needed laserpower for a certain optical potential using light at 660 nm is 5 % of the needed laserpower using light at 532 nm. This is shown in fig. 3.8, where the needed laserpower for a certain optical potential using light at 660 nm is normalized with the amount of power, one would need, using light at 532 nm. Accordingly the corresponding scattering rate,

[7] The ringing effects (c.f. cha. 2.4) being present in coherent imaging systems are called "speckles".

using light at 660 nm, is normalized with the corresponding scattering rate for light with a wavelength of 532 nm.

Even though one needs less power for the same optical potential, the corresponding scattering rate increases dramatically by reducing the detuning. However, at 660 nm, a heating rate can be calculated by taking the scattering rate defined by eq. 2.9 giving $0.01\frac{1}{s}$ and multiplying it with the energy corresponding to a photon recoil

$$\frac{\text{energy}}{\text{second}} = \frac{\hbar^2 k^2}{2m}\Gamma_{\text{sc}}^2. \tag{3.6}$$

Inserting the the numbers results in an energy transfer of 740 Hz/s inside the wall (region of maximal intensity). Since the atoms are located away from the repulsive walls, the real energy transfer will be even less, such that it does not limit us.

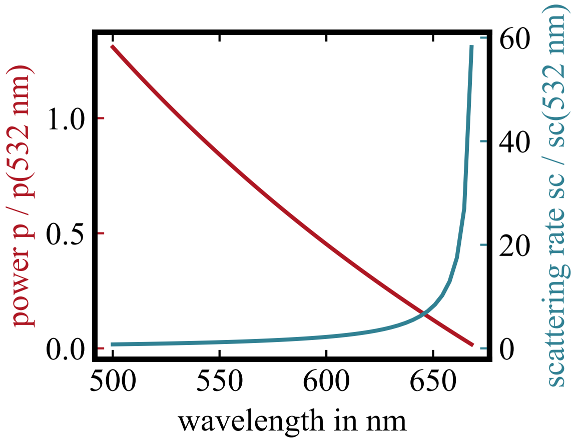

Figure 3.8 Laser power and scattering rate in dependence on the wavelength [14]. The needed power for a certain optical potential using light at the given wavelength is normalized with the needed power using light at 532 nm. The same is done for the corresponding scattering rate. It can be seen that small detunings reduce the amount of needed laserpower, while the scattering rate increases.

The laser system can be operated in three different modes, SKILL, FINE and the bare mode. The bare mode is the standard operation mode without any additional features. Operating in SKILL mode ("speckle killer"), the coherence length of the laser will be reduced by exciting of additional laser modes with voltage amplitude modulation. These modulations are performed at 200 MHz. The FINE ("Feedback Induced Noise Eraser") feature should reduce noise and power instabilities due to optical feedbacks in the setup. According to Toptica, the activation of these modes makes no difference for high output powers ($> 50\,$mW). Increasing the intensity, more laser modes are excited and additional voltage amplitude modulation do not lead to additional excitations.

For the planned setup it is important to characterize the coherence properties and the relative intensity noise of the laser to ensure that no parametric heating appears (c.f. cha. 2.1.4). The voltage amplitude modulation is not expected to create noise on relevant scales since 200 MHz is far above all trap frequencies used in our experiment lying in the kHz regime. Additionally, one has to estimate the required for power for the planned potentials to make sure that the laser is sufficient.

Power estimation For the desired box potential with a height of 15 kHz, side lengths of $50\,\mu$m, a wallthickness of $2\,\mu$m, a total power of 0.28 mW is required at 660 nm. The DMD has to be illuminated with much more power, because the beam emitted by the iBeam-SMART-660-S is Gaussian. Since the DMD is a binary mask, power gets discarded or reflected locally. To be as efficient as possible, the beamshape of the laser, illuminating the DMD has to be optimized. The intensity of a Gaussian beam is maximal in the center and decreases to the sides. Displaying a box on the DMD surface utilizes only a fraction of the incident light intensity and discards the remaining majority. By adding a beam expander before the DMD one can optimize the beamwaist of the illuminating laserbeam. Most efficient illumination with a Gaussian beam is given for a beamwaist equal to the sidelengths of the box on the DMD. In the optimized setup, a light utilization effenciency of 3.7 % can be achieved, leading to a total required power of 7.5 mW.

Relative intensity noise (RIN) Toptica provides a relative intensity noise measurement[8] (see fig. 3.10) but does not specify if there are substantial differences for the different operational modes. Since the coherence length reduction is achieved by exciting additional laser modes, one has to make sure that theses modes are driven in a way, that no additional relative intensity noise appears by e.g. competing laser modes at the laser threshold.

The relative intensity noise was measured using a ThorLabs photodiode[9]. The Photodiode was placed behind the fiber bringing the light from the laser board to the DMD. For a stable operation high frequency as well as low frequency noise is important and therefore intensity variations were measured for 2 s and $200\,\mu$s re-

[8] `https://www.toptica.com/products/single-mode-diode-lasers/ibeam-smart/`, called November 2020

[9] ThorLabs DET10A/M, $200 - 1100\,$nm, 1 ns rise time

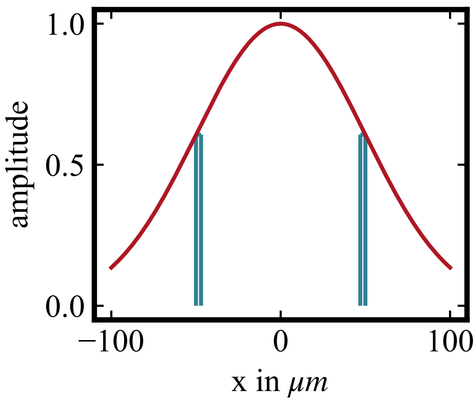

Figure 3.9 Creation of a box potential. The red beam shows the intensity profile of the laser and the blue lines show the required intensity for the walls. It can be seen that using a Gaussian beam is highly ineffective to produce a box potential. Therefore, the efficiency cannot be higher than 3.7 %.

spectively. As shown in fig. 3.11, the bare mode at low output powers provides additional noise up to 400 Hz. Using FINE or SKILL this noise is reduced. Increasing the output power, the additional noise floor in the bare mode decreases too, but keeps being above the noise corresponding to the SKILL and FINE mode. It is remarkable that for 50 mW at 2 kHz an edge is present in the spectrum. The RIN drops by 20 dBc/Hz. An edge is also present in the SKILL and FINE mode, but the decrease is less steep and it is lies at 1 kHz. At high output powers, all modes provide the same RIN, it is however enhanced in direct comparison with the Skill/Fine mode at medium output. The higher frequency RIN (fig. 3.12) is similar to the RIN provided by Toptica and is decreasing over the frequency spectrum from −100 dBc/Hz to below −175 dBc/Hz.

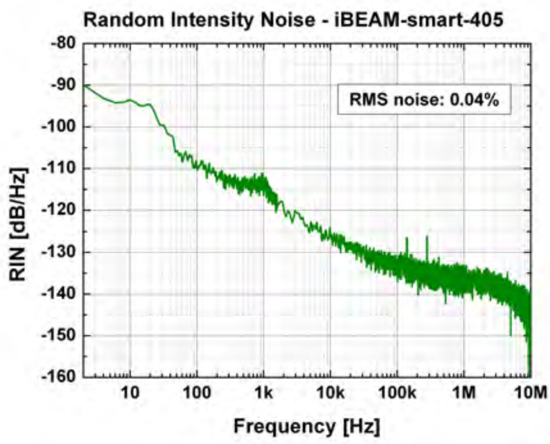

Figure 3.10 The random intensity noise spectrum from Toptica. Around the trap frequencies (kHz) the noise level is $-120\,\mathrm{dB/Hz}$.

At low frequencies, we find much larger RIN than specified by Toptica. This could be due to competing modes at the lasing threshold, since the number of active modes in the laser at bare mode operation increases for increasing output powers. If the bias voltage is close to the threshold voltage of a certain mode, the mode arises and breaks down leading to a an additional variation in intensity. Since many modes are driven by amplitude voltage modulation in the FINE or SKILL mode these intensity variations are washed out. Increasing the output power, more modes are active, even without usage of SKILL or FINE and so the effect on the RIN is less remarkable. Why the performance decreases further at high output powers is still an open question. One possible explanation is, that the active modulation is not present any more and so some modes are still close to their laser threshold leading to this additional RIN in comparison with an active amplitude modulation at medium output powers.

To conclude, the laser should not be used in the bare mode for low or medium output powers. Additionally, if the full power is not needed a medium output power with active SKILL or FINE mode is preferable.

Coherence length The intensity and the wavelength influence the depth of the optical potential created by the laser. The laserintensity is spatially modulated by the DMD and imaged onto the atoms in the main experimental chamber. As described in sec. 2.4, the coherence properties affect the spatial resolution and the imaging of sharp intensity features. As discussed previously, there are two kinds of coherence:

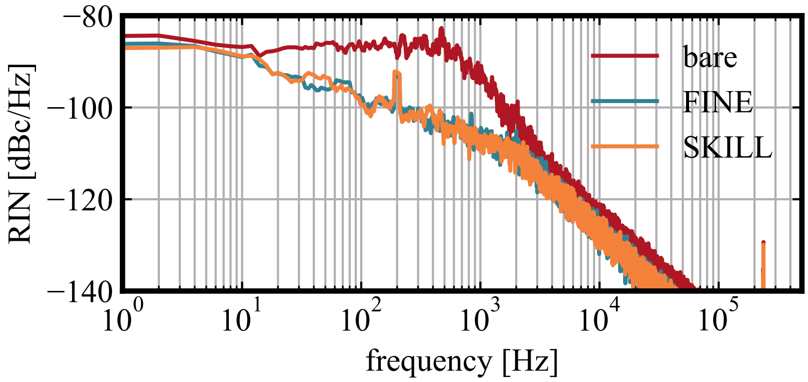

(a) 25 mW output power.

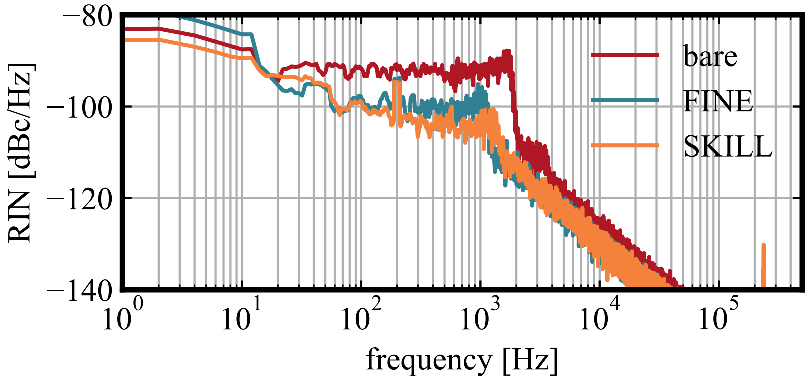

(b) 50 mW output power.

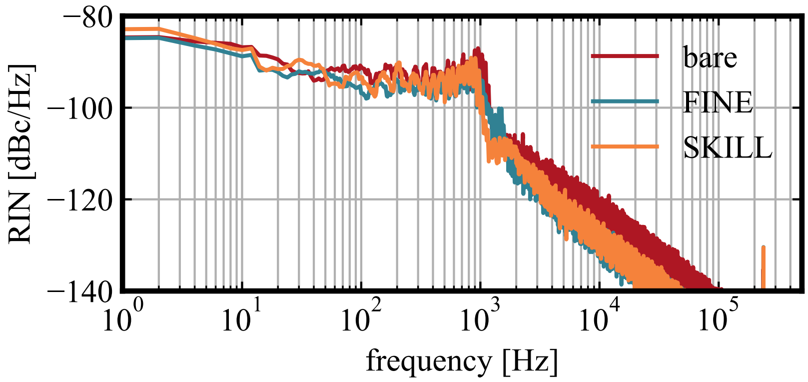

(c) 120 mW output power.

Figure 3.11 Relative intensity noise for different output powers of the three modes FINE, SKILL, bare.

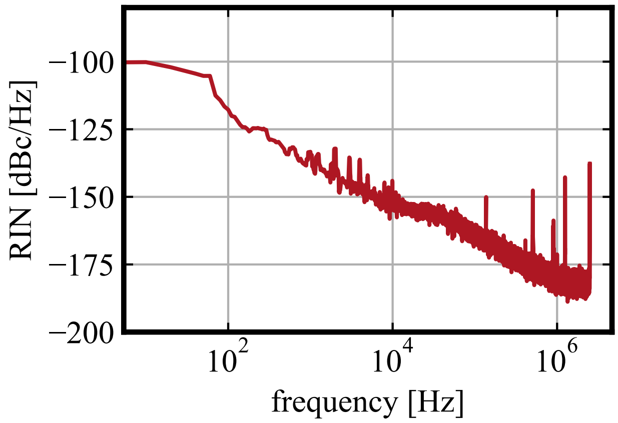

Figure 3.12 Noise spectrum of the laser for high output powers and SKILL mode active. The noise spectrum corresponds to the spectrum provided by Toptica (Figure. 3.10).

spatial and temporal. The specified and measured linewidth is on the order of 2 nm (fig. 3.13a), such that the laser emits partially temporal incoherent light with a coherence length on the order of 200 μm. By changing the operation temperature of the laser, the center wavelength changes by approximately 0.2 nm/K. This is not due to thermal expansion of the semiconductor medium (expansion coefficient of Si is 2.6 μm/K) but probably due to the temperature dependence of the bandgap (c.f. [37]) which lead to changes on the order of nm/K.

As already introduced in sec. 2.4, the treatment of partially incoherent light is difficult because the imaging properties depend on the correlation function at different object points. In this setup, the object points are the different micromirrors on the DMD. The correlation as a function of the distance between points, is not known in general and depends on the spectrum of the lightsource. To gain further insight in the spatial dependence of the correlation function, a Michelson interferometer was used. The path difference of the two arm was set by using an electronic translation stage. The mirror was steadily driven over a distance of 20 mm around the position giving equal path length. The time-amplitude trace was detected and translated into a path-difference-amplitude trace by multiplying with the stage speed of 400 $\frac{\mu\text{m}}{s}$. By moving the translation stage, the interference stripes on the photodiode move, which results in an oscillation in intensity. For the case where, the relative phases of the lightbeams coming from the two arms are well-defined, the interference contrast is maximal. If the relative phases are undefined, the contrast is zero

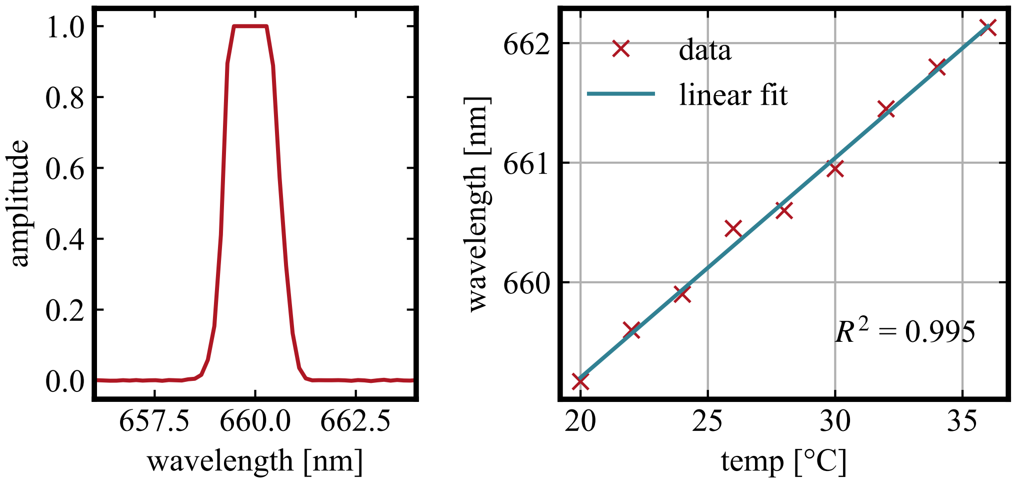

(a) The measured linewidth of the laser is around 2 nm, which corresponds to a coherence length on the order of 200 μm. It has to be noted that the used wavemeter has a resolution of 0.5 nm such that it gives no detailed insight over the form spectrum.

(b) Linewidth for different temperatures. The temperature dependence cannot be explained by the thermal expansion coeficient, that is on the order of μm/Km for semi-conductor materials. For a 5 cm cavity, this would lead to an expansion of 50 nm. Instead, the temperature dependence of the bandgap could lead to the observed effect ([37] ~ 0.5 nm/K).

Figure 3.13 Linewidth. The linewidth of the laser and its centerfrequncy depending on the temperature.

and no interference is observable anymore. Consequentially, when the coherence length is finite, the increase in path difference leads to a decrease in contrast until the interference stripes vanish. The path difference where the contrast is reduced $1/e$ of its maximum value, is identified as the coherence length. As already pointed out in sec. 2.4.3, revivals of the contrast at larger distances are expected. Light-sources like LEDs, halogen lamps or single mode lasers provide a spectrum with a center frequency which decays monotonically away from the center frequency. The iBeam-SMART-660-S in contrast, sends out multiple laser modes depending on the output power. Accordingly the dependence of the interference contrast of the path difference is more complicated.

To complement the RIN data, the traces for low output powers (25 mW) and high output powers (120 mW) are evaluated in the SKILL and bare mode. The taken intensity traces are given in fig. 3.14a - fig. 3.15b. The lower x-axis show the path difference of the two interferometer arms and the upper axis translates this path difference in a distance, measured in the number of micromirrors. The path difference is expressed in terms of micromirrors by calculating the path difference Δs picked up by the micromirrors originating from the finite angle of incidence.

The spectra show different behaviour for the two power regimes as well as for the two modes. In the low power regime, the bare mode shows an intensity trace with a global maximum at the white light position. The contrast decrease up to a path difference of 5 mm where the first revival starts. The coherence length is approximately 2.5 mm.

The trace at 25 mW and active SKILL mode differs a lot. Around the central peak, which widths is on the order of $200\,\mu$m, side peaks a tenth as high as the central peak, appear. After two millimeters no peaks are distinguishable from the background, being at a twentieth of maximal intensity. One finds first revivals at a distance of $5\,\text{mm} - 6\,\text{mm}$.

For higher output power the difference of the two modes is less striking. In the SKILL mode at 120 mW, the central peak is surrounded by two peaks with the same width (≈ 1 mm) and of half the amplitude. Between these main peaks the spectrum is filled with secondary peaks, such that there is no envelope dropping to zero and giving a coherence length. Nevertheless, at 5 mm path difference, the spectrum is repeated. Comparing this trace with the the bare mode, the main peaks are no longer distinguishable and the central maximum stands out of a diffuse decaying envelope. As before, the shape is repeated at a distance of 5 mm.

There is no clear envelope decaying to zero contrast in the spectra, because one sees a superposition of modes with long coherence lengths (probably $\sim$ m or $\sim$ km). We know that this laser emits at different frequencies at different output powers. Just a few modes are lasing for 25 mW output power, some are close to the lasing threshold, such that their emitted power differs over time as presented in fig. 3.11. One can interpret the bare mode trace at low output powers as an envelope, decaying due to the non-zero bandwidth, with a notable amount of noise due to the varying output power of modes close to the laser threshold. Driving the other modes by voltage amplitude modulation (SKILL mode) in a controlled way, could prevent that modes are driven close to their threshold and stabilize their respective output power. Therefore, the RIN at low frequencies is reduced with respect to the bare mode (fig. 3.11) and the interference contrast drops by an order of magnitude at a path differences of $200\,\mu$m.

For high output powers Toptica claims that enabling SKILL mode does not change much, because the laser is close to its maximal output power and many modes are already driven in the bare mode. Since the output power is already close to its maximum, additional controlled amplitude modulation might get impossible. This could be an explanation for the broader spectrum at high power compared to 25 mW.

All in all, the experimental requirements are best met if the coherence length is as short as possible and the incoherent regime is reached. Accordingly, the best performance is achieved if the laser is operated in the SKILL mode with low to medium output powers.

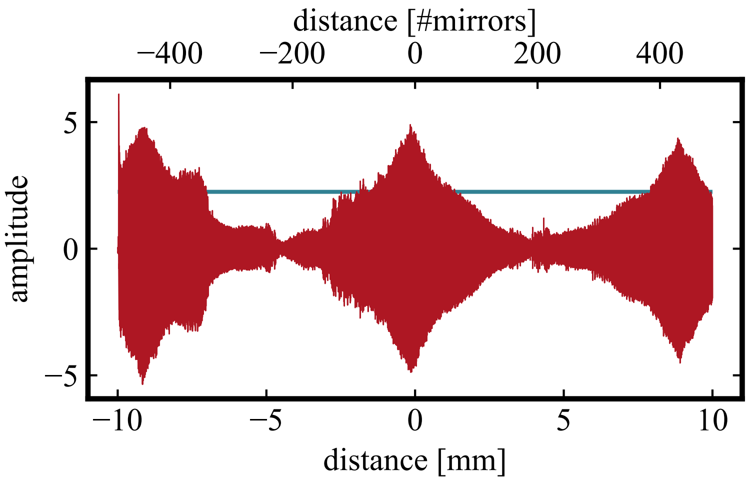

(a) Intensity trace for 25 mW bare mode.

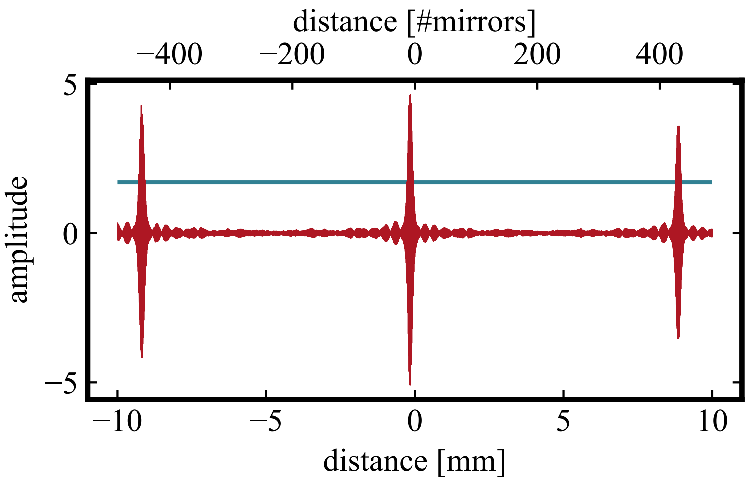

(b) Intensity trace for 25 mW SKILL mode.

Figure 3.14 Intensity for the different modes at low output power (25 mW). $1/e$ of the maximal intensity is marked by the blue horizontal line. The traces show a maximum at the white light position, corresponding to the case of no path difference. The contrast falls of by moving away from the wight light position. For low output powers, the bare mode contrast intersects the blue line at 3 mm. In the SKILL mode the central maximum is narrower and gives a coherence length of 200 μm.

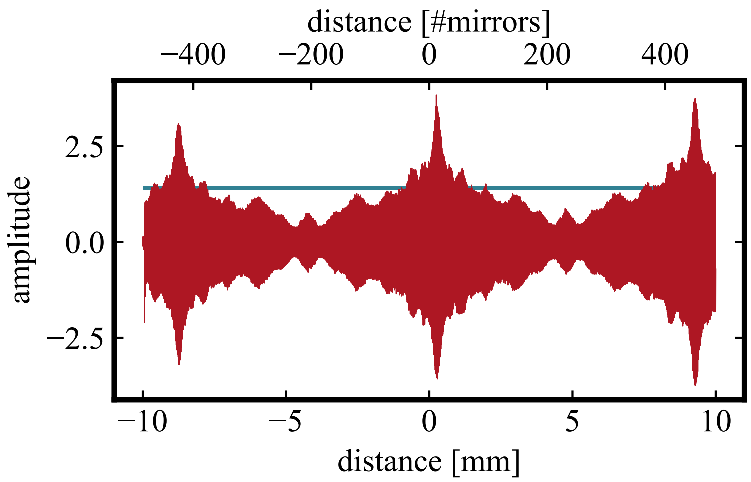

(a) Intensity trace for 120 mW bare mode.

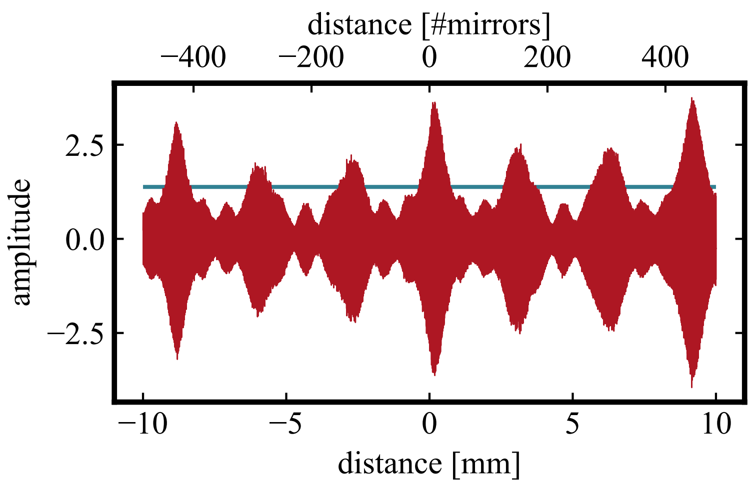

(b) Intensity trace for 120 mW SKILL mode.

Figure 3.15 Intensity for the different modes at high output power (120 mW). $1/e$ of the maximal intensity is marked by the blue horizontal line. The traces show a maximum at the white light position, corresponding to the case of no path difference. The contrast falls of by moving away from the position with equal path lengths. For high output powers, both traces show a broad central maximum, which is closely surrounded by other local maxima on the same scale, such that the definition of a coherence length is unclear.

Image quality With the characterization of the laser properties as a function of operational mode and output power at hand, it is now interesting to study their influence on the image quality. As shown in fig. 2.13b imaging with coherent light leads to ringing behaviour next to edges or sharp changes in intensity. That is especially relevant if dust and other pointlike imperfections are in the imaging path. They add mainly high spatial frequency components and intensity variations are present around them. In comparison, when the situation with incoherent imaging light is studied, these disturbances are suppressed. This is because the incoherent transfer function decreases monotonically with increasing spatial frequency and therefore these features are washed out in incoherent imaging systems. To visualize the difference, a pattern with all pixels in the "on" position is taken and camera images with the laser operated in the different modi are compared (fig. 3.17).

The image illuminated with coherent light, shows a stripe pattern. This could be due to some imperfections of the coverglass from the camera acting like a grating in the beampath. This pattern disappears as soon as the SKILL mode is activated. The difference between coherent and incoherent imaging becomes more apparent in a 1D cut of this image (fig. 3.16).

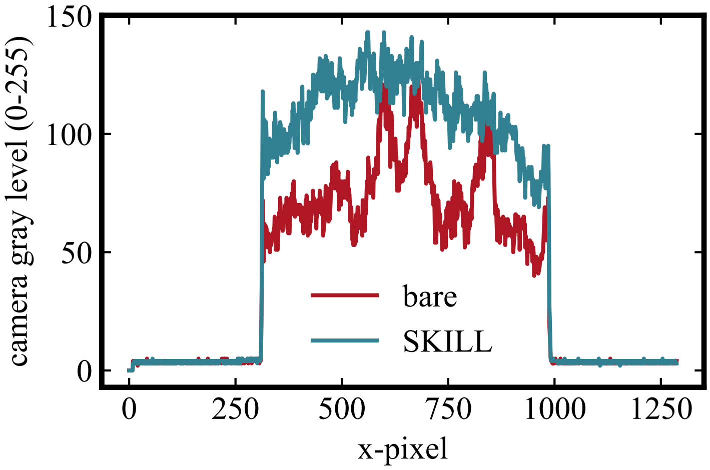

Figure 3.16 1D Cut of the image intensities in fig. 3.17. The intensity with "SKILL illumination" is smoother and has less disturbances than the intensity trace of the image corresponding to the bare mode.

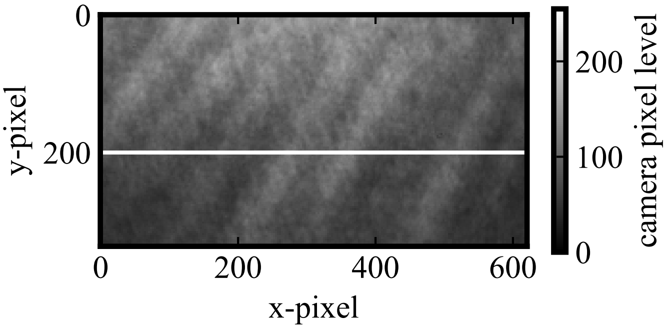

(a) Bare mode.

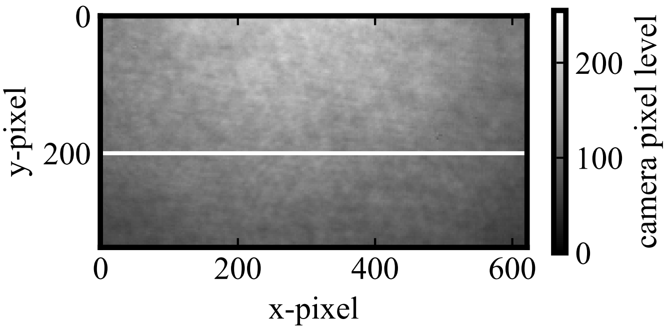

(b) SKILL mode.

Figure 3.17 Pattern with all pixels “on” at 10 mW laserpower in the SKILL and bare mode. In the bare mode a lot of disturbances due to dust are visible. An fringe pattern appears in addition, which could be explained by imperfections of the coverglass acting as a grating. After the activation of the SKILL mode, these imperfections disappear. The white line shows the position of the 1D cut shown in fig. 3.16

3.2.3 Blazing

A DMD as programmable micromirror array differs a lot from a conventional mirror. As explained in sec. 2.2 one can define a binary mask which is realized by switching the mirrors between two positions. If all mirrors are in the "on" position, the surface is not flat but consists of millions of tilted mirrors building a grating. The mirror size ($7.56\,\mu$m) is on the same order of magnitude as the laser wavelength (0.66μm). Illuminating this grating leads to a diffraction pattern in the far field. The geometrical situation is shown in fig. 3.18. The beams travel in a horizontal plane and the DMD is shown from above. The mirrors are tilted by θ_{tilt} and the beams come in with the angle θ_{in} with respect to the DMD normal. They get reflected under the angle θ_{out}. These two angles have different algebraic signs because they are defined with respect to the DMD normal. Two neighbouring mirrors are $d = 7.56\,\mu$m apart from each other. Beams getting reflected from different

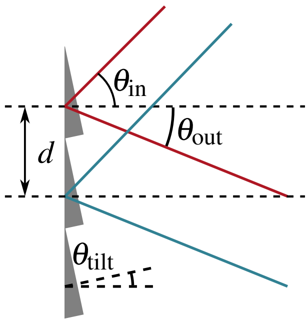

Figure 3.18 Blazed grating. All angles are defined with respect to the DMD normal. The mirrors are tilted by $\theta_{\text{tilt}} = \pm 12^\circ$. Beams with the input angle θ_{in} get reflected by neighboring mirrors under the angle θ_{out} and pick up a path difference of $d(\sin(\theta_{\text{in}}) + \sin(\theta_{\text{out}}))$ which depends on the distance of the reflecting mirrors.

mirrors pick up a path difference because each micromirror is tilted with respect to the DMD normal. This results in a diffraction pattern with many orders (see fig. 3.19) in the image plane. The zeroth order is the order with maximal intensity, such that we want to project this order onto our atoms[10]. The efficiency in this context is defined as the total power in the zeroth order compared with the total power of the beam, that falls onto the DMD. This efficiency depends strongly on the input angle (c.f. [38] or [39]). Since we want to avoid as many powerlosses as possible, the setup has to be optimized.

[10]The NA is too small to pick up more than one order.

Qualitatively one can understand the reflexion at the DMD surface by thinking about it in two different ways. On the one hand each single tilted mirror reflects the incoming light into the far field with the intensity maximum at $\theta_{\text{out}} = 24° - \theta_{\text{in}}$. On the other hand, an illuminated grating leads to interference maxima in the far field if $p(\sin(\theta_{\text{in}}) + \sin(\theta_{\text{out}})) = m\lambda$, m $\in \mathbb{Z}$. These two equations build the blazing condition.

Figure 3.19 Diffraction pattern of the DMD. Illuminating the DMD-surface leads to a diffraction pattern with many orders. The efficiency (0^{th}order power/total power) depends on the concrete choice of θ_{in} and θ_{out}.

The intensity pattern in the far field, depending on the in-and output angle can be calculated using Fourier-optics. As pointed out in sec. 2.3, the far field pattern is the optical Fourier transform of the incoming beam at the focal point. The grating will be treated as a transmissive one, which is illuminated from behind. The angles of the in-and outgoing beam relative to the DMD normal are imprinted in a phase gradient over the DMD surface. The reflection on a tilted mirror can be accounted for by setting $\theta_{\text{in}} + \theta_{\text{out}} = 24° = 2\theta_{\text{tilt}}$.

The transverse proportion of the wavenumber of the incoming beam is

$$q = \frac{2\pi}{\lambda}\sin(\theta_{\text{in}}). \tag{3.7}$$

Since the beams are propagating in a horizontal plane, and the tilt axis of the micromirrors is vertical, the 0^{th} order lies also in the horizontal plane and the grating can be described by the convolution of a dirac-train, accounting for the periodicity, and a box-function giving the micromirror size in 1D. The illumination angles θ_{in} and θ_{out} are imprinted in the phase gradient

$$\Delta = \frac{2\pi}{\lambda}\sin(\theta_{\text{in}} + \sin(\theta_{\text{out}})) \tag{3.8}$$

along the x-axis. p signifies the mirror pitch, which is $7.56\,\mu$m and N is the total number of micromirrors along the axis. The DMD is placed at the focal point before a lens and therefore the lightfield U_o at the focal point behind the lens is the Fourier transform of the lightfield U_i at the DMD. U_o can be written as

$$U_\mathrm{o}(k) = \mathscr{F}\left\{ e^{\mathrm{iqx}} \times \left(\sum_{m=-N/2}^{m=N/2} \delta(x-mp) * e^{i\Delta x} B(x,p) \right) \right\}. \tag{3.9}$$

Repeated application of the convolution theorem leads to the output amplitude $U_\mathrm{o}(k)$ as

$$U_\mathrm{o}(k) = \left[\mathrm{sinc}\left(\frac{Np}{2} k \right) * \sum_{m=-\infty}^{m=\infty} \delta\left((k-q) - m\frac{2\pi}{\lambda} \right) \right] \mathrm{sinc}\left(\frac{p(k-q-\Delta)}{2} \right). \tag{3.10}$$

U_o gets maximal if the dirac train lines up with the second sinc-term. Therefore, $k - q = m\frac{2\pi}{\lambda}$ and $k - q - \Delta = 0$ must hold. By plugging in the given definitions for Δ and q one finds the blazing condition

$$m\frac{2\pi}{\lambda} = \sin(\theta_\mathrm{in}) + \sin(\theta_\mathrm{out}) \quad \wedge \quad \theta_\mathrm{in} + \theta_\mathrm{out} = 24^\circ. \tag{3.11}$$

Since the DMD mirrors get titled along their diagonal axis, the DMD will be rotated by 45° to hold the beam parallel to the optical table. That also has to be accounted for in the blazing calculation. We treated it as a lattice with an adjusted mirror pitch $p' = \sqrt{2}p$. Inserting the numbers in the given formula one fulfills the blazing condition by choosing $(\theta_\mathrm{in}, \theta_\mathrm{out}) = (-16^\circ, 40^\circ))$. To verify the calculation, the intensity for different input-output angle configurations was measured[11] fulfilling $\theta_\mathrm{in} + \theta_\mathrm{out} = 24^\circ$. The measurement shows good agreement with the calculation and confirms blazing for $(-16^\circ, 40^\circ)$. For the blazing condition an efficiency of approximately 60 % could be reached. In the setup the output angle should be the smaller one (16°), to hold the DMD as aligned as possible to the subsequent optical components. If the DMD is tilted strongly and the longitudinal distance between mirrors gets too large, the image quality suffers from the finite depth of focus of the imaging system. The depth of focus is defined as twice the Rayleigh length

$$2z_0 = \frac{2\pi w_0^2}{\lambda}, \tag{3.12}$$

[11] One of the two angles is always negative, because all angles are defined with respect to the DMD normal.

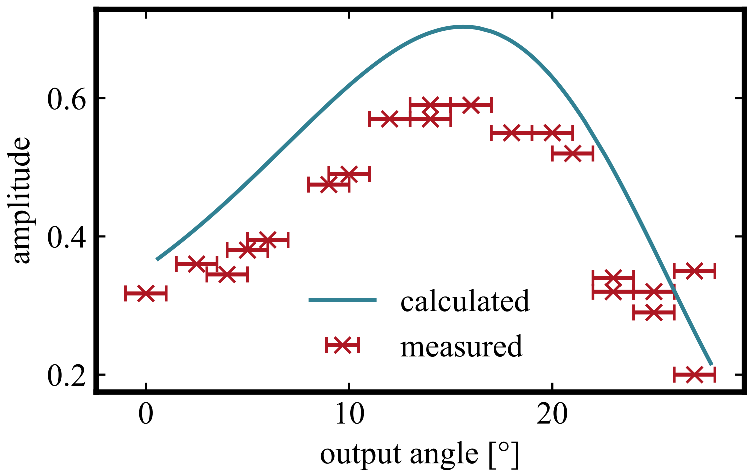

Figure 3.20 Lightpower in the 0^{th} order for different output angles. The DMD was illuminated under an angle $\theta_{\text{in}} = 24° - \theta_{\text{out}}$. The measurement shows good agreement with the calculation. The blazing condition is fulfilled for $(-16°, 40°)$

depending on the wavelength λ and the waist at the focal point w_0. Assuming a dynamical range of 49, i.e. $w_0 = 7/2$ pixels, the depth of focus is 6.7 mm. The tilt of the DMD leads to a maximal longitudinal distance of 2.8 mm between different mirrors, such that the image will not be relevantly affected by the finite depth of focus.

Additionally the grating has influence on the coherence properties of the light. As discussed in sec. 3.2.2, the laser has a certain bandwidth leading to temporal partial decoherence. The grating leads to output angles depending on the wavelength of the incoming beam (c.f. eq. (3.8) for $\Delta = m\lambda$, $m \in \mathbb{Z}$), such that the grating translates temporal decoherence into spatial decoherence.

3.2.4 Optical setup

Having evaluated all the single components, one can combine them for the optical setup, shown in fig. 3.21. The components will be placed on two different bread boards marked in gray, such that the laser and the DMD can be mounted independent from each other. The third breadboard is already in the setup and contains the EMCCD camera for fluorescence imaging. Additionally to the sketched components, a flipping mirror is mounted on the EMCCD-breadboard to couple in the light for absorption imaging, but since these components do not play role for the DMD setup, they are omitted.

The light for the optical potential building the box, is provided by the iBeam-SMART-660-S, emitting 660 nm light with a short coherence length (200 μm). The laser emits linearly polarized light such that a $\lambda/2$ plate is required to couple the light in the single mode fiber. The power will be stabilized using a fiber-based AOM. The light comes out of the fiber and with the tunable subsequent $\lambda/2$ plate and a PBS, the amount of power in the imaging path is tunable. After the PBS, the light polarization is cleaned. Afterwards a beamsapler is included to reflect a small amount of light onto the photodiode for regulating the AOM via a feed-back loop. The light illuminates the DMD, mounted in blazing configuration $((\theta_{\text{out}}, \theta_{\text{in}}) = (-16^\circ, \quad 40^\circ))$. The light gets diffracted by the DMD under an angle of 16° and enters the 4f setup. The first two lenses of 500 mm and 300 mm focal length provide a demagnification of 0.6 such that the DMD screen is demagnified to a size of 7.2 mmm $\times$ 11.4 mm. In the first image plane a combination of $\lambda/2$, PBS and a camera is placed to have access to the image in the first image plane. The beampath between the first image plane and the next lens is 1 m and the beam has to be folded multiple times. The distance between first image plane and the third lens is crucial because a dilatation would lead to blurring in the image. Therefore, a cat-eye (black box in fig. 3.21) is placed in between to be able to adjust the length of the beampath. The 1000 mm lens is followed up by two mirrors and a broadband polarizing beamsplitter to be able to couple the beam into the experiment. The s-polarized imaging beam coming from the objective gets reflected to the EMCCD camera and the light from the DMD goes through the cube towards the objective and the experimental chamber.

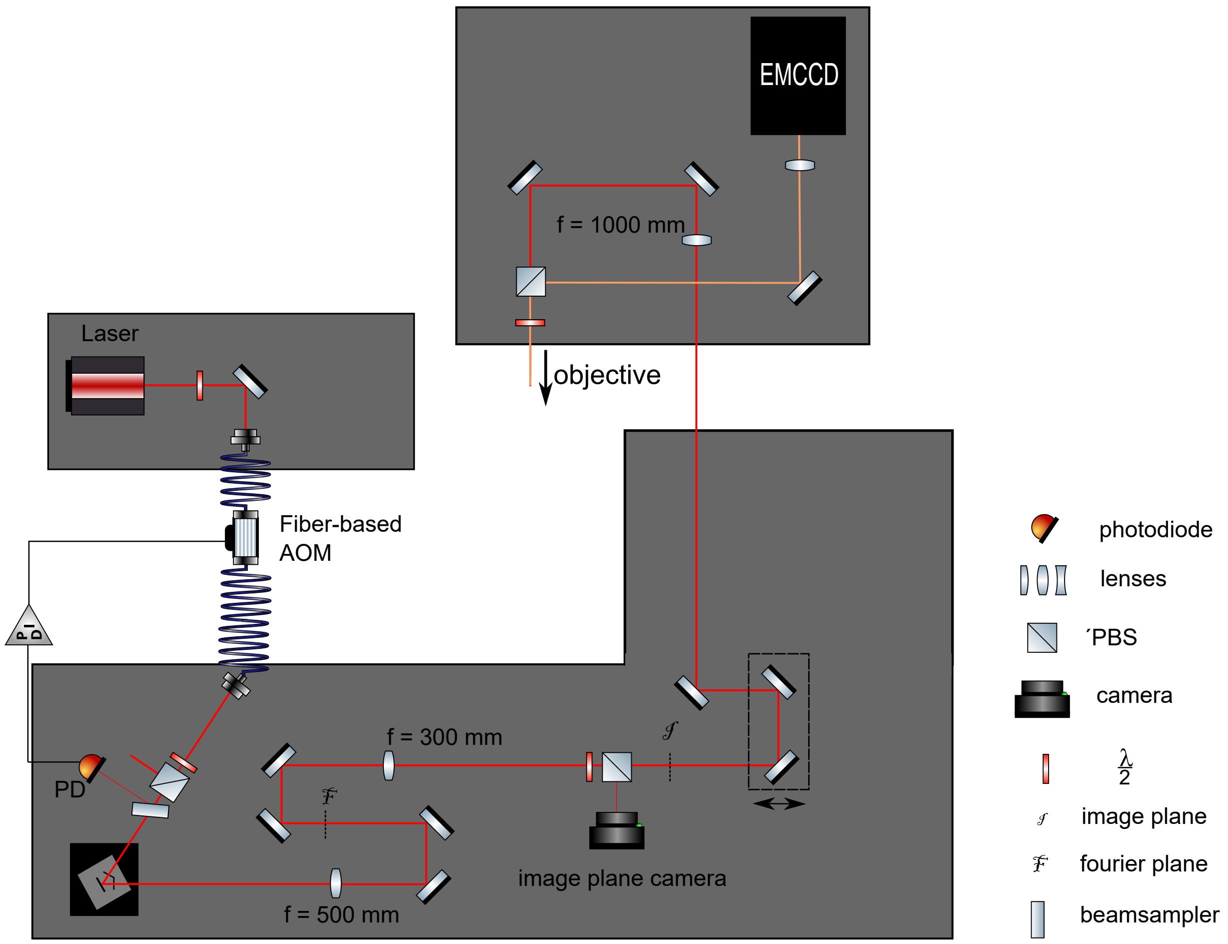

Figure 3.21 DMD Setup.

The vacuum architecture is shown in fig. 2.3. The imaging beam and the beam for the optical tweezer enter the experimental chamber from above ((3) in fig. 2.3). The imaging setup, which combines the tweezer beam, the imaging beam and the beam from the DMD is shown in fig. 2.7.

3.3 Using a DMD

Beamshaping can be done in two different ways. If the experimentalist just wants to display walls and limiting geometries, binary potentials being high or zero are enough. This would be the case for creating box potentials where the DMD is just used for spatial confinement. Therefore, one wants to make sure that the walls are as sharp as possible and that no potential oscillations close to the boundaries are present. Since no grayscaling is needed, one can choose the magnification without being limited by any dynamical range, one wants to achieve. That means, it has to be figured out, on which length and amplitude scales disturbances are and on what they depend, if they are present. Additionally one has to figure out if any image deformations occur in the optical setup and if it is possible to account for them. This will be explained in sec. 3.3.1.

Using the DMD for spatial confinement, while simultaneously altering the depth of the confinement, makes the situation more difficult, since the desired dynamical range sets an additional constraint for the optical system. As in the binary case, it is important to be aware of possible ringing effects close to boundaries and local amplitude variations. To achieve a target intensity in the atom plane, one has to account for the beamprofile and for the coherence properties of the laser. As discussed in sec. 3.2, a certain gray level can be achieved by adjusting the local density of pixels being in the “on” position, such that one has to figure out, how to binarize a grayscaled pattern without introducing spatial amplitude noise in the system. This will be presented in sec. 3.3.2.

To test these dependencies a test setup was used (fig. 3.22). The DMD is mounted on a prototype mount which did not fulfill the blazing condition. The beam comes out of a fiber, gets expanded to a beam diameter of approximately 1 inch and hits the DMD. There it is reflected and passes the first lens with a focal length of 500 mm. Behind the first lens, a beamsampler is included to reflect some light onto a photodiode for RIN measurements. The beamsampler is followed up by the second lens L2 with a focal length of $f = 200\,\mathrm{mm}$[12]. The light falls on a 50/50 beamsplitter which

[12] In the first test setup, I used a 200 mm lens instead of a 300 mm lens because I planned with a 800 mm lens before the objective. This one is replaced by a 1000 mm lens because the extra space is needed for optical components.

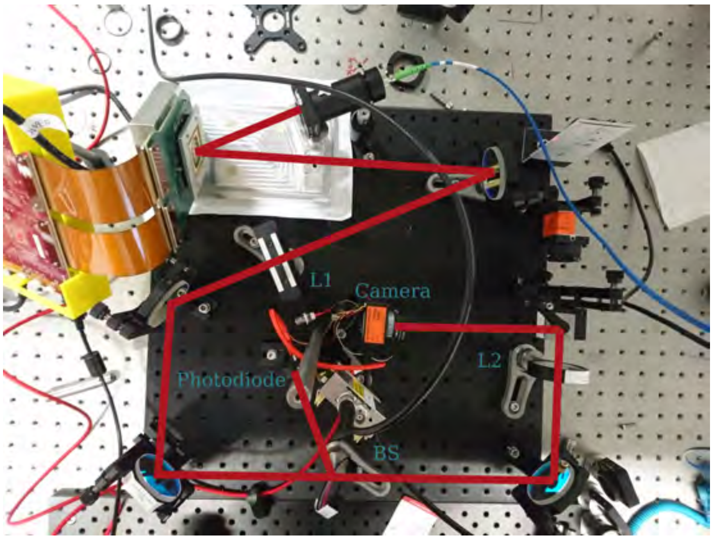

Figure 3.22 Test setup. The DMD is imaged on to camera using a 2f setup. The intensity modulations are measured using photodiode.

is followed up by the camera and a Shack-Hartman sensor. In this configuration one can see the image after the first telescope in the image plane.

3.3.1 Binary potentials

Image transform The propagation of the image to the first image plane is not trivial because the transfer depends on the relative pixel sizes of camera and DMD, on the magnification and on the relative position between DMD center and camera center. Additionally the image gets affected by imperfections of the optical setup. We assume that possible deformations can be described by shearing, translation and rotation and can therefore be modeled by an affine transformation

$$t\left((x,y)^T\right) = (b_1 + xa_{1,1} + ya_{1,2}, b_2 + xa_{2,1} + ya_{2,2})^T \tag{3.13}$$

acting on the point (x,y). The parameters a_i are rotation matrix entries and the parameters b_i describe the translational degrees of freedom. Therefore, the image data are compared with the camera data and the transformation is fitted by the affine transformation. One wants to account for the imperfections by acting the inverse image transform on the binary mask. Additionally the inverse transform is needed to do grayscaling. To achieve the desired intensity distribution in the atom plane, one has to account for the beamshape of the lightsource. By taking a camera image of a completely bright DMD-screen, one gets the intensity distribution after the first telescope (c.f. 3.22). By applying the inverse image transform on the camera image, one can propagate the distribution back onto the DMD. Therefore, one knows the initial illumination and can account for it by a proper grayscaled pattern.

It has to be noted that the following projections were done with a DLP3000 DMD with micromirrors in diamond pattern configuration (c.f. fig. 3.2). That is the reason for the additional distortion in horizontal direction. Nevertheless, even this deformation will be mapped by the image transformation.

For image processing `FindGeometricTransform[]` is used, which is a Mathematica function. By committing an input image and an output image to the function, the corresponding image transform is calculated. If the images are not equally sized, they get padded. The function fits an affine transformation to corresponding image points in the two images. Therefore, we take a gauge mask, which is loaded onto the DMD and compared with the corresponding image on the camera. The most reliable way to identify corresponding points in the images was to use asymmetric polygons as gauge masks and to detect their corners with the Mathematica function `ImageCorners[]` (c.f. fig. 3.23). The asymmetry makes it easy

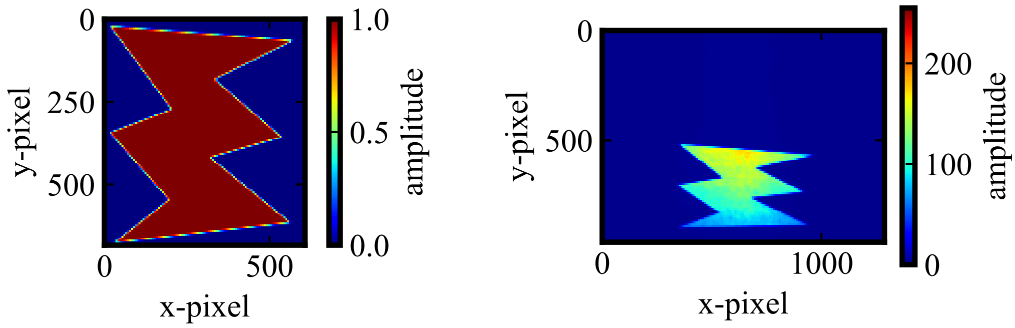

(a) DMD mask. **(b)** Camera Image.

Figure 3.23 A polygon is loaded onto the DMD. Due to the asymmetry it is easy to identify corresponding axis on the DMD and on the camera. Due to the diamond pattern geometry the image is distorted along one direction (c.f. fig. 3.2).

to identify corresponding axis on DMD and camera. The corners are committed to `FindGeometricTransform[]`, which returns the corresponding affine transformation. Since the camera image array has more entries than the DMD mask, the DMD mask is padded by Mathematica. To make sure about the position of the image in the padded matrix, it is required to define reference points. This is done by displaying a frame on the DMD, such that on sets all mirrors “off” besides the mirrors along the edges. This results in a camera image of the frame, which can be backpropagated by using the inverse image transform. Fig. 3.24 shows the camera

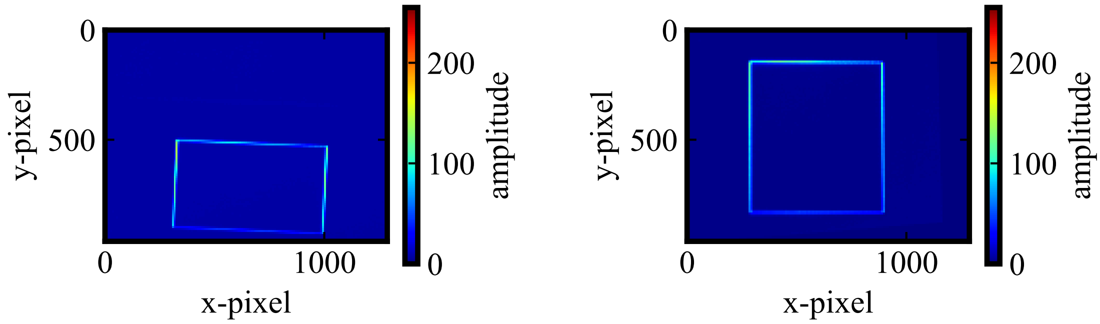

(a) Camera image of the frame. **(b)** Back-propagated camera Image.

Figure 3.24 A polygon is loaded onto the DMD. Due to the asymmetry it is easy to identify corresponding axis on the DMD and on the camera. Due to the diamond pattern geometry the image is distorted along one direction (c.f. fig. 3.24).

image of the frame (left) and the back propagated image (right). Even though the mask has less pixels than the used camera, after padding the backpropagated image has the same size as the camera image. Therefore, one has to use the propagated frame as a reference.

To benchmark the image transformation procedure, two steps were performed. Firstly we checked, if it is possible account for imperfections of the imaging system, by uploading the inverse image transform of the desired pattern on the DMD. Secondly a chess grid was uploaded on the DMD and the backpropagated image was analyzed to verify that no distortions are present.

The first target pattern is a white rectangle. The corresponding image points are the corners (marked in red in fig. 3.25). First the rectangle is uploaded onto the DMD (c.f. fig. 3.25a), the resulting image on the camera (3.25b) shows some shearing that is quantified by measuring the angles. A rectangle with all the four angles being 90° gets deformed and the angles on the camera are 92.38°, 87.35°, 91.75°, 87.98°. This is equivalent to a root mean square deviation from 90° of 4.45°.

Fitting the transformation of the edges and applying the inverse on the rectangle gives a tilted rectangle (shown in fig. 3.26 on the left). The corresponding camera image shows that the transformation equalizes the deformations of the imaging system (fig. 3.26 on the right). The angles are 90.09°, 89.86°, 90.08°, 90.3°, which gives a root mean square deviation from 90° of 0.35°. Concerning the geometrical form of the image, the processing could improve the image quality.

(a) Rectangle uploaded onto the DMD.

(b) Rectangle projected onto the camera.

Figure 3.25 A rectangle is uploaded onto the DMD and gets projected onto the camera. The resulting image shows some shearing which can be quantified by measuring the angles. The camera rectangle has angles of 92.38°, 87.35°, 91.75°, 87.98°.

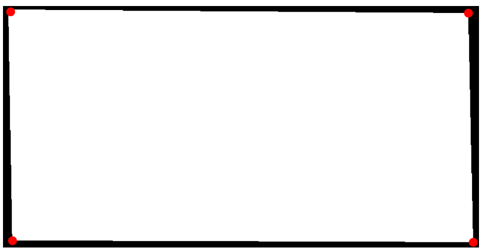

(a) Inverse transformed rectangle uploaded onto the DMD.

(b) Camera image of the inverse transformed retangle.

Figure 3.26 The edge coordinates from fig. 3.25 are used to fit an affine transformation the propagation of the image from DMD to camera. The target image (rectangle) gets inversely transformed to correct the imaging imperfection. Indeed, the rms error of the angles can be reduced by a factor of 12.

The second pattern that was uploaded is shown in fig. 3.27. The chess grid is deformed due to the diamond pattern configuration (see sec. 3.2) and by imaging imperfections. Nevertheless, the inverse transformation results in a transformed image which is geometrically similar to the uploaded grid. By using the function `Hough Line Transform`, implemented in python, one can detect lines and read out angles. The angles of the horizontal lines were found to be on average -0.25° with a standard deviation of -0.11° and the angles of the vertical lines were found to be on average 90.27° with a standard deviation of -0.14°. Therefore, acting the inverse image transformation on the camera image, gives an image, which is geometrically similar to the uploaded mask. That means that the image transform maps the present image deformations well.

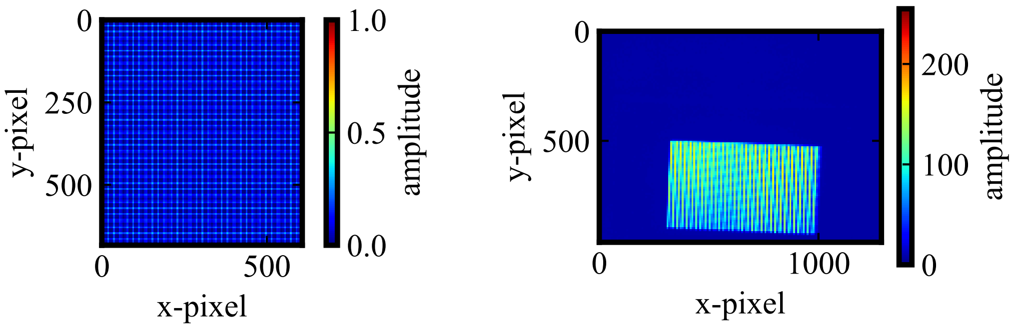

(a) DMD mask. **(b)** Camera Image.

Figure 3.27 Uploading a chess grid onto the DMD leads to strongly distorted chess grid on the camera screen.

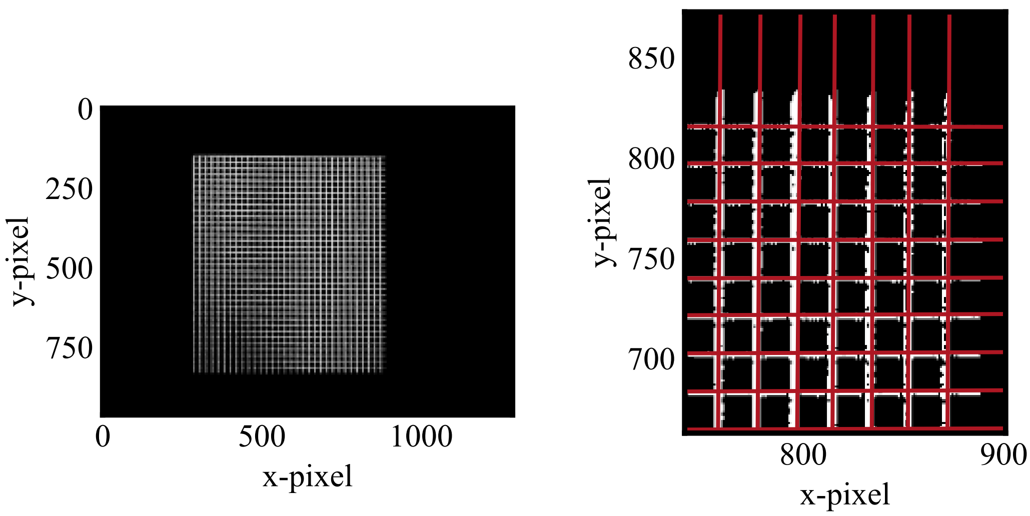

(a) Back propagated chess grid.

(b) Angle measurement in the back propagated image.

Figure 3.28 The image transforms maps the image deformations well. This is verified by the fact, that acting the inverse transform onto the camera image produces an image which is geometrically similar to the uploaded mask.

Ringing To quantify ringing effects, the setup in fig. 3.22 is used but instead of the beamsampler an Iris is placed in the Fourier plane. A striped pattern is uploaded onto the DMD (fig. 3.29) and the intensity variations next to the edge on the bright side and the dark side are examined. The influence of the numerical aperture is tested by closing the Iris. Fig. 3.30 shows the image and its simulation for differ-

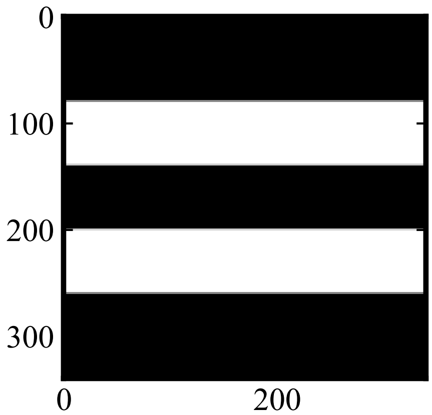

Figure 3.29 Binary mask dislpayed on the DMD to investigate the ringing next to edges.

ent NAs[13]. Since the amplitude variations on the dark and the bright side are on different scales, the respective scales are adjusted.

Spatial variations of the intensity perpendicular to the edges are present. The wavelengths of the oscillations in the simulated data for NAs of 0.025, 0.017 and 0.008 are approximately 7 pixels, 10 pixels and 21 pixels, while the measured wavelengths are 3 pixels, 4 pixels and 10 pixels respectively. Due to the finite NA of the system, some Fourier components are filtered out. The cutoff-frequency in an imaging system with a binary filter in the image plane is proportional to $(2\pi/\lambda) \times NA$ and therefore a decrease of the observed wavelength for a decreasing numerical aperture is reasonable.

The lengthscale of the variations, being approximately 10 camera pixels in the first image plane, would correspond to $10 \times 3.75\,\mu\text{m} \times (1/50) = 0.75\,\mu\text{m}$ in the atom plane, such that these variations are only present close to the boundaries. The lengthscale of the variations on the dark side is similar (c.f. fig. 3.31).

The amplitudes of the variations do not depend on the NA. In the simulations they oscillate about up to $\pm 20\,\%$ around the medium value on the bright side. In the

[13] The simulation procedure is the same as in sec. 2.4.2.

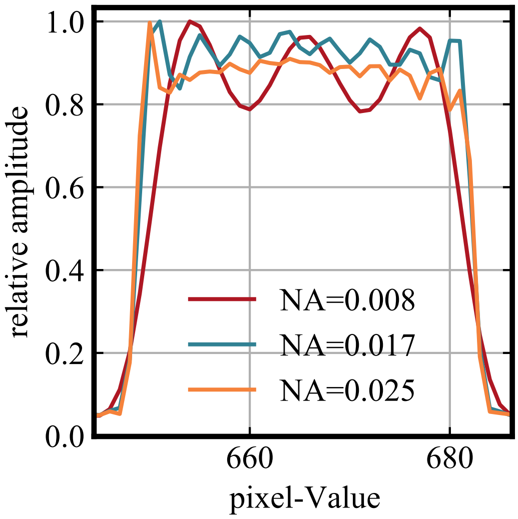

(a) Camera Image.

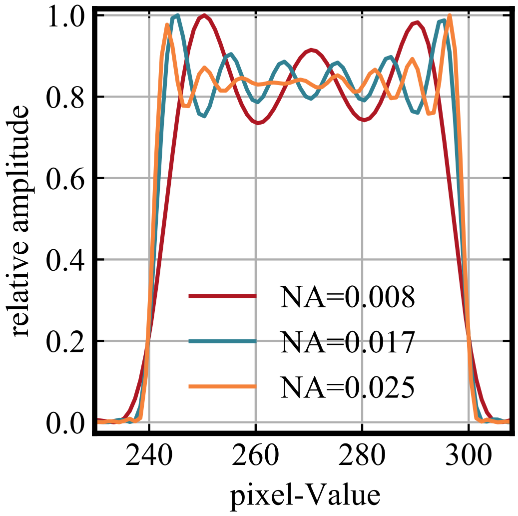

(b) Simulation

Figure 3.30 The simulated and the camera image of fig. 3.29 for NAs of 0.025, 0.017 and 0.008. The 2D pattern was simulated. From the corresponding image, the amplitudes along the horizontal axis were added and plotted along the vertical direction. The oscillations lie on a length scale of 7, 10 and 21 pixels (simulation) and 3, 4 and 10 pixels (camera) with a relative amplitude of 20 % to 30 %. Increasing the NA reduces the frequency of the oscillation.

measurements, oscillations with a similar relative amplitude (20 % to 30 %) were observed. In the dark region, the variations are smaller in amplitude (c.f. 3.31). The first and second maximum are at 1 % and 0.3 % of the wall height and with increasing distance to the edge, the variations disappear. Having two walls close to each other leads to an enhancement of the variations between the walls, since these modulations overlap. Nevertheless, the resulting relative intensity noise for the chosen numerical apertures is still maximally on the order of 1 % of the wall height (c.f. fig. 3.31) and limited to a region of about ten camera pixels around the edge. Assuming the given demagnification of 80, this corresponds to approximately 0.75μm in the atom plane. Since the wall height of the target system is 15 kHz, a potential difference of 1 % would correspond to an energy variation on the order of 150 Hz.

In contrast to the simulation of the coherent imaging process, the incoherent output shows no ringing effects (fig. 3.32). By comparing the camera images with the images from the simulations, one finds that the setup is better described by the coherent imaging simulation.

The variations of the intensity in the bright regions are not crucial for our setup, as we work with blue detuned beams. Therefore, the potentials are repulsive and do not contain any atoms. Hence, only the variations in the darker regions have to be considered.

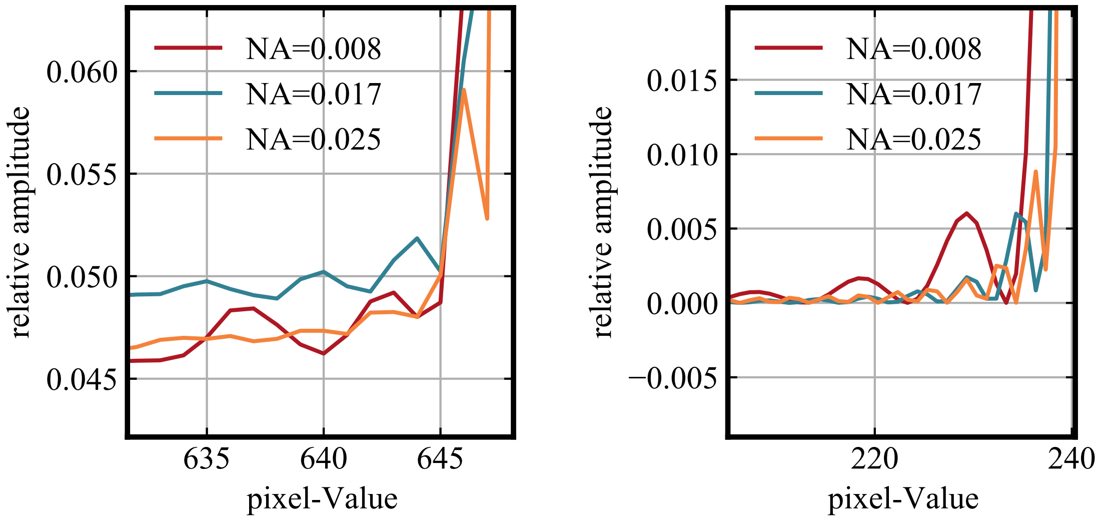

(a) Camera Image

(b) Simulation

Figure 3.31 Intensity variations on the dark side of the edge between the two stripes. The lengthscale is similar to the lengthscale in the bright region but the amplitudes are much lower being on the order of 1 % of the wall height.

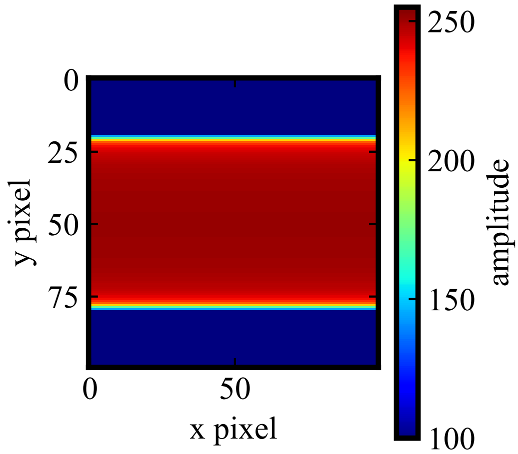

(a) Incoherent illumination for a NA of 0.025.

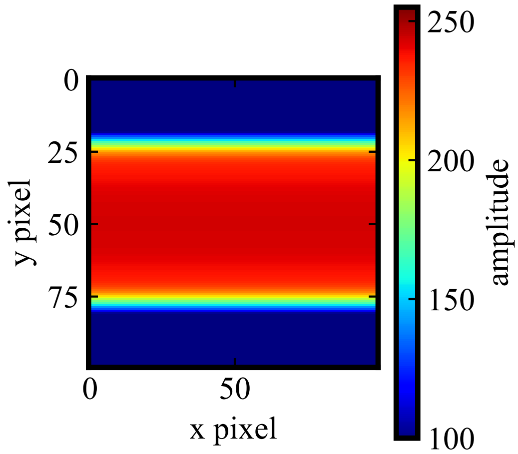

(b) Incoherent illumination for a NA of 0.008.

Figure 3.32 Incoherent illumination with numerical apertures of $NA = 0.008$ and $NA = 0.025$. It can be seen that no ringing is present in the system which does not correspond to the observed intensities.

3.3.2 Grayscaling

Although the DMD is a binary amplitude mask, it is possible, as explained in sec. 3.2.1, to create potentials with grayscaled amplitudes. This can be useful for excitations in sharp geometries, being on a lower energy scale than the confining potential, for example excitations of sound modes in box systems, or excitations of vortices in atomic traps as in [40], [41] and [42]. Since our lightsource emits a Gaussian beam, we want to be able to account for the Gaussian curvature of the intensity to build arbitrary potential landscapes. Therefore a first step will be to try to find a DMD mask that results in a constant intensity distribution in the image plane and based on this to create "physical" grayscaled images, being an harmonic trap and a user defined Gaussian intensity distribution.

dithering To control the local intensity in the atomplane with the DMD, the perfect image of a micromirror has to be smaller than the Point-Spread-Function of the optical system such that each PSF is illuminated by several micromirrors. By propagating the PSF spot in the atom plane back onto the DMD, one gets the micromirrors illuminating the corresponding spot in the atom plane. Therefore the local image plane intensity is controlled by the local amount of bright pixels on the DMD. The translation of an image containing multiple intensity levels between 0 and 1 into a binary mask is called dithering. The most common application of dithering is, to reduce the size of image files by reducing the number of image pixels. If the image is large, the effect on the image quality is negligible because the human eye can hardly recognize the difference due to its finite resolution. We want to use the same technique to grayscale our potentials by using the finite resolution of the imaging setup.

The first intuitive idea is to translate the intensity level of an image pixel into a probability for the corresponding micromirror to be in the "on-position". Therefore, the setting of a mirror just depends on the local intensity level and not on the values of surrounding pixels. That results in an image with many sharp features (c.f. 3.34c) and coarse grained areas. This is, because the quantization error is not accounted for. In every binarization process a quantization error arises which leads to spatial noise in the resulting image. State of the art dithering procedures, c.f. [43] and [44], consider the quantization error and try to spread it over neighboring pixels by reading through the image from top to bottom and from left to right. Compared to the intuitive ansatz, this needs more calculation time, since the setting of a single mirror depends on the corresponding pixel and on the quantization error of preceding operations. By increasing the number of neighboring pixels to be concerned, one diffuses the error further but the calculation time increases. That means, one has to make a trade-off between error-diffusion and calculation time and therefore, as in other cold atom experiments, e.g. [45], the original Floyd-Steinberg procedure (sec. 5.3) is chosen. Diffusing the errors means to shift noise in the spatial frequency spectrum to higher frequencies. In fig. 3.34 the effect is shown. In the top row, the Fourier transforms of the local dithered and error diffused parrots picture are shown. In the local dithered spectrum, the noise is present at all spatial frequency components, and low amplitude details are lost. That is not the case for the error diffused image as also reported in [46]. The spatial quantization noise is shifted to regions of higher spatial frequency. That leads to an image of higher quality since the the imaging system has a finite numerical aperture, such that high frequency components are not concerned and spatial noise in the error diffused image is filtered out.

Since, using the Floyd Steinberg algorithm, one reads through the image from top to bottom and from left to right, periodic structures appear in the image (c.f. 3.33b). This is not the case for the first ansatz, explained above, since no correlations between neighboring pixels exist. Periodic structures lead to bright distinct peaks in the Fourier plane, which makes the image vulnerable to imperfections in the beampath, since a local disturbance can affect the whole image. That is why, one adds a random, normal distributed weight to each single pixel, such that the correlation between neighboring pixels is decreased and the image gets spread further in Fourier space. The standard deviation of the distribution is chosen to be 0.3, which turned out to be a good compromise between a properly dithered image and a an adequate spread in Fourier space. As it can be seen in fig. 3.33d, periodic structures are suppressed.

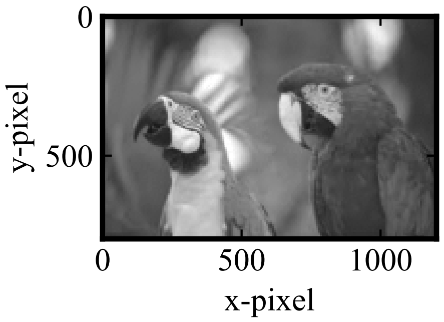

(a) Floyd Steinberg no random noise.

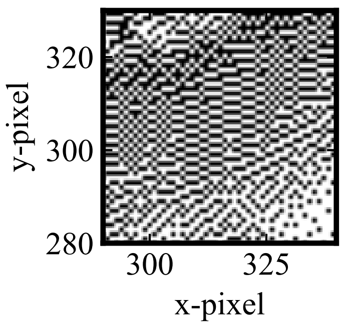

(b) Periodic structures appear.

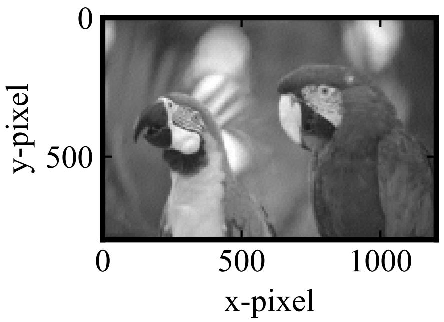

(c) Floyd Steinberg with normal distributed random noise.

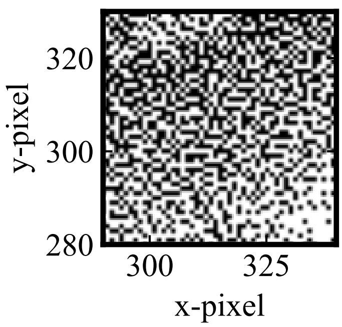

(d) Periodic structures are suppressed.

Figure 3.33 Floyd Steinberg dithering. The right column zooms into the corresponding image. Floyd Steinberg dithering (first row) leads to periodic structures which can be suppressed by adding random noise (second row).

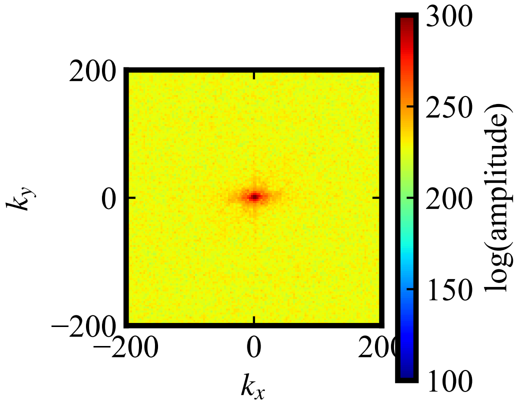

(a) Probabalistic dithering, Fourier spectrum. A noisefloor at all spatial frequencies is present.

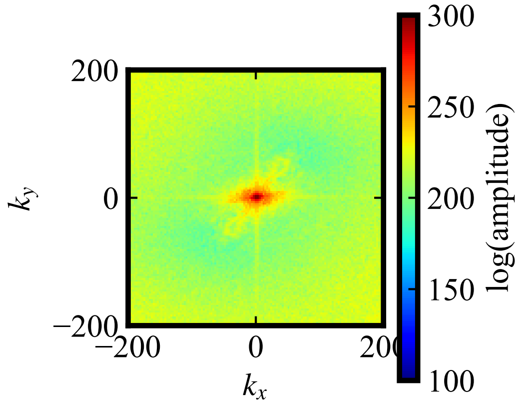

(b) Floyd Steinberg dithering, Fourier spectrum. Spatial noise is mainly present at high spatial frequencies.

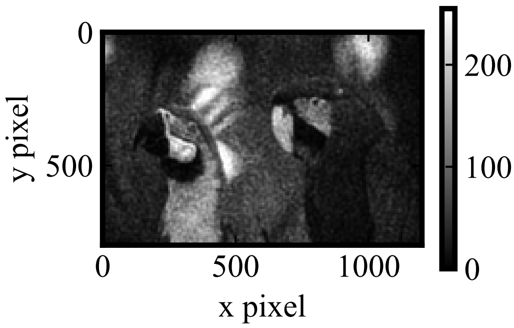

(c) Probabilistic dithering. The probability to be white is graylevel/255 for each single pixel.

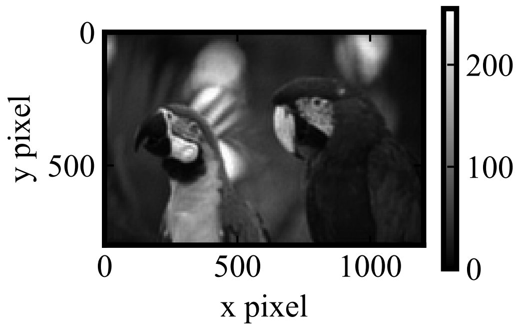

(d) Floyd Steinberg dithering. The quantization error is diffused over neighbouring pixels.

Figure 3.34 Floyd Steinberg dithering (right) and probabilistic dithering (left). Probabilistic dithering sets the probability of each pixel to be white independently of the neighboring pixels. That leads to an overall noisefloor in the Fourier spectrum. Floyd Steinberg algorithms diffuse the quantization error to neighbouring pixel and the noise is shifted to higher spatial frequencies.

Intensity scaling Using the Floyd Steinberg algorithm, it is possible to translate an image, consisting of different intensity levels, into a binary mask. The finite resolution of the imaging system leads to a smooth grayscaled intensity distribution in the atomplane. Nevertheless it has to be examined how the number of bright mirrors on the binary mask scale with the intensity level in the atom plane.

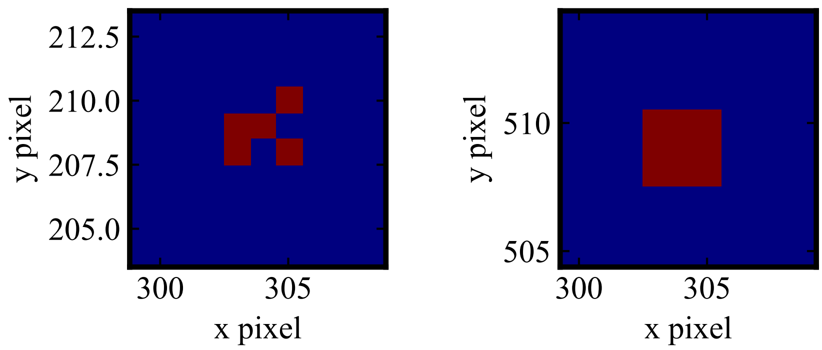

(a) 5 bright pixels. **(b)** 9 bright pixels.

Figure 3.35 Grayscaling. The image plane amplitude is controlled by the local number of bright pixels (red) on the DMD. Since the resolution is 10 pixels, the imaging system is not able to resolve the local structure and the number of bright pixels does not affect the form of the spot in the imageplane but its intensity.

In fig. 3.35 an imaging system with a resolution of 10 image pixels is assumed. The local intensity at two different spots in the atom plane is controlled by two 3×3 pixel arrays. These arrays cannot be resolved anymore and therefore grayscaling is possible. The left array consists of five bright pixels, while the right array consists of 9. Comparing the corresponding image plane intensities, shows that the peaks in the coherent system scale as $5^2 : 9^2 = 25 : 81 = 0.31 : 1$, while the incoherent imaging system shows a scaling of $5 : 9 = 0.56 : 1$.

As pointed out in sec. 2.3, in the coherent case, the field **amplitude** in the image depends linearly on the input **amplitude**. For incoherent imaging, this is not the case, since the **intensity** of the output field is linear in the **intensity** of the input field. Therefore, doubling the number of bright mirrors for coherent illumination increases the image plane intensity by a factor of four, while the same procedure for incoherent light would double the image plane intensity. This effect is illustrated in fig. 3.36.

The lightsource planned for the setup (c.f. sec. 3.2.2) is neither perfectly coherent

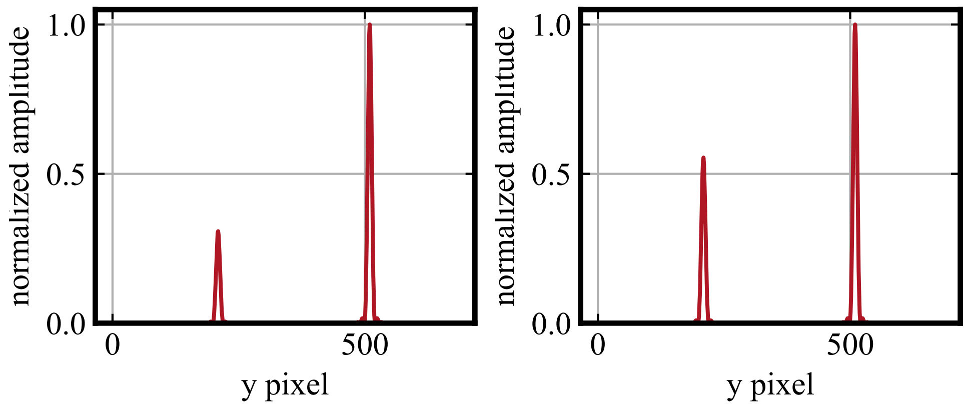

(a) Coherent illumination of the structure in fig. 3.35. The peak heights are 1 and 0.31.

(b) Incoherent illumination of the structure in fig. 3.35. The peak heights are 1 and 0.56.

Figure 3.36 The scaling of the imageplane intensity with the number of bright DMD-pixels depends on the illumination. For coherent light, the amplitude scales quadratically with the number of bright pixels and for incoherent illumination the scaling is linear.

nor perfectly incoherent. To check the dependency between the number of bright pixels and the intensity level in the image plane, monochrome graylevel patterns were uploaded onto the DMD. In fig. 3.37, the ratio of on to off pixels is compared with the corresponding relative image intensities. For coherent illumination, one would expect a quadratic scaling, while incoherent illumination would lead to linear scaling. Our used lightsource lies in between these two limits. A quantitative description of the intensity scaling is difficult, because it depends on the spatial dependency of the coherence function, as pointed out in eq. (2.18).

The image formation process depends strongly on the coherence properties of the light, being reflected by different mirrors. The coherence contrast for different delays between the beampaths is shown in fig. 3.14a to fig. 3.15b. The interference contrast depends on the path difference/time delay between two different beams. Since the input and output angles are fixed, the path difference between beams, being reflected by two mirrors being *#mirrors* apart from each other can be expressed as

$$\#mirrors = \frac{\Delta x[\mathrm{mm}]}{7.56\,\mu\mathrm{m} \times (\sin(\theta_{\mathrm{in}}) + \sin(\theta_{\mathrm{out}}))}. \tag{3.14}$$

A quantitative description of this imaging process is very complicated since the patterns on the DMD have a size of several hundred micromirrors and the interference contrast is strongly spatially dependent on this lengthscale and two different kinds of coherence are mixed up. On the one hand there is the temporal incoherence of the lightsource due to the bandwidth. On the other hand, the blazed grating leads to output angles depending on the wavelength of the incoming beam. Therefore, the blazed grating translates temporal decoherence into spatial decoherence.

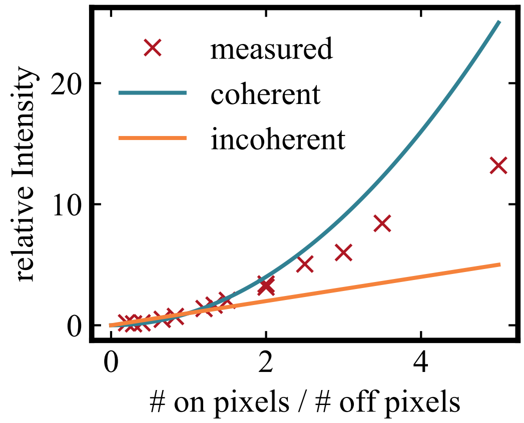

Figure 3.37 The relative amount of bright pixels is compared with the relative intensity in the image plane. The expected scalings for coherent (quadratic) and incoherent (linear) illuminations are shown. The measured scaling lies between these two limits.

Flat Potentials Knowing the transformation function of the imaging system enables the experimentalist to account for deformations and to map the camera image onto the DMD. For the creation of grayscaled potentials, a mapping is needed to account for the intensity distribution $I_{\text{in}}(x,y)$ of the illuminating beam. Depending on the coherence properties of the light, the DMD is either a binary amplitude or a binary intensity mask. In a coherent picture, the output amplitude $\sqrt{I_{\text{out}}}$ can be described as

$$\sqrt{I_{\text{out}}} = \sqrt{I_{\text{in}}} \times mask(x,y), \tag{3.15}$$

where $mask(x,y)$ describes the DMD mask and is locally either one or zero.

To benchmark the system, one tries to project a flat potential in the image plane by equalizing the Gaussian intensity distribution of the incoming beam. For grayscaling, coherent imaging is assumed, since this led to a better performance in terms of intensity scaling.

In the following, images were taken with the setup from fig. 3.22 with an iris in place of the beamsampler (BS). By closing the iris, one can decrease the numerical aperture and increase the dynamical range. The iris was closed to a diameter of 7.7 mm, which corresponds to a NA of 0.015. With the given magnification 5/3 this leads to a dynamical range of 36[14].

The workflow is shown in fig. 3.38. First, the image transformation function is determined as described in sec. 3.3.1. Subsequently one sets all DMD-mirrors "on" and takes a camera image to measure the beamshape in the image plane (a). One fits the intensity distribution with a Gaussian function[15] (b) and act the inverse image transform on it. One gets the backpropagated beam (c), which shows the intensity distribution at the DMD surface in the coordinates of the DMD. Since the transformation function maps between equally sized matrices, one needs a frame of reference to identify the screen in the image. That is why, an image of a pattern is taken, where all mirrors are "off", besides the mirrors at the edges. Backpropagating the corresponding camera image gives a frame of reference (d), which can be used to cut the relevant region out of the backpropagated beam.

Knowing the intensity distribution of the lightsource at the DMD (I_{DMD}) surface, one can identify the amplitude as $\sqrt{I_{\mathrm{DMD}}}$. The needed reflection of the DMD pattern is calculated as

$$\mathrm{reflection}(x,y) = \sqrt{\frac{\mathrm{target(x,y)}}{I_{\mathrm{DMD}}}}. \tag{3.16}$$

If the target potential is flat, target(x,y) is a matrix, where all entries are equal. Therefore, the local reflection is a value between zero and one. This factor has to be scaled properly, depending on the format that is used for the Floyd-Steinberg-Algorithm. Since we use 8 bit images (monochrome) the reflection gets scaled by 255. The resulting 8 bit image is binarized by using the Floyd-Steinberg-Algorithm (e).

Since the reflection is limited to one, the local amplitude level in the atom plane is always limited by the local amplitude of the lightsource. Therefore, for a given target grayscalelevel, the size of the flat region is limited. This can be seen in fig. 3.38 (e) and (f). Due to the high target intensity, eq. 3.16 gives a reflectivity larger than one in the lower left and lower right corner. Therefore, the calculated local amplitude ($\sqrt{I_{\mathrm{loc}}}$), which is given by the reflectivity scaled with 255, is larger than

[14] As described by eq. (3.5). In the final setup a dynamical range of 49 is planned.

[15] After several runs in turned out, that the image transformation works more reliable if one propagates the fitted intensity distribution back onto the DMD instead of using the camera image

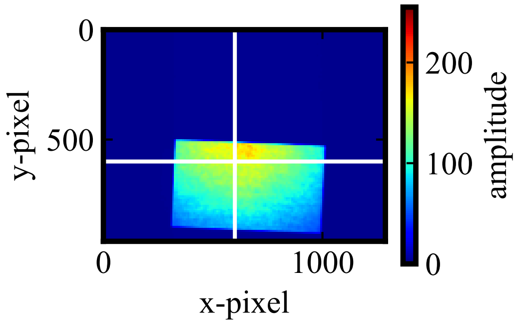

(a) Camera Image, bright screen. The white lines show the axis for the horizontal cut in fig. 3.39

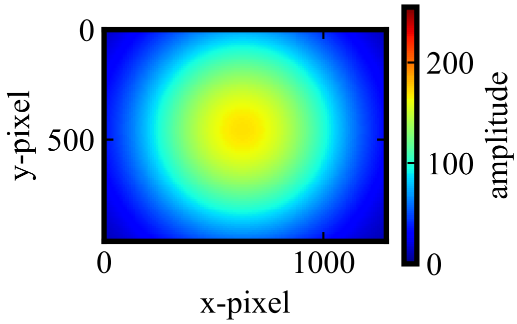

(b) Gaussian fit of the intenisity distribution on the camera

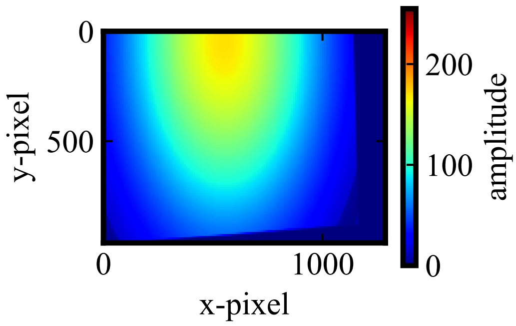

(c) Backpropagated beam.

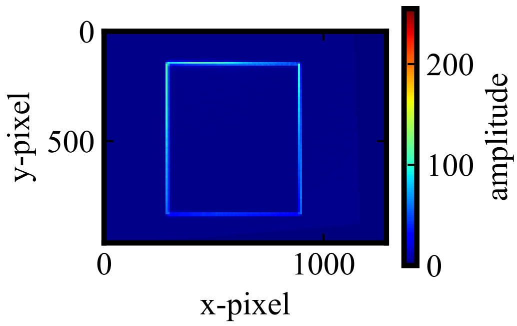

(d) Backpropagated Frame for reference.

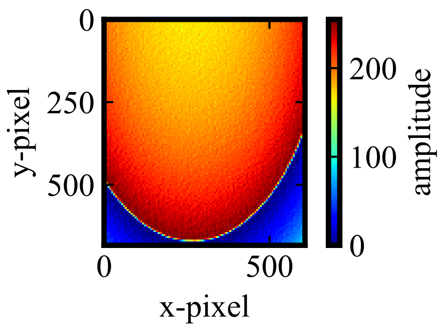

(e) Binary Mask displayed on the DMD after Floyd-Steinberg dithering. Due to the colorscheme, it seems that the mask in non-binary but this is due to the high pixel density for the given picture size.

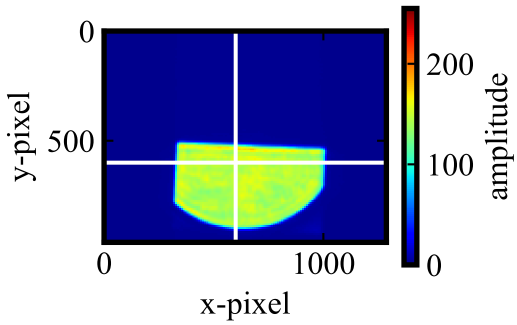

(f) Camera Image of the flat potential. The white lines show the axis for the horizontal cut in fig. 3.39

Figure 3.38 Workflow for correcting the Gaussian beamshape of the lightsource.

255 and the local pixel value is given by $\sqrt{I_{\text{loc}}}$ mod 255, resulting in dark regions in the lower corners.

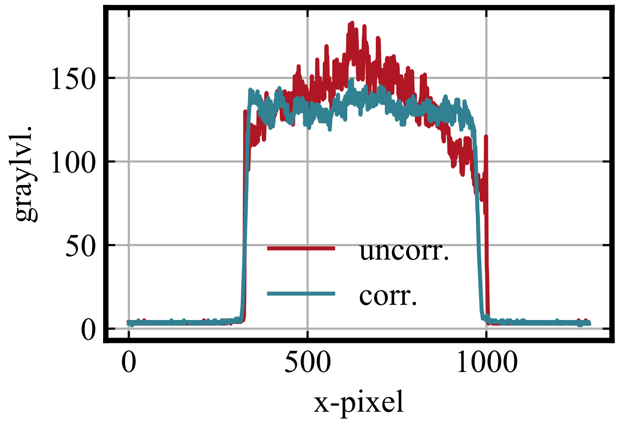

Figure 3.39 White Screen intensity and the intensity of the grayscaled potential. For grayscaling, the power of the beam was increased. The Gaussian shape of the lightsource could be corrected resulting in $\varepsilon_{\text{rms}} = 3.8\,\%$.

Flat boxes are quantified by their flatness and their root-mean-square-variation (ε_{rms}) from the target intensity. ε_{rms} for N given local values is defined as

$$\varepsilon_{\text{rms}} = \sqrt{\frac{\sum_{j=1}^{N}(\text{target}(j) - \text{data}(j))^2}{N}}. \tag{3.17}$$

In the case of a flat potential this is the standard deviation. With our setup, we achieve a root-mean-square deviation of 5.06, which corresponds to a relative flatness of 3.8 %. In fig. 3.39 the uncorrected signal (red) is curved due to the beamshape of the lightsource and by using adjusting the pattern, a flattened intensity is achieved (blue). The local corrected intensity is always bounded by the local intensity of the lightsource, but here the laserpower was increased for the second measurement.

Other cold atom experiments [47], [48] achieve flatnesses of up to 5 % and 0.3 %. Their procedure differs from the one presented here, since they used feed-back algorithms to set their binary masks. Therefore, an ε_{rms} of 3.8 % lies in the same region as other state-of-the-art experiments and the presented procedure can be used to produce grayscaled potentials.

Two relevant intensity patterns would be a Gaussian of variable width and depth as well as an harmonic pattern. Gaussian beams of blue-detuned light can be used to be superimposed with beams of red-detuned light to equalize potential curvatures. Such a beam is shown in fig. 3.41. The first row shows the mask displayed onto the DMD (left) and the corresponding intensity (right) on the camera. In the lower row, the intensities along the gray lines (a) are shown. The orange trace indicates the beam intensity on the camera with all DMD-pixels "on" and with full numerical aperture. Hence, the intensity is given by the beamprofile of the lightsource (I_l). The target beamprofile is achieved by adjusting the transmission such that

$$\sqrt{I_\text{o}(x,y)} = \sqrt{I_\text{l}(x,y)} \times \text{transmission}(x,y) \tag{3.18}$$

holds. As shown in fig. 3.41a and 3.41b, the image intensity is bounded by the local intensity of the laser. Comparing the fit with the measured intensity, one obtains a total rms deviation of four, which corresponds to a relative deviation of 4.3 %.

In addition to compensating for attractive harmonic potentials, also the repulsive beam can be used to create harmonic traps as shown in fig. 3.42. The modulated intensity was fitted to an harmonic potential leading to a root-mean-square-deviation of five (camera gray level). Since the target intensity is very low and partially close to zero, the relative deviation with respect to the target intensity is large ($\approx 25\,\%$). As mentioned above, the dynamical range of the setup is 36. By opening the iris in the beampath, which increases the NA, one increases the resolution and decreases the dynamical range. With a completly open iris, one obtains a dynamical range of three and the intensity profile can just be coarsely adjusted. Therefore small scale structure appear (c.f. fig. 3.42, full NA) on the image due to larger NA and resolution.

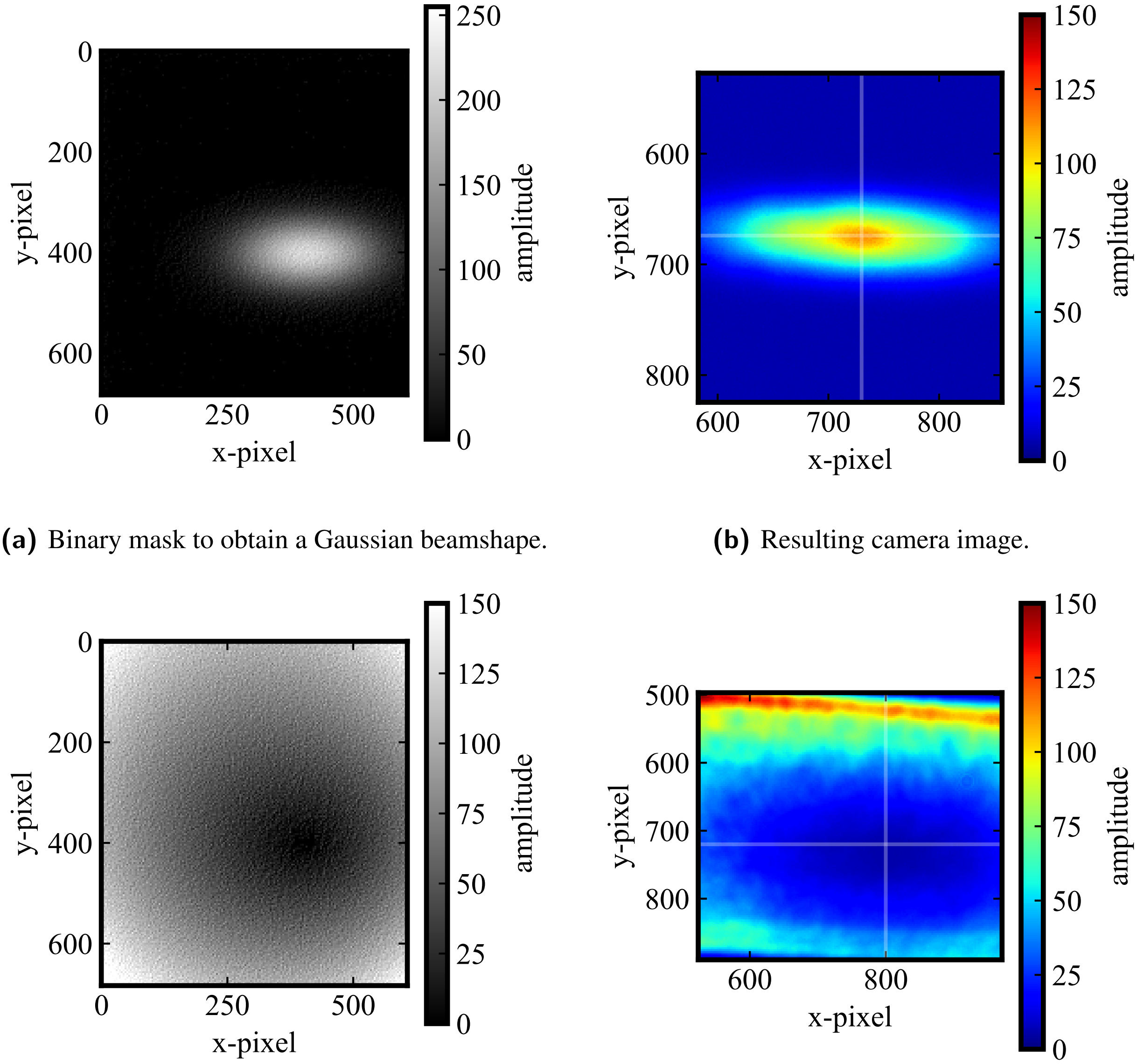

(a) Binary mask to obtain a Gaussian beamshape.

(b) Resulting camera image.

(c) Binary mask to obtain an Harmonic trap.

(d) Resulting camera image.

Figure 3.40 Binary DMD patterns and corresponding camera images. The gray lines indicate the 1D plots in fig. 3.41 and 3.42

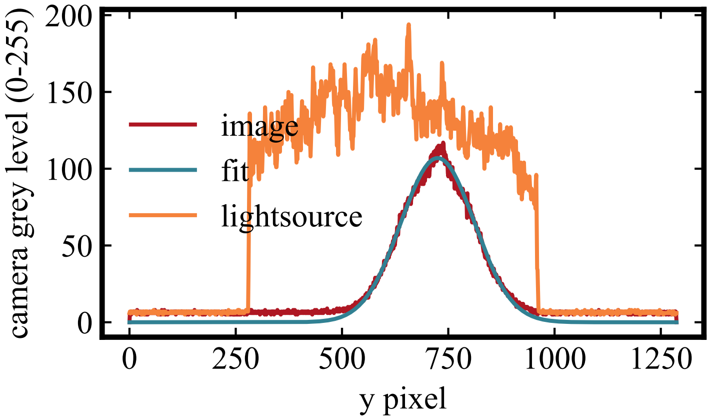

(a) 1D cut along the horizontal axis.

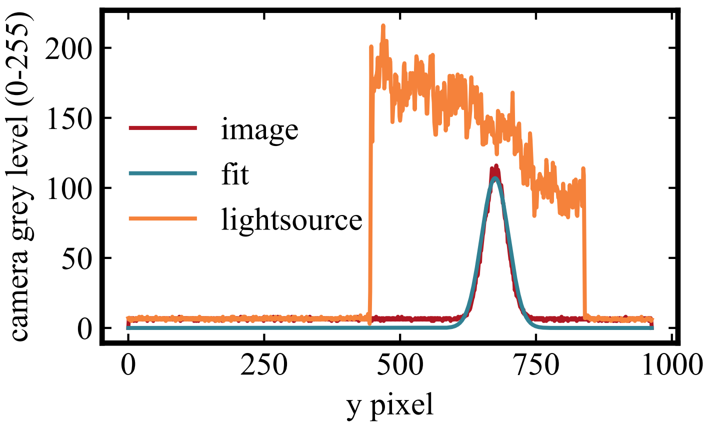

(b) 1D cut along the vertical axis.

Figure 3.41 Grayscaling to achieve a predefined Gaussian beam. The beamshape of the lightsource, the intensity of the modulated beam and the corresponding Gaussian fit at the camera plane are shown. The relative rms deviation between the fit and the measured intensity of the modulated beam is 4.3 %.

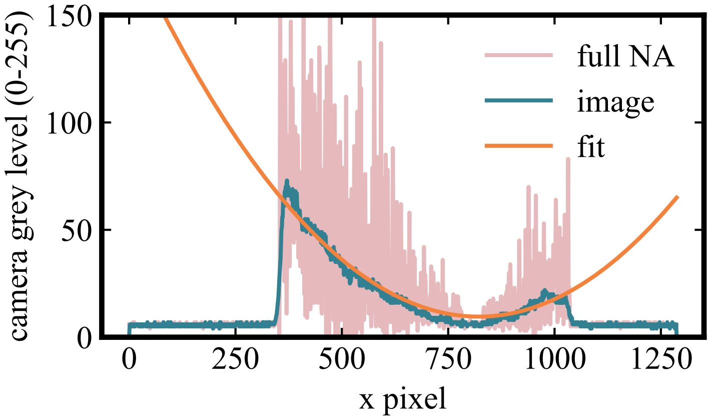

(a) 1D cut along the horizontal axis.

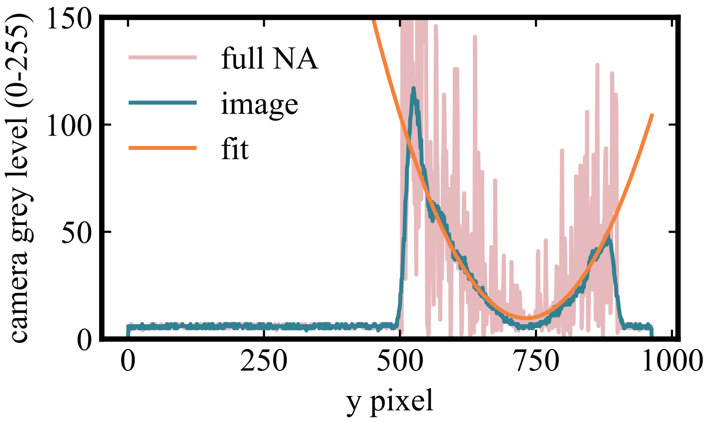

(b) 1D cut along the vertical axis.

Figure 3.42 Grayscaling to achieve an harmonic optical potential in the camera plane. The intensity of the modulated beam at a dynamical range of 36 (blue), at a dynamical range of 3 (full NA) and the corresponding harmonic fit at the camera plane are shown. The total rms deviation between the fit and the measured intensity of the modulated beam (dynamical range 36) is 5. The intensity level of the unmodulated beam is between 100 and 150.

3.4 Conclusion

The interest in universal quantities of homogeneous 2D many body systems led us to develop a setup to project arbitrary potentials in the experimental chamber. Usually, DMDs or SLMs are used for these purposes. We decided for a DMD in the image plane due to the better performance in terms of lightpower efficiency, pattern rate and simplicity (c.f. sec. 2.2). As a first target system with a sharp confinement and small variations, of the chemical potential, compared to the Fermi-energy, we planned a flat-bottom-box-shaped potential (c.f. sec. 3.2). The idea is to use the present standing-wave-trap setup (c.f. 2.1.3) and to superimpose an attractive potential created by a blue-detuned laser beam. Therefore, one can create repulsive boundaries and equalize attractive potentials (c.f. fig. 3.6).

Summarizing the scales of the target system and of the beamshaping device give the constraints for the setup. Since we aim for quantum degenerate systems with atom densities on the order $1\,\mu\mathrm{m}^{-2}$ and atom numbers on the order of 10^4 (c.f. sec. 3.2.1 and sec. 2.1.1) the system scale lies on the order of $50\,\mu\mathrm{m}$ to $100\,\mu\mathrm{m}$. The height of the potential walls should be higher than the Fermi-energy to suppress tunneling processes. We have chosen $3 \times E_\mathrm{F}$ leading to a loss rate of $0.003\,\mathrm{atoms/s}$.

The desired system size, the size of the DMD chip area ($\sim 2\,\mathrm{cm}$) and its micromirrors ($7.56\,\mu\mathrm{m}$) set the needed scale of the magnification, since one wants to use as much mirrors as possible for finer control of the potential. On the other hand, by increasing the magnification and reducing the used chip-area, one achieves a higher dynamical range in the atom plane (c.f. 3.2.1 and fig. 3.7). Finding a compromise between large dynamical range and effective use of the chip, led to a demagnification on the order of 85. Since, an iris in the Fourier plane offers Fourier filtering, adjustments of the dynamical range and the resolution, a beam path with well defined Fourier planes is advantageous. Accordingly, two 4-f setups consisting of a 500 mm, 300 mm, 1000 mm and the objective as last lens (focal length 20.3 mm) is used.

The lightsource for the blue beam is the iBeam-SMART-660-S with a center wavelength of 660 nm and maximal power output of 130 mW. Being relatively close to the atomic resonance at 671 nm enables us to work with laser powers at the mW scale. As emphasized by fig. 3.8, scaling the detuning is always a trade-off between the needed power decreasing for smaller detuning and the scattering rate, increasing for smaller detuning. By calculating the corresponding lossrate above, we made sure to work in a reasonable regime.

The laser is a free running diode laser with the capability of driving several laser modes by voltage amplitude modulation and therefore reducing the coherence length (c.f. sec. 3.2.2). For the best performance in terms of relative intensity noise and coherence length it turned out, that the laser should be operated in SKILL mode (reduced coherence length) and at medium to high output powers.

Having decided about the design, it is planned to integrate the DMD setup in the experiment as shown in fig. 3.21.

Having the DMD operating, it is important, which imaging imperfections occur and how one can account for them. On the one hand there are ringing effects due to the coherence properties of the light (c.f. in sec. 3.3.1). These effects are present at sharp features but they get suppressed within $1\,\mu$m. On the other hand there are geometrical distortions of the image due to imperfect imaging. We have shown by using affine transformations between the DMD and imaging plane, that we can compensate for distortions (c.f. fig. 3.25 and fig. 3.26).

In principle there are two different types of potentials to consider: binary- and grayscaled potentials. For adequate grayscaling it is crucial to have precise and reversible mapping between DMD plane and camera plane, since one has to account for the initial beamshape of the lightsource (c.f. sec. 3.3.2, fig. 3.38 and fig. 3.28). Our ability of grayscaling is quantified by the achieved root-mean-square deviation from the target intensity level of $3.8\,\%$. That is illustrated in fig. 3.39.

In the future, displaying a grayscaled repulsive pattern could be used to compensate the attractive first order harmonic potential created by the 2D standing-wave-trap.

All in all a procedure to display binary potentials and to account for image imperfections was presented. Additionally the setup enables us to do grayscaling which is quantified by a root-mean-square variation of $3.8\,\%$ from a constant target potential (c.f. fig. 3.39 compare with e.g. [48] or [47]), which is a good starting point to build arbitrary potentials (c.f. fig. 3.41 and fig. 3.42) and face the measurement of bulk properties of quantum gases.

4

Further perspectives

As already discussed above, our motivation for the DMD setup is to study bulk properties of 2D Fermi gases as proposed in [10] and [1]. Another approach is the creation of two connected boxes. By changing their size and measuring transport quantities, we want to study the transition from few-body coherently described systems to large quantum statistical ensembles as motivated in [49] and [2]. Hence, we need tools to create repulsive potentials, confining the atoms in arbitrary geometries. We decided for a DMD setup, which, once it is included in the experiment, will give us the flexibility to project arbitrary potentials on the atoms.

In this thesis such a setup was planned and evaluated using a test-setup. The performance of the used laser, the imaging system and the software control of the DMD was quantified. Currently there remain two minor issues. Firstly, the current DMD evaluation module has a very limited upload speed (c.f. sec. 3.1.7) and secondly, mirror flickering creates intensity noise on the potential (c.f. sec. 3.1.6).

To solve these issues we ordered another DMD (Vialux V-9501). This model is a modified version of the Texas Instrument device. The flickering on the current DMD is caused by a global mirror release each $105\,\mu$s, which also limits the maximal pattern rate to $1/105\,\mu\text{s} = 9.5\,\text{kHz}$. The Vialux model offers to set the global release manually. One can freeze the mirror position for a time between $77\,\mu$s and several seconds. Hence, intensity noise of static potentials due to flickering is not an issue anymore. Furthermore, the maximal pattern rate is slightly increased to $1/77\,\mu\text{s} = 13\,\text{kHz}$.

Additionally, transfer of image data on the Vialux board is handled with a USB3.0 interface providing transfer rates above 1600 fps, while the current DMD data transfer rate is limited by $64\,\text{kB/s}$[1] and therefore the upload speed issue is also solved. Nevertheless, the new board still requires pre-defined patterns, such that no streaming during the experimental sequence is possible and any dynamical adjustment has to be done manually.

With the current setup at hand, binary potentials can be created. Currently we plan to first use our setup to create a flat box potential. However, initially there will be no compensation for the curvature of the underlying 2D trap. As the residual

[1] Transfer rates of approximately $30\,\text{kB/s}$ were measured.

curvature (on the order of 100 Hz) will be much smaller than the chemical potential of our strongly interacting Fermi gas (on the order of 5 kHz), this should however not be a problem. Therefore, we can study bulk properties, e.g. transport parameters, of ultracold Fermi gases as proposed in [1]. Additionally, we might also make use of our capability to create small samples [17] in order to investigate phenomena related to superfluidity in the few-particle limit. One example are AC Josephson oscillations, which have already been observed in many-body cold-atom systems [20], but not in the few-particle context.

Another perspective is the already mentioned transition from coherent few-body samples to quantum statistical ensembles in setups related to [49]. How will well-known effects as e.g. the quantized conductance be affected by the size of the system? Is the transport dominated by single particles or by correlated pairs?

These questions can be tackled with our setup. With the DMD two connected boxes can be projected into the experimental chamber, setting the potential landscape. The imaging setup offers single atom resolution [50]. Therefore, correlation measurements [19] are feasible and we have access to the counting statistics.

Furthermore, the DMD setup allows us to go beyond binary potentials. The creation of arbitrary potentials by doing grayscaling is a promising perspective, since it provides to scale the local trapdepth. Accordingly, one can project arbitrarily shaped traps in the atom plane and imprint phase patterns on the wavefunction. Nevertheless, sine DMDs provide a binary mask, intensity cannot be redistributed over the image. Patterns are created by discarding intensity of the initial beam and therefore one has to account for the beamshape of the lightsource. Hence, all potentials which do not have a similar shape as the incoming intensity distribution are highly ineffective and therefore a lot of power is needed. This can be solved by either adding an additional lightsource or the inclusion of phaseplates to shape the beam impining on the DMD, which could be options for the future.

All in all, the inclusion of a DMD in our setup adds the possibility of beamshaping and grayscaling, enabling us to create homogeneous atomic systems and even (nearly) arbitrary trapping geometries. Therefore, the DMD adds flexibility to the setup and gives us access to new interesting physics.

5 Appendix

5.1 USB protocol

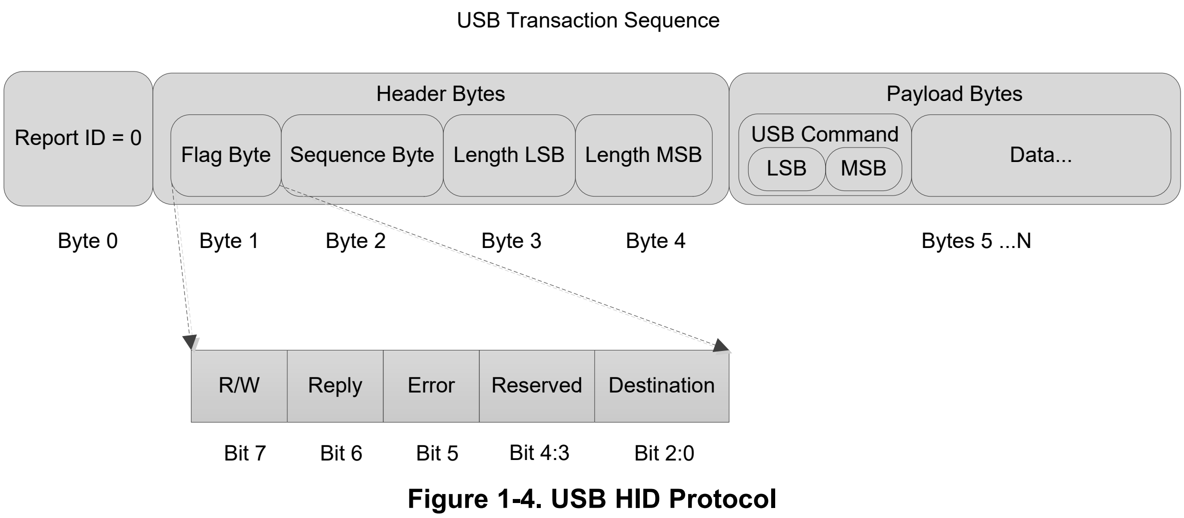

Figure 5.1 USB-protocol. The structure of the sent messages is shown. Image taken from the Programmers Guide of TI [29]

USB HID protocols are structured as shown in fig. 5.1. The users sends a Report ID, which set to zero by default in all cases, four header bytes, which describe the message that will be transmitted and the payload bytes which contain the data that the user wants to send. The header consists of a header byte which defines if the operation will be a read or write operation and if the user expects a response. The header byte is followed by the sequence byte which acts like a reference. If the user expects a response to a write command, the sequence sent by the device will have the same sequence byte as the write command. The last two header bytes mark the total length of the data to transmit in this transfer as least significant byte followed by most significant byte. For all DMD operations exists a USB command which is a number of four hexadecimal digits. In some cases the DMD operation is not fully defined by the USB command but needs to be clarified by some data. For example “0x1A1B” signifies the “Display Mode Selection Command” which has to be followed up by a digit which defines the display mode. One transaction consists of maximally 65 bytes (including the Report ID) whereas the internal command buffer of the DMD consists of 512 bytes. These are used for multiple transfer commands with large payloads, e.g. sequences defining certain patterns. In multiple transfer sequences, the descriptive bytes are just given in the first message. This way, filling the internal buffer of the DMD corresponds to a maximal amount of transmitted data of 504 bytes[1].

5.2 Flickering

The DMDLC9000 as well as the DMDLC6500 from Texas Instruments “flicker” as mentioned in sec 3.1.6. The controllers send a release pulse to the DMD chip every 105 μs, such that a global release is executed. Therefore, the electrodes holding the micromirrors in position are grounded (c.f. 3.4) and the micromirrors oscillate freely, until the electrodes are active again.

We measured the total reflected intensity of the laser beam over time and saw, that it varies every 105 μs for approximately 5 μs. The corresponding relative intensity noise makes it impossible to display static patterns without parametric heating in the trap. In [32], a hardware workaround is presented. They interrupt the signal line, that triggers the flickering with a switch.

Alternatively, there is a software workaround that avoids flickering proposed by an applications engineer of DigitalLight Innovations. As reported in sec. 3.1.4, we use the “Pattern-On-The-Fly mode”. The user can set the pattern switch, the dark time t_{dark} and the illumination time $t_{\text{illumination}}$. The pattern switch can be triggered either by an internal timer or by an external trigger. After the pattern has switched it is displayed for $t_{\text{illumination}}$, as soon as the illumination time is over, all mirrors are switched in the “off” position for t_{dark}.

If the pattern switch is set to external trigger mode, the dark time to zero and the illumination time to its minimal value of 105 μs, the DMD displays the pattern for 105 μs and switches to the next pattern as soon as a trigger signal is received. In the time after the illumination and before receiving the trigger, the DMD switches all mirrors in their “off” position, but does not flicker. The idea is to let the DMD hold the pattern, instead of switching all micromirrors in the “off” position during this

[1] first message: 1 (report ID) + 4 (header) + 2 (USB comm) + 2 (length of the datastream) + 56 (data). Seven additional messages contain 1 (report ID) + 64 (data). That gives in total $56 + 7 \times 64 = 504$ transferred data bytes

time. The “pattern clear” after $t_{\text{illumination}}$ is not handled automatically but caused by a command, sent by the user.

We used the USB-protocol and the procedure introduced in [29] to initialize the “Pattern-On-The-Fly” mode. The “LUT Definition Command” (0x0134), consisting of 11 bytes, sets the timings and trigger settings for each pattern, as well as the “pattern clear”. By modifying the zeroth bit of the fifth byte of the command, one deactivates the “pattern clear” manually. A fifth byte, which is generated by the TI GUI, setting the bit depth to zero (bit $1:3 = 000$), disabling all LEDs (bit $4:6 = 000$) and setting the pattern switch to external trigger mode (bit $7 = 1$) is given as 0b10000001 (zeroth bit is on the right). The zeroth bit enables the pattern clearing after the exposure time and that can be switched of manually by setting the zeroth bit to 0, such that the corresponding fifth byte would look like 0b10000000.

5.3 Floyd Steinberg

For the image dithering process the Floyd Steinberg algorithm, as presented in [43] was used. As motivated in [45], the algorithm was adjusted to suppress the emergence of periodic patterns. The algorithms goes through the image from top to bottom and from left to right. Each pixel is binarized by using `get_closest_color`. After binarization the quantization error is added to neighboring unbinarized pixels before the algorithm proceeds. Therefore, the quantization errors get diffused over the whole image. By adding the randomly distributed value delta in each binarization process, the pattern gets slightly disturbed and periodic structures emerging get suppressed (c.f. 3.33).

```
for yy in range(0,im_matrix.shape[1]-1):
    for xx in range(0,im_matrix.shape[0]-1):
            oldpix = im_matrix[xx][yy]
            newpix = get_closest_color(oldpix, sigma)
            im_matrix[xx][yy] = newpix
        quant_error = oldpix - newpix
        im_matrix[xx+1][yy] =
            im_matrix[xx+1][yy] + quant_error*7/16
        im_matrix[xx-1][yy+1] =
            im_matrix[xx-1][yy+1]+quant_error*3/16
        im_matrix[xx][yy+1] =
            im_matrix[xx][yy+1] + quant_error*5/16
        im_matrix[xx+1][yy+1] =
            im_matrix[xx+1][yy+1] + quant_error*1/16
```

```python
def get_closest_color(uu, sigma):
    delta = np.random.normal(128, sigma*255)
    if uu + delta > 128:
        return 255
    else:
        return 0
```

Bibliography

[1] Tilman Enss. “Bulk Viscosity and Contact Correlations in Attractive Fermi Gases.” In: *Phys. Rev. Lett.* **123** (20 Nov. 2019), p. 205301.

[2] Giulio Amato *et al.* “Noninteracting many-particle quantum transport between finite reservoirs.” In: *Phys. Rev. A* **102** (2 Aug. 2020), p. 022207.

[3] J. Bardeen *et al.* “Theory of Superconductivity.” In: *Phys. Rev.* **108** (5 Dec. 1957), pp. 1175–1204.

[4] Wolfgang Ketterle and Martin Zwierlein. *Making, probing and understanding ultracold Fermi gases*. 2008. arXiv: `0801.2500 [cond-mat.quant-gas]`.

[5] I. Boettcher *et al.* “Equation of State of Ultracold Fermions in the 2D BEC-BCS Crossover Region.” In: *Phys. Rev. Lett.* **116** (4 Jan. 2016), p. 045303.

[6] P. A. Murthy *et al.* “Observation of the Berezinskii-Kosterlitz-Thouless Phase Transition in an Ultracold Fermi Gas.” In: *Phys. Rev. Lett.* **115** (1 June 2015), p. 010401.

[7] Markus Bohlen *et al.* “Sound Propagation and Quantum-Limited Damping in a Two-Dimensional Fermi Gas.” In: *Phys. Rev. Lett.* **124** (24 June 2020), p. 240403.

[8] Mark J. H. Ku *et al.* “Revealing the Superfluid Lambda Transition in the Universal Thermodynamics of a Unitary Fermi Gas.” In: *Science* **335**.6068 (2012), pp. 563–567. eprint: `https://science.sciencemag.org/content/335/6068/563.full.pdf`.

[9] Puneet A. Murthy *et al.* “Quantum scale anomaly and spatial coherence in a 2D Fermi superfluid.” In: *Science* **365**.6450 (2019), pp. 268–272. eprint: `https://science.sciencemag.org/content/365/6450/268.full.pdf`.

[10] Bernhard Frank *et al.* “Quantum critical thermal transport in the unitary Fermi gas.” In: *Phys. Rev. Research* **2** (2 June 2020), p. 023301.

[11] Puneet Anantha Murthy. "Emergent phenomena in two-dimensional Fermi systems." PhD thesis. Universität Heidelberg, 2018.

[12] Wilhelm Zwerger. *The BCS-BEC Crossover and the Unitary Fermi Gas*. first edition. Springer-Verlag Berlin Heidelberg, 2012.

[13] Luca Bayha. "Emergence of Many-Body Physics in Two-Dimensional Few-Fermion Systems." PhD thesis. Universität Heidelberg, 2020.

[14] Rudolf Grimm *et al.* "Optical Dipole Traps for Neutral Atoms." In: vol. 42. Advances In Atomic, Molecular, and Optical Physics. Academic Press, 2000, pp. 95–170.

[15] M. E. Gehm. "Preparation of an Optically-Trapped Degenerate Fermi Gas of6Li: Finding the Route to Degeneracy." PhD thesis. Duke University, 2003.

[16] Andre Wenz. "From Few to Many:Ultracold Atoms in Reduced Dimensions." PhD thesis. Universität Heidelberg, 2013.

[17] Luca Bayha *et al.* "Observing the emergence of a quantum phase transition shell by shell." In: *Nature* **587** (Nov. 2020), pp. 583–587.

[18] T. A. Savard *et al.* "Laser-noise-induced heating in far-off resonance optical traps." In: *Phys. Rev. A* **56** (2 Aug. 1997), R1095–R1098.

[19] Marvin Holten *et al.* *Observation of Pauli Crystals*. 2020. arXiv: `2005.03929 [cond-mat.quant-gas]`.

[20] Niclas Luick *et al.* "An ideal Josephson junction in an ultracold two-dimensional Fermi gas." In: *Science* **369**.6499 (July 2020), pp. 89–91.

[21] Rick van Bijnen. "Quantum Engineering with Ultracold Atoms." PhD thesis. Eindhoven University of Technology, 2013.

[22] Joseph W. Goodman. *Introduction to Fourier Optics*. first edition. McGraw-Hill, 1968.

[23] Bahaa Saleh and Malvin Teich. *Fundamentals of photonics*. first edition. John Wiley and Sons, Inc., 1991.

[24] Ruichao Ma. "Engineered potentials and dynamics of ultracold quantum gases under the microscope." PhD thesis. Harvard University, 2014.

[25] Yunxin Wang *et al.* "Speckle noise suppression in digital holography by angular diversity with phase-only spatial light modulator." In: *Opt. Express* **21**.17 (Aug. 2013), pp. 19568–19578.

[26] Shigeo Kubota and Joseph Goodman. "Very efficient speckle contrast reduction realized by moving diffuser device." In: *Applied optics* **49** (Aug. 2010), pp. 4385–91.

[27] Muhammad Akram *et al.* "Laser speckle reduction due to spatial and angular diversity introduced by fast scanning micromirror." In: *Applied optics* **49** (June 2010), pp. 3297–304.

[28] Texas Instruments, ed. *DLP® LightCrafter™ 6500 and 9000 Evaluation Module (EVM) User's Guide*. 2014.

[29] Texas Instruments, ed. *DLPC900 Programmer's Guide*. 2014.

[30] Anton Mazurenko. *Lightcrafter6500DMDControl*. Oct. 2020. URL: `https://github.com/mazurenko/Lightcrafter6500DMDControl`.

[31] Rene F. Aguirre. *pywinusb 0.4.2*. Oct. 2020. URL: `https://pypi.org/project/pywinusb/`.

[32] Klaus Hueck *et al.* "Note: Suppression of kHz-frequency switching noise in digital micro-mirror devices." In: *Review of Scientific Instruments* **88**.1 (2017), p. 016103. eprint: `https://doi.org/10.1063/1.4973969`.

[33] Klaus M. Hueck. "A homogenous, two-dimensional Fermi gas." PhD thesis. Universität Hamburg, 2017.

[34] Dr. Thomas Renner. *iBeam smart*. Dec. 2020. URL: `https://www.toptica.com/products/single-mode-diode-lasers/ibeam-smart/`.

[35] Martin Ries. "A Two-Dimensional Fermi Gas in the BEC-BCS Crossover." PhD thesis. Universität Heidelberg, 2015.

[36] Franz Schwabl. *Quantenmechanik*. seventh edition. Springer-Verlag Berlin Heidelberg, 2007.

[37] Newport, ed. *An Overview of Laser Diode Characteristics*. 2005.

[38] Meiqi Li *et al.* "Structured illumination microscopy using digital micromirror device and coherent light source." In: *Applied Physics Letters* **116**.23 (2020), p. 233702. eprint: `https://doi.org/10.1063/5.0008264`.

[39] Alice Sandmeyer *et al.* "DMD-based super-resolution structured illumination microscopy visualizes live cell dynamics at high speed and low cost." In: *bioRxiv* (2019). eprint: `https://www.biorxiv.org/content/early/2019/10/08/797670.full.pdf`.

[40] Guillaume Gauthier *et al.* "Quantitative Acoustic Models for Superfluid Circuits." In: *Phys. Rev. Lett.* **123** (26 Dec. 2019), p. 260402.

[41] L. Amico *et al.* *Roadmap on Atomtronics*. 2020. arXiv: `2008.04439 [cond-mat.quant-gas]`.

[42] Guillaume Gauthier *et al.* "Giant vortex clusters in a two-dimensional quantum fluid." In: *Science* **364**.6447 (2019), pp. 1264–1267. eprint: `https://science.sciencemag.org/content/364/6447/1264.full.pdf`.

[43] Robert W. Floyd and Louis Steinberg. "An Adaptive Algorithm for Spatial Greyscale." In: *Proceedings of the Society for Information Display* **17**.2 (1976), pp. 75–77.

[44] Mohamed Attia *et al.* "A General scheme for dithering multidimensional signals, and a visual instance of encoding images with limited palettes." In: *Journal of King Saud University - Computer and Information Sciences* **26**.2 (2014), pp. 202–217.

[45] Anton Mazurenko. "Probing Long Range Antiferromagnetism and Dynamics in the Fermi-Hubbard Model." PhD thesis. Harvard University, 2017.

[46] Christophe Dorrer and Jonathan D. Zuegel. "Design and analysis of binary beam shapers using error diffusion." In: *J. Opt. Soc. Am. B* **24**.6 (June 2007), pp. 1268–1275.

[47] Mohammadamin Tajik *et al.* "Designing arbitrary one-dimensional potentials on an atom chip." In: *Optics express* **27**.23 (Nov. 2019), pp. 33474–33487.

[48] Jinyang Liang *et al.* “High-precision laser beam shaping using a binary-amplitude spatial light modulator.” In: *Appl. Opt.* **49**.8 (Mar. 2010), pp. 1323–1330.

[49] Samuel Häusler *et al.* *Interaction-assisted reversal of thermopower with ultracold atoms*. 2020. arXiv: `2010.00011 [cond-mat.quant-gas]`.

[50] Andrea Bergschneider *et al.* “Spin-resolved single-atom imaging of ^{6}Li in free space.” In: *Phys. Rev. A* **97** (6 June 2018), p. 063613.

Erklärung:

Ich versichere, dass ich diese Arbeit selbstständig verfasst habe und keine anderen als die angegebenen Quellen und Hilfsmittel benutzt habe.

Heidelberg, den (Datum) 14.12.2020 C. Hintze ....

Last but not least, I want to thank all the people from the ultracold group who supported me, writing this thesis.

- the team of the new experiment: Luca Bayha, Marvin Holten, Keerthan Subramanian and Sandra Brandstetter for answering my questions, explaining the experiment, giving me introductions to electronics and optics and also giving me a lot of feedback on my thesis
- Philipp Preiß for detailed discussions about beamshaping, coherence and Fourier optics
- Selim Jochim for letting me joining the group and providing a productive scientific environment
- and Fred Jendrzejewski for offering to co-supervise this Master thesis.